USGS
science for a changing world

Prepared in cooperation with the California State Water Resources Control Board

Airborne Electromagnetic Survey Results near the Poso Creek Oil Field, San Joaquin Valley, California, Fall 2016

Data Report 1155

U.S. Department of the Interior
U.S. Geological Survey

Cover. Airborne electromagnetic system operated by SkyTEM ApS in the southern San Joaquin Valley of California, October 2016 (Photograph by Lyndsay Ball).

Airborne Electromagnetic Survey Results near the Poso Creek Oil Field, San Joaquin Valley, California, Fall 2016

By Katrina D. Zamudio, Lyndsay B. Ball, and Michael J. Stephens

Prepared in cooperation with the California State Water Resources Control Board

Data Report 1155

U.S. Department of the Interior
U.S. Geological Survey

U.S. Geological Survey, Reston, Virginia: 2022

Suggested citation:
Zamudio, K.D., Ball, L.B., and Stephens, M.J., 2022, Airborne electromagnetic survey results near the Poso Creek oil field, San Joaquin Valley, California, fall 2016: U.S. Geological Survey Data Report 1155, 55 p., https://doi.org/10.3133/dr1155.

Associated data for this publication:
Zamudio, K.D., and Ball, L.B., 2022, Aireborne electromagnetic and magnetic survey data, southeastern San Joaquin Valley near Cawelo, California, 2016: U.S. Geological Survey data release https://www.sciencebase.gov/catalog/item/5d642e32e4b01d82ce987143.

ISSN 2771-9448 (online)

Acknowledgments

Appreciation is extended to our cooperators and collaborators. This work was funded by the California State Water Resources Control Board's Oil and Gas Regional Monitoring Program. Airborne geophysical data were acquired by SkyTEM ApS under contract with the U.S. Geological Survey. Borehole geophysical logs were digitized by the California State University, Sacramento Water Resources Group through a cooperative agreement with the U.S. Geological Survey.

Contents

Figures

Table

Conversion Factors

International System of Units to U.S. customary units

Multiply	By	To obtain
	Length	
meter (m)	3.281	foot (ft)
kilometer (km)	0.6214	mile (mi)
	Area	
square meter (m^2)	10.76	square foot (ft^2)
square kilometer (km^2)	0.3861	square mile (mi^2)
	Volume	
liter (L)	1.057	quart (qt)
Mass		
gram (g)	0.03527	ounce, avoirdupois (oz)
	Frequency	
hertz (Hz)	1	cycle per second

Datum

Vertical coordinate information is referenced to the North American Vertical Datum of 1988 (NAVD 88).

Horizontal coordinate information is referenced to the North American Datum of 1983 (NAD 83).

Altitude, as used in this report, refers to distance above the ground surface.

Elevation, as used in this report, refers to the distance above the vertical datum.

Supplemental Information

Concentrations of chemical constituents in water are given in milligrams per liter (mg/L).

Electrical resistivity is given in ohm meters (Ω•m) unless otherwise specified.

Magnetic moment is given in ampere square meter ($A•m^2$).

Abbreviations

A	ampere
Ω	ohm
AEM	airborne electromagnetic
COGG	California Oil Gas and Groundwater
DOI	depth of investigation
SCI	spatially constrained inversion
3D	three dimensional
TDS	total dissolved solids
USGS	U.S. Geological Survey

Airborne Electromagnetic Survey Results near the Poso Creek Oil Field, San Joaquin Valley, California, Fall 2016

By Katrina D. Zamudio, Lyndsay B. Ball, and Michael J. Stephens

Abstract

An airborne electromagnetic survey west of the Poso Creek oil field, located in the southeastern San Joaquin Valley, California, was flown in October 2016 to improve understanding of the hydrogeologic setting and the distribution of groundwater salinity in the area. The airborne electromagnetic data were used to develop resistivity models of the subsurface, where the mean depth of investigation is about 300 meters below the land surface and thus characterizes parts of the Kern River Formation and overlying sediments. Resistivity models along with water table elevation, historical total dissolved solids measurements of water samples from wells, well lithologic records, borehole geophysical logs, and mapped surface geology were used to develop an understanding of local hydrogeologic controls on resistivity. Interpretation of these data indicate the resistivity structure primarily reflects the general lithologic character and geologic structure of the study area, with more subtle influences from variations in saturation and salinity.

Introduction

The U.S. Geological Survey (USGS), in cooperation with the California State Water Resources Control Board (State Water Board), is conducting regional studies of groundwater quality in California near areas of oil and gas production. California is the largest agricultural producer in the United States (U.S. Department of Agriculture Economic Research Service, 2010) has the largest population (U.S. Census Bureau, 2018), and leads the country in total water use and annual groundwater withdrawal volumes (Dieter and others, 2018). California is also one of the largest on-shore oil and gas producing States (U.S. Energy Information Administration, 2017) with nearly 500 oil and gas fields. The Oil and Gas Regional Monitoring Program, authorized by California Senate Bill 4 (California Senate, 2013) and initiated by the State Water Board in 2015, was developed in response to concerns about the potential risks and impacts of oil and gas development on groundwater resources that may have current or future beneficial use (California State Water Resources Control Board, 2015). As part of the Regional Monitoring Program, the USGS is conducting interdisciplinary studies of groundwater quality near oil and gas fields under the California Oil Gas and Groundwater (COGG) program. The COGG program has several broad objectives: (1) locate aquifers containing fresh and brackish groundwater (defined as total dissolved solids [TDS] concentration <10,000 milligrams per liter [mg/L]) near oil and gas fields that could potentially have beneficial use for drinking water, irrigation, or industrial purposes, (2) assess the vulnerability of fresh and brackish aquifers to mixing with oil field fluids by understanding the relative locations of oil and gas operations and groundwater resources, (3) determine if there is evidence of oil and gas constituents in aquifers, (4) identify potential hydrogeologic pathways or processes connecting oil and gas operations and sources with aquifers, and (5) assess the regional-scale effects of oil and gas operations on groundwater quality (California Oil, Gas, and Groundwater Program, 2020). The COGG program takes a diverse approach to address these objectives, including historical compilations of water quality data, geochemical analyses of groundwater and oil field water and gas, analyses of borehole geophysical logs, development of geologic frameworks, and collection of new geophysical data.

Geophysical data, including those derived from airborne electromagnetic (AEM) surveys, provide insights into subsurface geology and groundwater salinity conditions that can be used to address some of the objectives of the COGG program (California Oil, Gas, and Groundwater Program, 2020). AEM data are used to derive three dimensional (3D) resistivity models of the subsurface. These resistivity models are similar in concept to low vertical-resolution borehole electrical or induction logs. However, borehole geophysical logs typically occur at irregularly dispersed well locations with data collected at various times, often spanning decades, whereas AEM surveys can acquire resistivity information across the landscape at a uniform spacing of roughly 30–40 meters (m) along the flight path of the aircraft, with data collection typically spanning a relatively narrow time window of days to weeks. AEM-derived bulk resistivity is influenced by a combination of the electrical properties of the pore fluids and the rocks and sediments. The resistivity results derived from AEM surveys can serve as a foundation for understanding spatial variations in groundwater salinity and to better understand the hydrogeologic setting, including changes in saturation, clay content, lithologic texture, and the geologic structure and location of faults that may influence hydraulic conductivity and define preferential groundwater flow paths.

The southern San Joaquin Valley (fig. 1) has been the initial focus of the AEM effort under the COGG program. This area serves as one of the most heavily developed oil-producing regions in California, putting energy development in close proximity to groundwater resources in many places (Davis and others, 2018b). AEM surveys were conducted in the fall 2016 adjacent to the Lost Hills and Belridge oil fields on the western margin of the valley and the Poso Creek oil field on the eastern margin. These fields were designated as high priority for detailed study based on the relatively high density of groundwater and petroleum wells; the vertical proximity of oil and gas development and groundwater resources; and the volume of injected fluids associated with the disposal of water produced during oil and gas production, commonly referred to as produced water, as well as enhanced oil recovery and subsidence control (Davis and others, 2018b). There are several hydrogeologic characteristics that differ between the western and eastern margins of the San Joaquin Valley that influenced the selection of both western and eastern study areas for the 2016 survey effort. The geologic materials that make up the shallow aquifers have different geologic sources. The western-margin sediments source from the marine sedimentary and metasedimentary formations of the Coast Ranges, whereas the eastern-margin sediments derive primarily from the crystalline rocks of the southern Sierra Nevada Mountains (fig. 1). Salinity in both groundwater and produced water is notably higher near the western valley margin in comparison to the eastern valley margin (Gillespie and others, 2017; Metzger and Landon, 2018). In the western valley near the Lost Hills and Belridge oil fields, TDS concentrations in shallow groundwater (upper 300 m) commonly exceed 3,000 mg/L and in some areas exceed 10,000 mg/L in complex patterns (Gillespie and others, 2019; Ball and others, 2020), and produced water is typically around 30,000 mg/L (McMahon and others, 2018; Metzger and Landon, 2018). In contrast, in the eastern valley near the Poso Creek oil field, groundwater TDS concentrations are typically below 1,000 mg/L, and the median produced water TDS concentration is about 1,300 mg/L (Metzger and Landon, 2018; Stephens and others, 2021). The major hydrogeologic differences of the eastern and western valley margins are expected to result in differences in the character of the subsurface resistivity structure and differences in interpretational sensitivity. The Poso Creek survey provides as an opportunity to explore the major hydrogeologic controls on resistivity and to define the potential role for AEM in areas of relatively fresh groundwater along the eastern margin of the San Joaquin Valley and other similar hydrogeologic settings.

This report presents results of the 2016 AEM survey conducted adjacent to the Poso Creek oil field. Results from the Lost Hills and Belridge AEM survey area, including 3D categorical salinity mapping interpretations, have been previously published by Ball and others (2020) and Ball (2020). This report presents the general resistivity structure of the Poso Creek area and discusses the correlations between AEM-derived resistivity and historical groundwater salinity, water table elevation, aquifer lithologic texture, and geologic formations and structures defined by available well records and geologic mapping. This report also explores the potential for groundwater to exceed TDS concentration thresholds commonly used by resource managers to establish the groundwater resource potential of aquifers, specifically 3,000 mg/L (fresh to brackish) and 10,000 mg/L (brackish to saline) thresholds (California State Water Resources Control Board, 1988; 40 CFR part 144). The AEM data also serve as a potential baseline of aquifer conditions for interpreting future changes in groundwater salinity relative to the fall 2016.

Hydrogeologic Setting

The Poso Creek AEM survey area is near the southeastern margin of the San Joaquin Valley, the southern-most extension of California's Central Valley (fig. 1). The survey area is located north of the city of Bakersfield along the relatively flat-lying valley floor adjacent to the western-most rise of the Sierra Nevada foothills. Land use in the Poso Creek survey area is dominated by irrigated agriculture, with most of the area used as orchards, in addition to vineyards, fallow land/open space, and other crops (Kern County Department of Agriculture, 2016).

The San Joaquin Valley, flanked on the east by the Sierra Nevada Mountains and on the west by the highly deformed Coast Ranges, is filled with Mesozoic Era and Cenozoic Era sediments up to 9 kilometers (km) thick on top of west-tilted crystalline Sierra Nevada basement rocks (Croft 1972, Bartow 1991). The Poso Creek survey area lies immediately west of the developed portion of the Poso Creek oil field. Production in the field comes from the late Miocene Chanac Formation and the basal sands of the Pliocene Etchegoin Formation (Weddle, 1959; Welge, 1973). The basal sands of the Etchegoin Formation are capped by the Macoma claystone, which underlies the upper Etchegoin sands and shales. The late Pliocene–Pleistocene Kern River Formation and undifferentiated Tertiary and Quaternary deposits overlie these units (Weddle, 1959; Welge, 1973; Bartow, 1991), and together they comprise the approximately 300-m depth of investigation (DOI) of the AEM survey. The Kern River Formation consists of continental alluvial deposits of poorly sorted clay, silt, sand, and gravel derived from the mountains east and south of the valley (Croft 1972; Faunt, 2009). Interbedded lacustrine siltstone, mudstone, and clay units may be present in places (Bartow and Pittman, 1983). The Tertiary and Quaternary deposits are compositionally similar to the Kern River Formation and generally cannot be easily differentiated (Cawelo Groundwater Sustainability Agency, 2020). In the survey area, these west-dipping sediments are cut by north-northwest trending normal faults (Bartow, 1991). The 125-km long northwest trending Poso Creek normal fault cuts the Kern River Formation (fig. 1) and is downthrown to the southwest with documented offsets ranging from 500 m to less than 1 m (Bartow, 1991; Beahm, 2015).

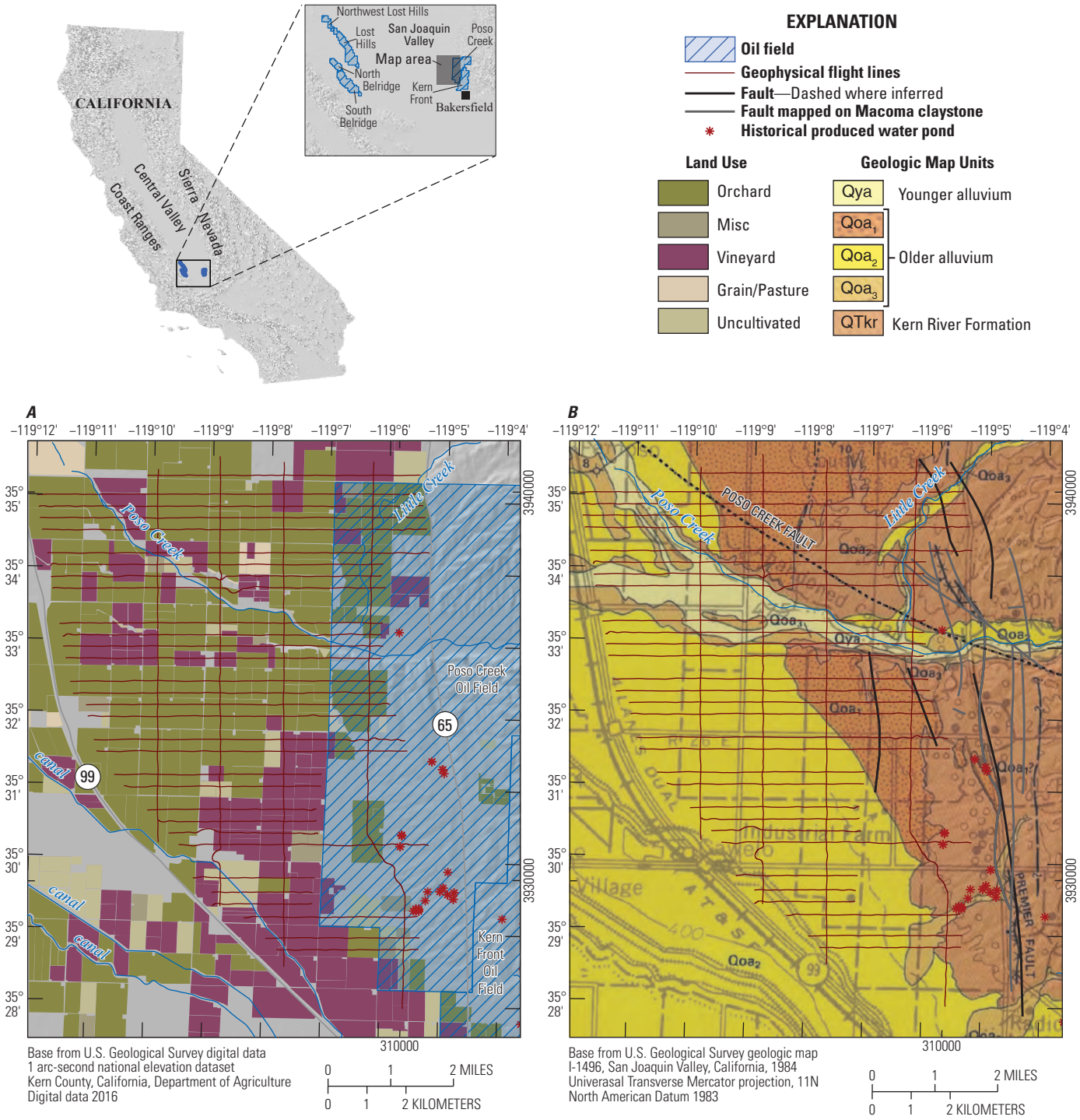

Figure 1. Location of the airborne geophysical survey area near the eastern margin of California's San Joaquin Valley. Location of airborne electromagnetic flight lines shown in dark red at various scales. The inset map (black outline on the hillshade) shows a selection of oil field boundaries (outlined in blue) in the context of the San Joaquin Valley. *A*, Geophysical flight lines and historical produced water ponds shown against oil field boundaries and land use (modified from Kern County Department of Agriculture, 2016) and *B*, Geophysical flight lines and historical produced water disposal ponds (Central Valley Water Board, 2018) shown against modified mapped geology (Bartow, 1984) and faults mapped at the Macoma claystone level from (Weddle, 1959; Jennings and others, 1977). *C*, Hillshade of the State of California showing the general location of the study area.

At a regional scale, the northwest-trending structural trough of the Central Valley is the principal controlling factor of groundwater occurrence and movement (Page, 1986). The Tertiary and Quaternary Kern River Formation and the alluvial and lacustrine sediments, along with the Tulare Formation that occurs west of the study area, make up the primary regional aquifer system in the southern San Joaquin Valley (Faunt, 2009). Groundwater in the Poso Creek area generally occurs under unconfined to semiconfined conditions, and lacustrine clay deposits within the AEM DOI are generally considered to be discontinuous (Cawelo Groundwater Sustainability Agency, 2020). Clay lenses within the primary aquifers may play a role in groundwater flow to different extents (Faunt, 2009).

The southern San Joaquin Valley has an arid climate with the lowest average precipitation rates and highest evapotranspiration rates in the Central Valley (Faunt, 2009). The regional aquifer system is recharged primarily from inflow from the adjacent mountains, infiltration from surface-water features such as streams and unlined or leaky canals, and agricultural irrigation return flows (Faunt, 2009). Local groundwater-flow directions are primarily to the west and north following the general surface drainage patterns towards the low-lying central portion of the valley. Within the study area boundary, Poso Creek is the most prominent stream and runs intermittently from the Sierra Nevada Mountains, flowing west–northwest towards the axis of the Central Valley. Artificial recharge also occurs through groundwater banking programs supplied by a network of surface canals (Cawelo Groundwater Sustainability Agency, 2020).

The depth to the regional water table and the temporal changes in groundwater levels vary throughout the survey area. At the time of the AEM survey (October 2016), the Poso Creek area had experienced several years of dry or critically dry conditions when annual precipitation was well below the average of 15 centimeters per year (Cawelo Groundwater Sustainability Agency, 2020). Groundwater-level declines were observed in monitoring wells for the period between 2007–17, with the lowest water levels being reached in 2016 following an extended dry period beginning in 2014 (CDWR, 2020; USDM, 2021). In the northern and western part of the survey area groundwater-level declines exceeded 50 m (CDWR, 2020). Groundwater-level declines in the eastern part of the survey area were less severe than in the northwest (Cawelo Groundwater Sustainability Agency, 2020). The depth to water from the land surface during 2015–18, close in time to the 2016 AEM survey, ranged from about 125 m in the northwestern survey area to about 190 m in the east (CDWR, 2020). Seasonal water table fluctuations also varied across the study area, but in general were on the order of 5–20 m.

Compiled historical groundwater and produced water TDS information (Metzger and Landon, 2018), along with available well construction information, consist of records from 1930 to 2014. Groundwater wells in the vicinity of the Poso Creek area have a median perforation depth of about 280 m (Metzger and Landon, 2018). Within the Poso Creek oil field, the typical depths at which TDS concentrations exceed 3,000 mg/L has recently been modeled to occur about 600 to 800 m below land surface in the marine units underlying the Macoma claystone (Stephens and others, 2021). Groundwater TDS concentrations in the AEM survey area were typically below 1,000 mg/L (range: 130 to 3,712 mg/L and median: 297 mg/L; Metzger and others, 2018) within the Kern River Formation and overlying sediments, with the maximum historical TDS observation in the southwestern corner of the study area. Clear trends in measured TDS concentrations with respect to perforation depth or time were not evident in the compiled groundwater well records (Metzger and others, 2018; fig. 2). Petroleum wells in the Poso Creek oil field are deeper than typical groundwater extraction wells within the study area with a median perforation depth of 780 m. Produced water TDS concentrations (range: 491 to 6,825 mg/L and median: 1,282 mg/L; Stephens and others, 2018) in the Poso Creek oil field are relatively fresh compared with produced water concentrations in oil fields in the western San Joaquin Valley (Gillespie and others, 2017; McMahon and others, 2018; Metzger and others, 2018) and overlap with concentrations observed in groundwater in the Poso Creek study area (fig. 2*A*).

Methods

In October 2016, AEM and magnetic data were acquired by SkyTEM Surveys ApS using the SkyTEM-312M helicopter-borne transient electromagnetic system and a Geometrics G822A cesium vapor magnetometer. Transient electromagnetic systems use a pulse of electrical current through a large loop of wire to generate a primary time-varying magnetic field. This primary magnetic field induces electrical current to flow in the subsurface, leading to secondary magnetic fields that vary, in part, as a function of the resistivity structure of the sampled geologic volume. The resulting decay in the secondary magnetic field is measured by receiver coils after the transmitter is turned off. The SkyTEM-312M AEM system uses dual-moment transmitters housed in a rigid airframe. The high-moment transmitter (about 500,000 ampere square meters [$A \cdot m^2$]) maximizes the depth of investigation through a multiturn loop with larger effective transmitter area and higher current; the low-moment transmitter (about 4,000 $A \cdot m^2$) achieves a faster turnoff time by using a lower current and smaller effective transmitter area, allowing early-time data collection and improved sensitivity to the shallow resistivity structure (Sorensen and Auken, 2004). Ancillary positional instruments, including global positioning system receivers, laser altimeters, and inclinometers, are mounted to the airframe and record the sensor's geographic location, height above ground, and airframe orientation. Details of the SkyTEM-312M system deployed for the Poso Creek survey are provided in the contractor's report that is included with the digital data release associated with this report (Zamudio and Ball, 2022).

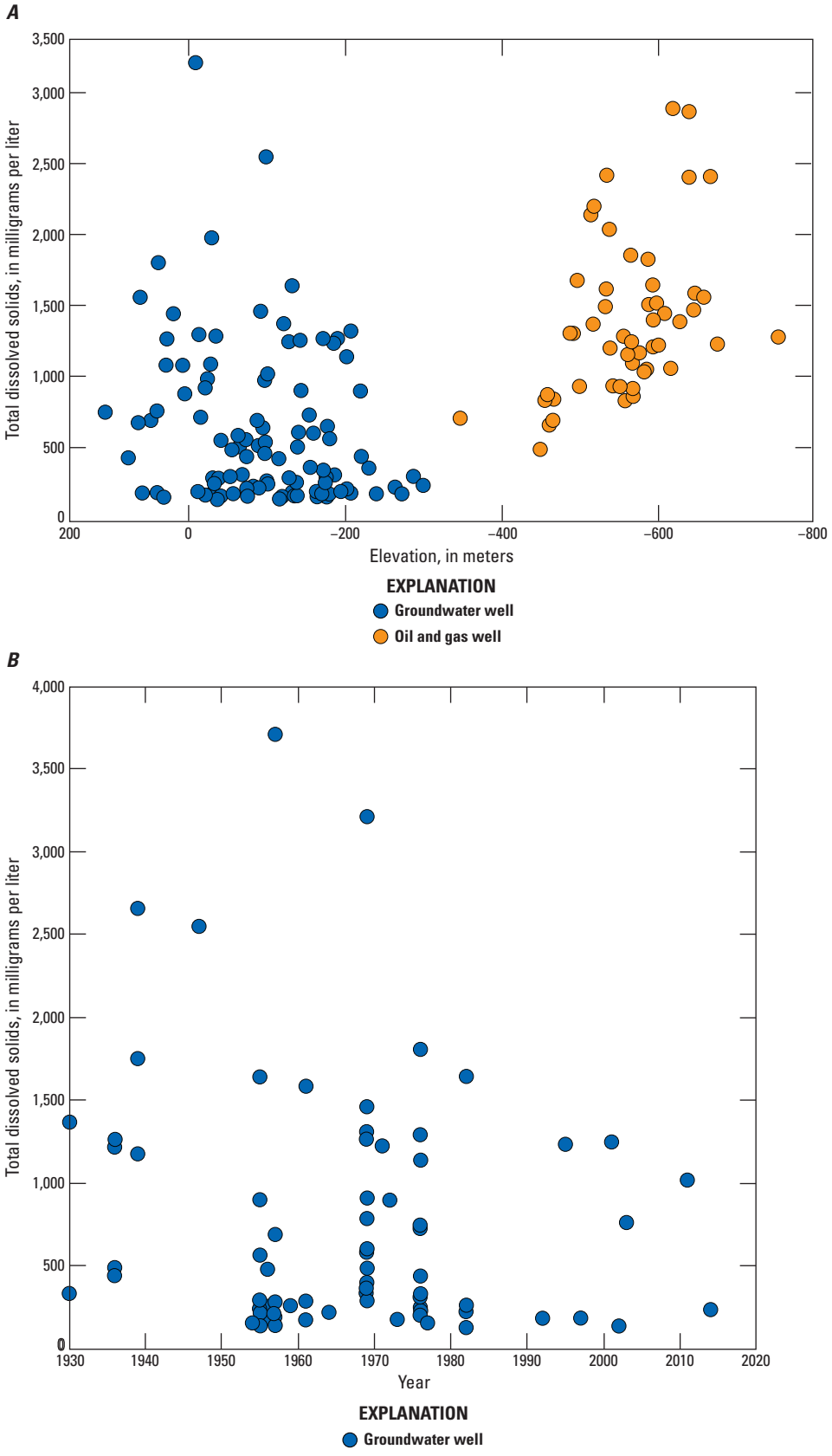

Figure 2. Historical total dissolved solids concentrations from groundwater and oil and gas wells in and near the Poso Creek survey area in California. Total dissolved solids concentration shown with respect to *A*, perforation elevation and *B*, measurement year. Data from Metzger and others (2018) and Stephens and others (2018).

The Poso Creek survey consists of 262 line kilometers flown over an area to the west of the developed parts of the Poso Creek oil field (fig. 1). The survey was flown as a series of closely spaced parallel lines (referred to as block lines) intersected by more widely spaced, perpendicular tie lines. Block lines have an east–west orientation and a nominal 300 m spacing; tie lines have a north–south orientation and a nominal spacing of 1,500 m. Data collection was prioritized in the area 5 km downgradient of the actively developed western margin of the Poso Creek oil field. California State Route 99, a major highway leading out of Bakersfield, was the western boundary of the AEM survey, as regular crossing of the highway was logistically unfeasible (fig. 1). In the survey area, land-surface elevations vary from about 120 to 220 m, rising smoothly to the east toward the Sierra Nevada Mountains. Survey altitude was draped to the terrain with a nominal altitude of 35 m. Actual sensor altitude averaged 37 m above land surface with variability resulting from terrain and clearance above obstacles like trees and powerlines. Christiansen and others (2019) modeled a 100 m by 100 m sensitivity footprint in the near-surface for the SkyTEM system at similar altitudes over a 30 ohm-meter (Ω•m) half space, though this footprint varies with resistivity.

SkyTEM Surveys ApS performed preliminary basic data processing, including a merge of all sensor data to a uniform 10 hertz (Hz) sampling frequency, tilt correction, and positional shifts to the center of the airframe. The magnetic data collected at the same time as the AEM data were diurnally corrected using locally deployed base stations and corrected for the International Geomagnetic Reference Field. The residual magnetic anomaly was calculated from the corrected magnetic data. Preliminary AEM data processing included primary-field correction to early-time data, normalization for transmitter moment, and adaptive noise filtering. Data acquisition and contractor-performed processing are described in further detail in the supporting documentation and the contractor's report included in the digital data release (Zamudio and Ball, 2022).

Upon delivery of the contractor-processed data, more detailed AEM data processing was performed at the USGS. Altimeter data were filtered and manually corrected as necessary to remove false heights associated with laser reflections on vegetation or other above-ground features. Minimally processed AEM data were manually culled for cultural noise such as powerlines, pipelines, and some vineyards, which can impact the AEM signal. Trapezoidal averaging filters were then applied to improve signal-to-noise ratios. Low-signal and noisy data in late-time measurements were ultimately culled from the processed data through a combination of filters and manual culling. Data processing procedures are described in more detail in the supporting documentation provided with the digital data release (Zamudio and Ball, 2022).

The processed AEM data were used to develop models of subsurface resistivity through a spatially constrained inversion (SCI) using the deterministic inverse modeling code AarhusINV (Viezzoli and others, 2008; Auken and others, 2015) implemented in Aarhus Workbench software (Aarhus Geosoftware, 2019). A smooth modeling scheme was used with 30 fixed-depth layers, where each layer increases in thickness from 4 to 32 m as the layer interface depth increases from 4 to 400 meters. The SCI approach produces a quasi-3D conductivity model by using Delaunay triangulation to build spatial constraints (Viezzoli and others, 2008). The starting resistivity for all model layers was 30 Ω•m, and loose lateral and vertical constraints on resistivity were chosen to allow for rapid transitions in resistivity between layers and adjacent processed data points. Inversion model parameters were selected by iterating on various parameter combinations and evaluating the resulting resistivity model. The suite of resistivity model results was evaluated for changes in model resistivity with depth, spatial consistency along and between flight lines, and the ability to recover similar resistivity values and structure to those observed in historical borehole geophysical logs collected in oil and gas exploration wells that were logged in the upper 400 m and closely located to the AEM flight lines (CALGEM, 2020). Details regarding all settings used in the development of the SCI are provided in Zamudio and Ball (2022).

The sensitivity of AEM data to resistivity at depth varies as a function of the resistivity structure of the subsurface and the AEM system parameters. DOI estimation gives a sense of the depth limit at which an individual resistivity model is less well-constrained by the data and more heavily influenced by model parameters and is therefore less reliable for estimating subsurface resistivity values. For the Poso Creek survey, two DOI cutoff limits were estimated for each data point using the cumulative sensitivity approach developed by Christiansen and Auken (2012) and implemented in Aarhus Workbench. A conservative upper DOI limit was estimated by comparing resistivity at depth from multiple models using various regularization parameters; above the upper DOI limit, modeled resistivity is fairly robust regardless of model settings. A less conservative lower DOI limit was also estimated. This lower DOI limit generally recovers transitions in resistivity expected from nearby borehole geophysical logs; however, the values of resistivity in this lower DOI range are less well-constrained than those modeled above the upper DOI limit. The model structure above the lower DOI limit captures general trends in resistivity at depth, whereas resistivity values above the upper DOI limit are more reliable for quantitative uses.

Results

Inverted resistivity models serve as the primary result of the AEM survey. The AEM inverted models are shown as a combination of resistivity cross sections along flight lines (appendix 1, figs. 1.1−1.35), resistivity depth slices, and resampled models at selected constant elevation bands 5 m thick. The AEM models from the Poso Creek survey area show a resistivity range from 3 to 64 Ω•m with a mean resistivity of 16 Ω•m (figs. 3 and 4). The DOI ranges from 34 to 431 m below land surface (fig. 4). The mean lower DOI is 293 m

whereas the mean upper DOI is 229 m. The resistivity models are completely masked below the lower DOI limit (figs. 3 and 4), and a grey line marks the upper DOI limit (fig. 4). The deepest DOI from the survey is about 430 m; therefore, the AEM data are sensitive to the lithologic characteristics and fluid properties of the Kern River Formation and overlying alluvial sediments. In general, the resistivity structure of the area shows a series of west-dipping layers that tend to thicken to the west (fig. 4). These west-dipping layers are consistent with the general orientation of the geologic units in this area (Kodl and others, 1990).

The highest resistivity layer is near the surface in the unsaturated alluvial sediments and ranges in thickness from 10 m to more than 100 m. The resistivity of this layer is generally greater than 18 Ω•m, and the layer thickens to the west across the survey area (figs. 3 and 4). From an aerial view, the most resistive parts of this layer can be seen near the Poso Creek drainage region from the hills on the east to the western margin of the survey where it fans out along Poso Creek drainage and to the south. Lens-shaped moderate resistivity layers (8–18 Ω•m) are common within this higher resistivity layer across the study area. These lenses are relatively uniform in depth and somewhat intermittent to the west, and more discontinuous with increasing vertical interruptions to the north and east. Figure 4 shows examples of these moderate-resistivity lenses and their spatial variation (fig. 4*C–E*). In some cases, interruptions in the extent and orientation of these lenses correspond to mapped normal faults (Bartow, 1984; Jennings and others, 1977; Weddle, 1959), particularly in the northeastern part of the survey area where faults are more commonly mapped (fig. 4*A–B*).

Underlying the high-resistivity surface layer, resistivity generally becomes more moderate (8–18 Ω•m) to relatively conductive (< 8 Ω•m) and shares the general trend of dipping and thickening to the west (fig. 3*C–F*, fig. 4). The elevation slices (fig. 3*D–F*) show resistivity in this moderate to relatively conductive range predominating in the western part of the study area below an elevation of about 10 m. As seen in figure 3, resistivity generally decreases, and contrasts become more muted with depth; however, the general trend and layered structure persists to the lower DOI limits (fig. 4).

Hydrogeologic Controls on Resistivity

Bulk resistivity is controlled by a combination of geologic conditions and fluid properties, including sediment saturation, salinity, lithologic texture and composition, clay and mineral content, and temperature (Keller and Frischknecht, 1966). Hydrogeologic interpretation of resistivity data requires consideration of these controlling factors, along with evaluation of available supporting information such as description of geologic materials from drillers logs, measurements from geophysical logs, observations of groundwater levels and salinity, and consideration of the general hydrogeologic setting. High natural thermal gradients are not expected to occur in the immediate survey area, although anthropogenic heat sources, such as from enhanced oil recovery techniques like steam flooding, do occur to the east of the survey area within the active parts of the Poso Creek oil field. However, steam flooding near the western oil field margin occurs primarily below the Macoma claystone, at depths of more than 500 m; the AEM survey extent is restricted to the Kern River Formation and alluvial materials overlying the Macoma claystone and west of the steam flooding activities (fig. 5). The Macoma claystone is expected to act as a confining unit limiting advective heat transport to shallower depths, and this in addition to the three dimensional separation is likely to limit substantial thermal anomalies from occurring within the AEM survey area. Therefore, temperature variations are assumed to not substantially influence the resistivity structure in the survey area. Conductive minerals other than clay, such as those associated with substantial hydrothermal deposits, are also not expected to occur within the survey area. As such, groundwater salinity, saturation, clay content, and lithologic texture are likely to be the most influential controls on the resistivity structure of the survey area. The resistivity depth slices, elevation slices, and cross sections were used to compare AEM-derived resistivity to the lithology, estimated water table elevation, and salinity information available from public data sources (Metzger and others, 2018; California State Water Resources Control Board, 2020) to build an understanding of the relative impacts of these factors on the observable resistivity structure of the Poso Creek survey area. Additionally, borehole geophysical logs from oil and gas wells (CALGEM, 2020) were used to evaluate the consistency of the AEM-derived resistivity to independent and older measures of resistivity structure.

Lithology influences bulk resistivity through clay content, porosity, and pore shape; high clay content and finer-grained materials are generally lower in resistivity in comparison to coarser-grained materials. Correlations between mapped surface geology and shallow resistivity highlight the sensitivity of the AEM-derived resistivity to changes in geologic composition within the Poso Creek survey area. To further evaluate local correlations between lithology and AEM-derived resistivity at depth within the saturated zone, descriptions from driller's logs (CDWR, 2020) near the AEM flight lines were summarized into clay-bearing or non-clay-bearing categories following similar criteria to those used by Christiansen and others (2014) to relate clay fractions to AEM results in other sedimentary environments. Figure 6 shows an example of classification based on drilling descriptions. Comparisons between resistivity structure and these lithologic classifications near flight lines (fig. 4) commonly show an observable correlation between predominantly fine grained and clay-bearing layers and moderate to relatively conductive AEM resistivity. An alternative classification scheme was explored, where layers described in driller's logs were sorted into a coarse- and fine-grained binary classification (Faunt, 2009). Both schemes generally result in similar classifications and therefore correlations to AEM-derived resistivity structure. The clay-bearing binary classification

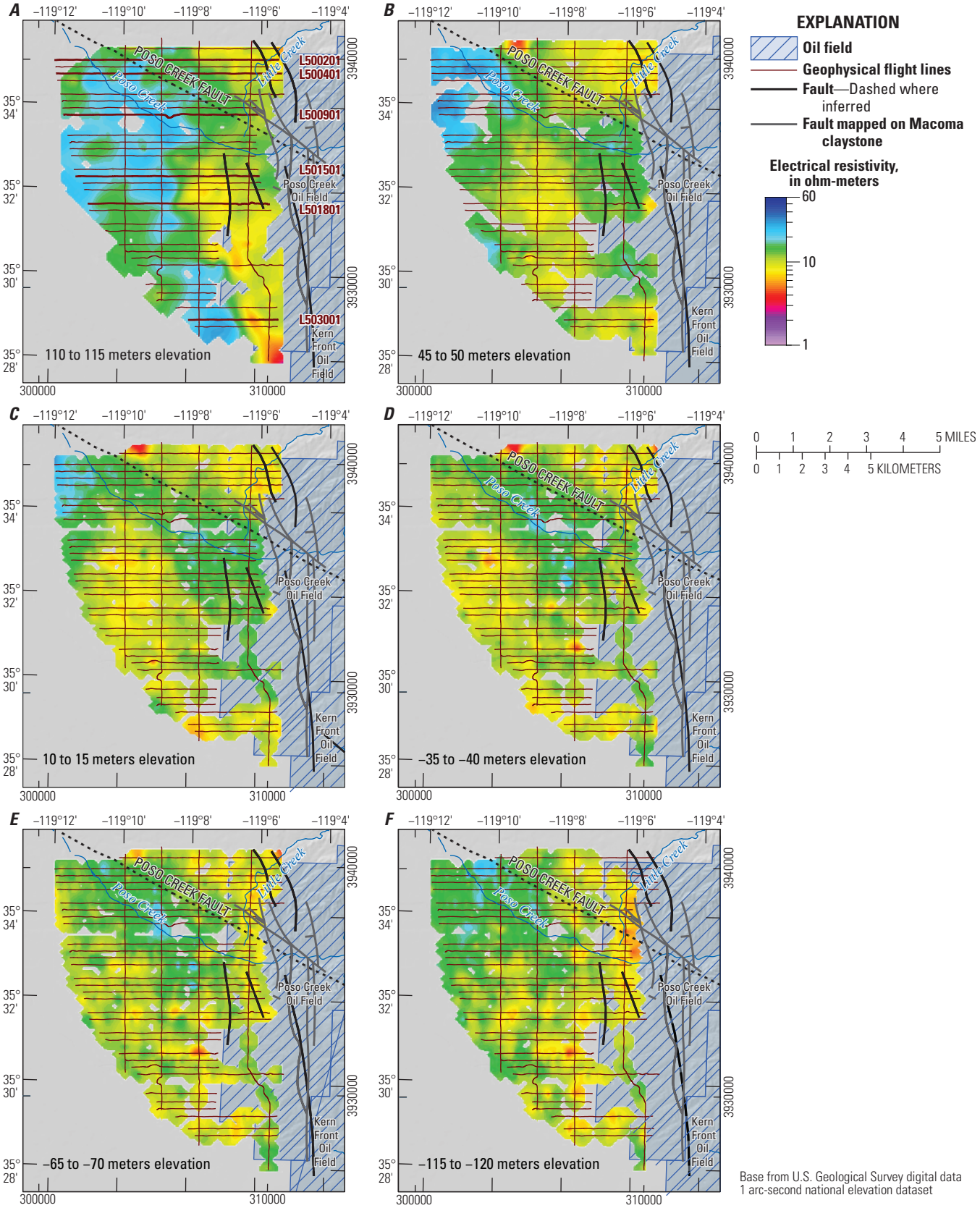

Figure 3. *A–F,* elevation slices of the airborne electromagnetic-derived resistivity models shown alongside oil field boundaries (blue squares), Poso Creek drainage, the Poso Creek Fault (dotted line), faults mapped at the Macoma claystone (solid black lines; Weddle, 1959; Jennings and others, 1977) and geophysical flight lines (dark red). Bolded and labeled Geophysical flight lines in *A*, show location of selected lines shown in figure 4.

was determined to be the most comparable to the AEM results and chosen as the primary scheme for this report, although in some cases, the coarse-fine classification was more comparable.

Although available lithologic logs in the study area have several drawbacks (they are spatially limited, the location accuracy may vary, and the reliability and level of detail in these descriptions varies), the correlation between resistivity structure and lithologic descriptions suggests that lithologic variability, especially clay content, is a controlling factor for some resistivity contrasts in the Poso Creek area. The correlation also confirms that the AEM-derived resistivity is accurately representing the depths of general lithologic transitions. For example, in section L501501 (fig. 4*D*), well 27S26E34A shows a correlation in the depth of the transition from mostly coarse-grained units to more consistently clay-bearing units mirroring the resistivity transition from the upper 20 Ω•m layer to the underlying lower resistivity layers at about 100 m below ground surface or an elevation of about 50 m. The decrease in resistivity is correlated with the increased frequency of clay-bearing materials with depth (fig. 6). Lithologic controls on resistivity have been documented in nearby parts of the Kern River Formation (for example, Negrini and others, 2009) where the groundwater has comparable salinity. Similar correlations between mostly clay-bearing and fine-grained materials and lower resistivity are apparent in other locations throughout the survey area and support a general sensitivity to lithologic texture throughout the DOI.

Saturation impacts bulk resistivity through increasing the relative volume of pore fluids (Archie, 1942), and as such, changes in relative saturation, such as across the water table of an unconfined aquifer, can lead to observable changes in bulk resistivity (for example, Turesson, 2006). To evaluate the relative impact of saturation on resistivity in the Poso Creek area, an approximate map of the local water table was developed using groundwater-level monitoring records available from the California Department of Water Resources Water Library Statewide database (CDWR, 2020). Because of seasonal and long-term fluctuations in the groundwater levels observed in the Poso Creek area, and particularly considering the declining water levels between 2006–16 (Cawelo Groundwater Sustainability Agency, 2020), measurements taken in the fall 2016 are the most relevant for comparison to the AEM survey. Given the limited spatial coverage of wells sampled in the fall 2016, particularly in the northern portion of the survey area, additional wells with water-level measurements taken in the fall between 2014–17 were also taken into consideration. Minimum-curvature gridding was used to interpolate water table elevations between wells, shown as the dashed lines projected onto the sections in figure 4.

In the northwestern part of the survey area, the notable transition from the high to moderate resistivity layers correlates to the approximated water table elevation (figs. 4*A–B*). In this area, driller's logs suggest that lithologic transitions are also closely located in depth to the water table elevation, which makes it difficult to fully attribute that resistivity contrast to either saturation or lithology. Bartow (1984) indicated a transition from alluvial sediments to the Kern River Formation at about 0-m elevation in a cross section through the northern part of the survey area, similar to the elevation observed for the major transition from relatively high to moderate resistivity (fig. 4*A*). This major resistivity transition to the east and south becomes more strongly associated with lithology and the dipping sedimentary structure and less coincident with the approximated water table elevation, which available measurements suggest was much flatter than the most dominant resistivity layering (fig. 4). More muted transitions in resistivity are observed in places that correlate to the water table elevation, such as in the easternmost portions of sections L500401 (fig. 4*B*), L500901 (fig. 4*C*), and L501801 (fig. 4*E*), but the signature associated with the approximated water table elevation is not spatially consistent and likely varies due to the changes in overall lithologic texture. Saturation does influence the resistivity structure, but detailed interpretations of the water table elevation from the AEM-derived resistivity with the available water-level measurements would be difficult given the relative influence of the layered and faulted geology. More widely distributed contemporary water-level measurements would improve the accuracy of the approximation of the water table across the survey area and could be helpful for interpretation of the AEM results.

Figures 4.—Following pages *A–F,* six selected sections showing airborne electromagnetic-derived resistivity models plotted with nearby lithologic logs and borehole geophysical logs. The approximated fall 2016 water table elevation and faults indicated in surficial mapping by Bartow (1984) and Jennings and others, 1977 and faults at the Macoma claystone by Weddle (1959). Data from nearby boreholes are projected onto the sections: lithologic logs are classified by presence of clay in the driller's description; Resistivity measurements from borehole geophysical logs are shown using the same color scale as airborne electromagnetic models. Profiles are plotted alongside a geologic map showing the surficial geology (Bartow 1984). The geologic map is centered along the flight path (solid line) with lithologic log locations. Geologic map units and symbols are described in figure 1*B*. Location of airborne electromagnetic cross sections are shown in bold on figure 3*A*.

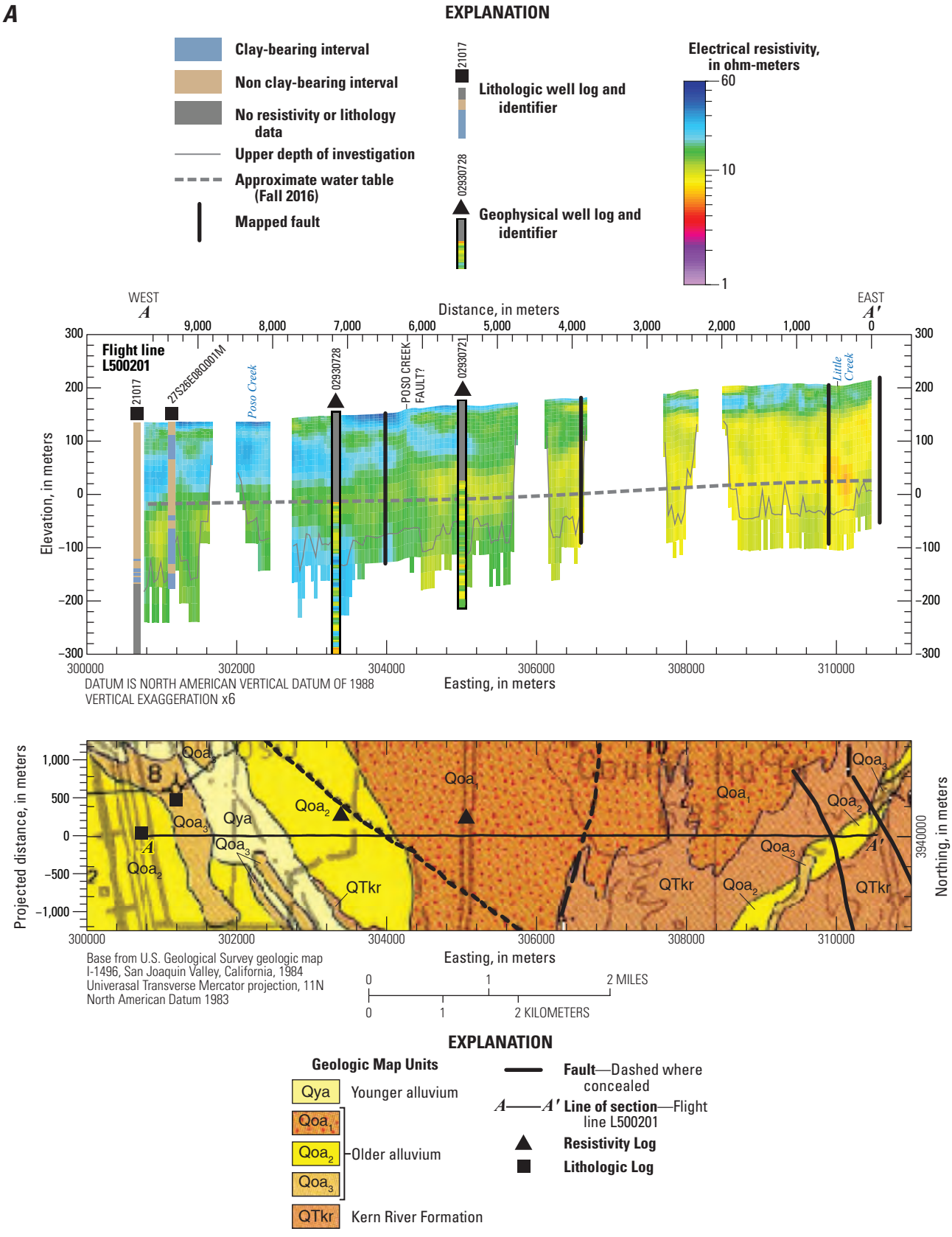
A
EXPLANATION
Clay-bearing interval
Non clay-bearing interval
No resistivity or lithology data
Upper depth of investigation
Approximate water table (Fall 2016)
Mapped fault
21017
Lithologic well log and identifier
02930728
Geophysical well log and identifier
Electrical resistivity, in ohm-meters
60
10
1
WEST
A
Distance, in meters
EAST
A′
9,000
8,000
7,000
6,000
5,000
4,000
3,000
2,000
1,000
0
Flight line L500201
21017
27S26E08Q001M
Poso Creek
02930728
POSO CREEK FAULT?
02930721
Little Creek
Elevation, in meters
300
200
100
0
−100
−200
−300
300000
302000
304000
306000
308000
310000
Easting, in meters
DATUM IS NORTH AMERICAN VERTICAL DATUM OF 1988
VERTICAL EXAGGERATION x6
Projected distance, in meters
1,000
500
0
−500
−1,000
B
A
A′
Qoa3
Qoa2
Qoa1
Qya
QTkr
Northing, in meters
3940000
Base from U.S. Geological Survey geologic map I-1496, San Joaquin Valley, California, 1984
Universal Transverse Mercator projection, 11N
North American Datum 1983
0
1
2 MILES
0
1
2 KILOMETERS
EXPLANATION
Geologic Map Units
Qya
Younger alluvium
Qoa1
Qoa2
Qoa3
Older alluvium
QTkr
Kern River Formation
Fault—Dashed where concealed
A——A′ Line of section—Flight line L500201
Resistivity Log
Lithologic Log

Figure 4.

B

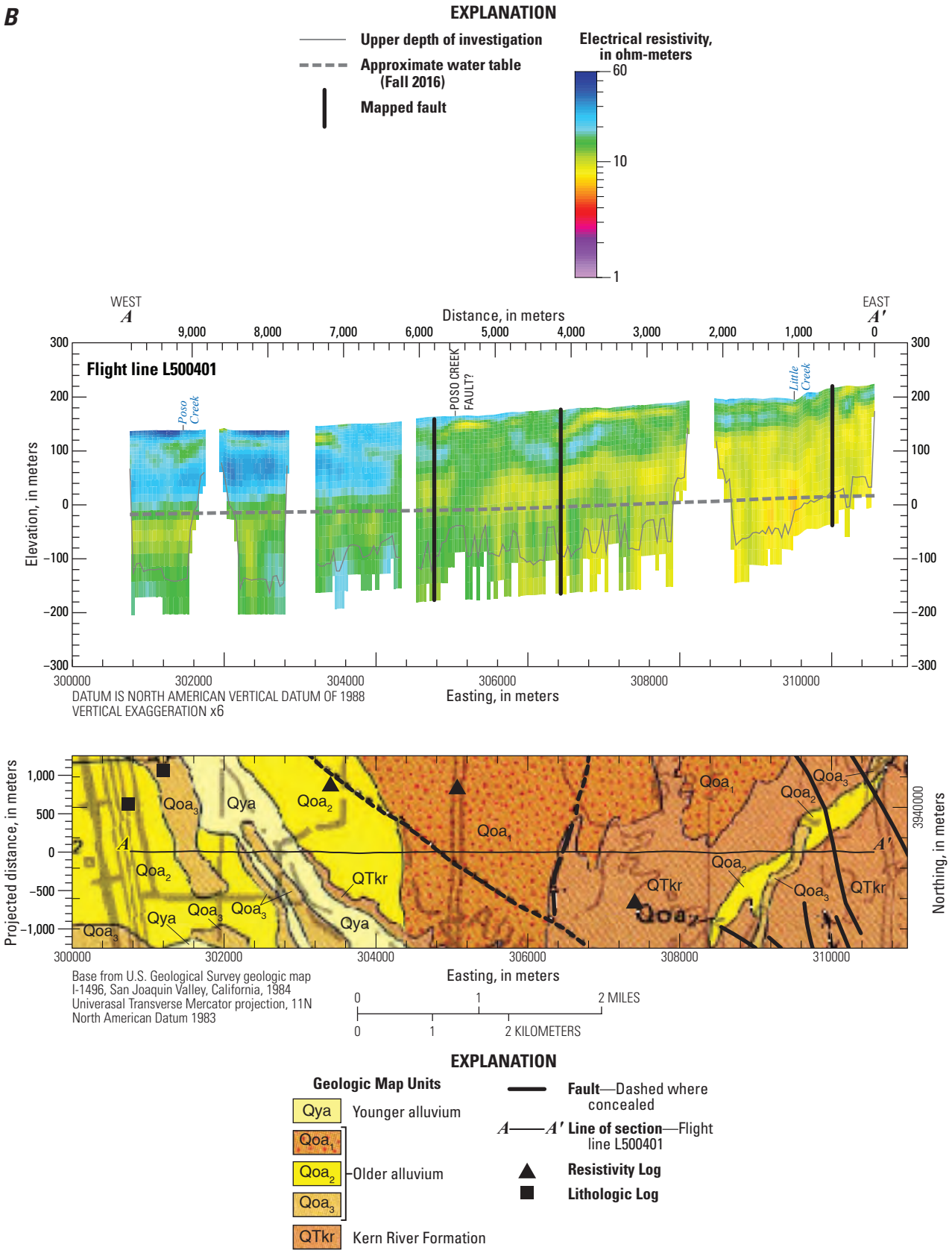

Figure 4. —Continued

C

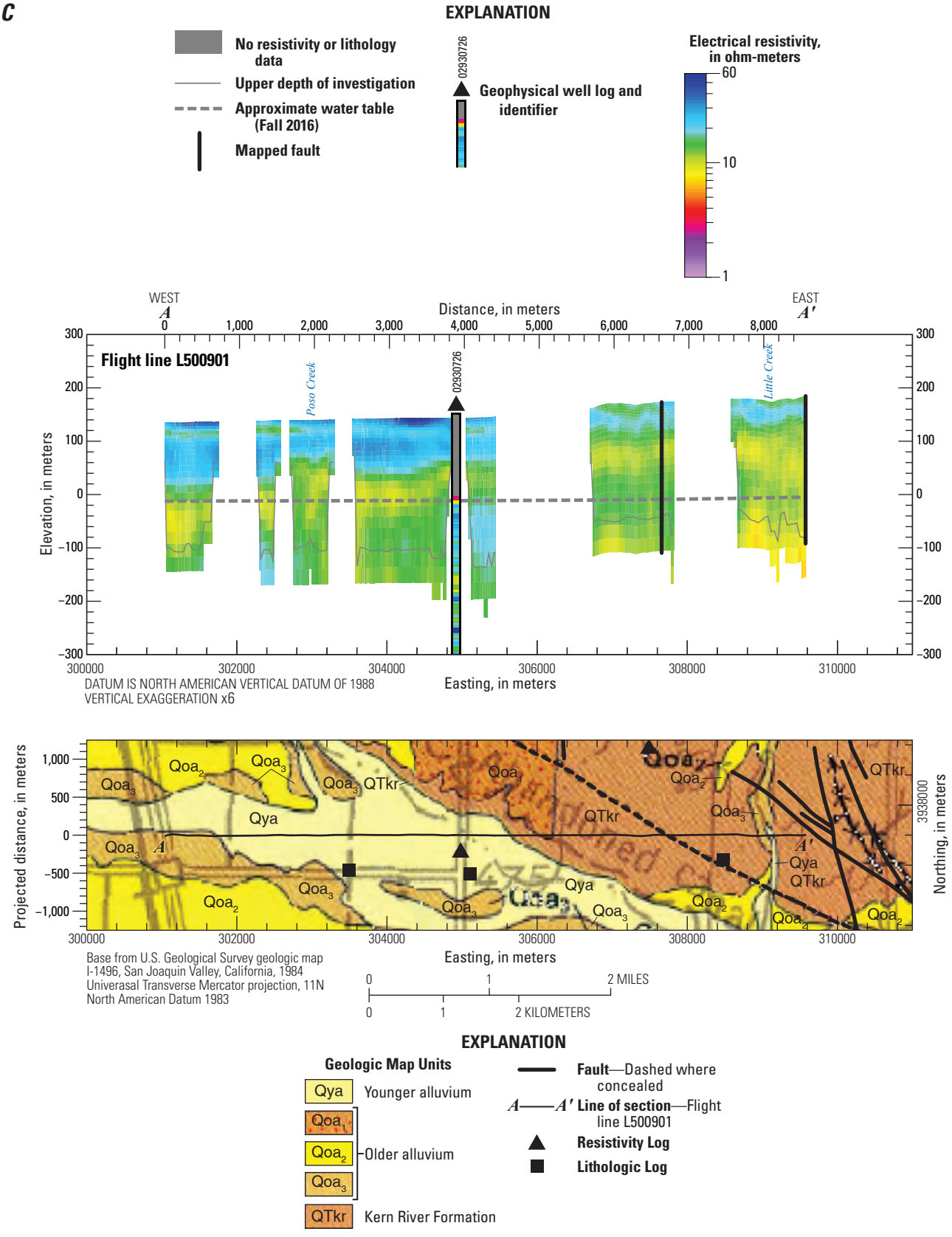

Figure 4. —Continued

D

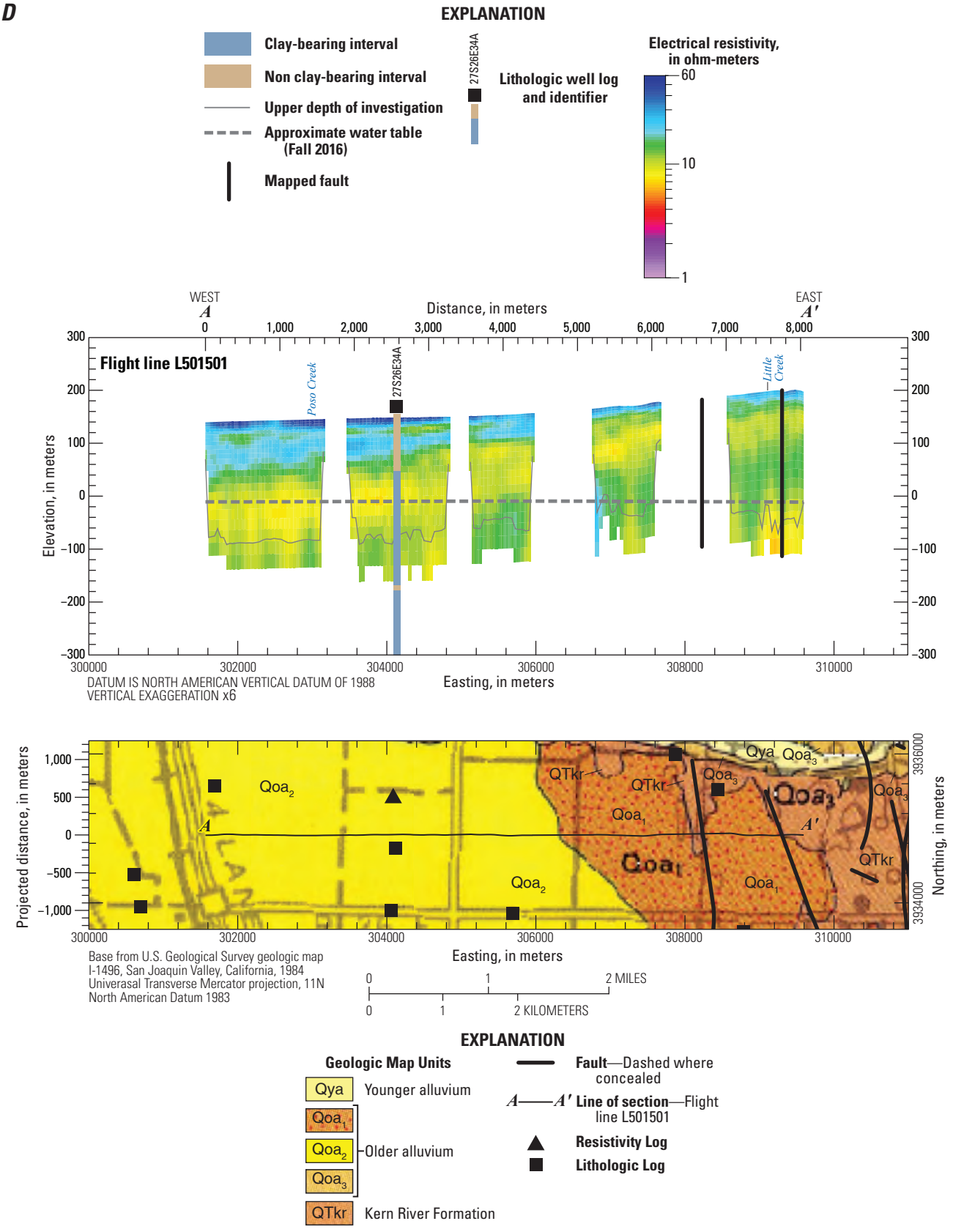

Figure 4. —Continued

E

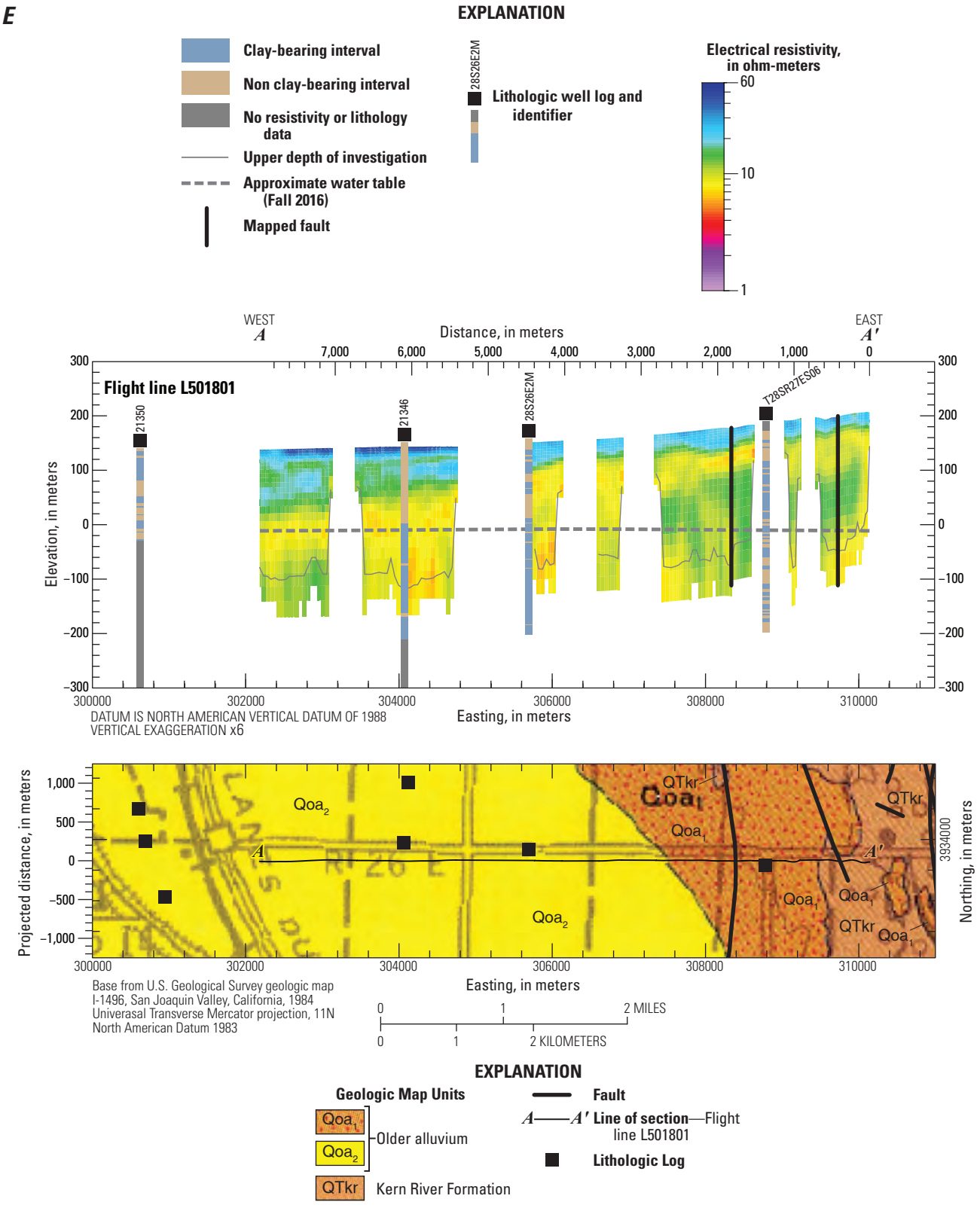

Figure 4. —Continued

F

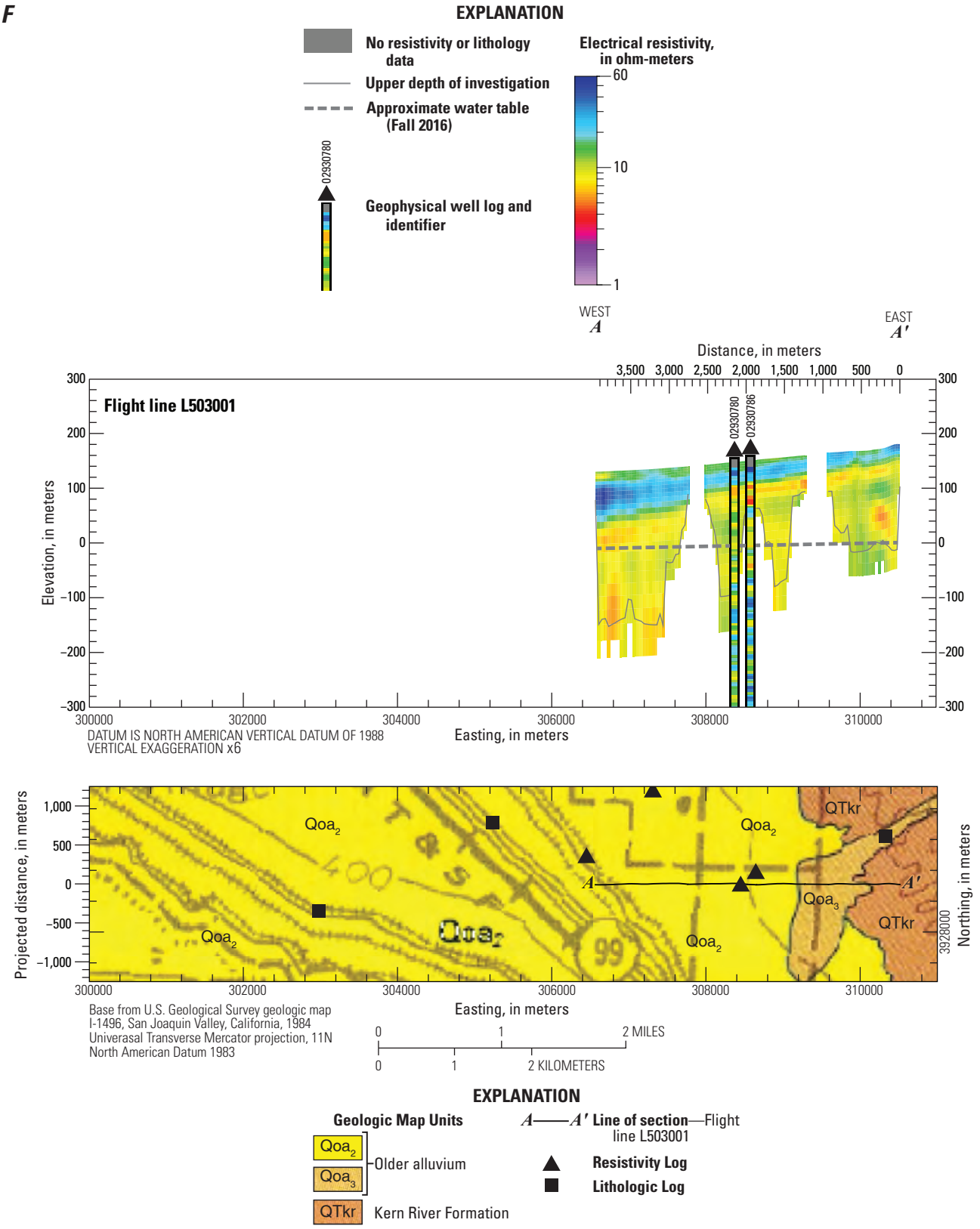

Figure 4. —Continued

Groundwater salinity strongly influences bulk resistivity, with higher groundwater TDS concentrations leading to enhanced fluid conductivity and overall reduced bulk resistivity. The relation between fluid conductivity and TDS concentration is well documented and illustrated by petrophysical relations (for example, Archie, 1942). Analyses of borehole geophysical logs have been used in several geologic settings to map salinity using bulk resistivity with collocated information about porosity and relative clay content, including recently in the Poso Creek oil field immediately east of the survey area (Stephens and others, 2021). Similar interpretations of AEM survey results, where only bulk resistivity information is uniformly available, often rely on observational relations between TDS and bulk resistivity (for example, Ball and others, 2020). Historical groundwater and produced water TDS concentrations compiled by Metzger and others (2018), supplemented by additional data reported by the State Water Board's Groundwater Ambient Monitoring and Assessment program online database (California State Water Resources Control Board, 2020) were compared to nearby AEM-derived bulk resistivity. These observations represent a mixed sample period (1930–2020) in the immediate vicinity of the AEM survey and cover a range of perforation depths from 50 to 1400 m, an equivalent of about 150–1,200 m in elevation. The available historical data do not show obvious trends in TDS concentrations with depth or time, suggesting that comparing the historical TDS concentrations to the 2016 resistivity values derived from the AEM survey may be valid (fig. 2). Furthermore, AEM resistivity and nearby borehole geophysical logs from oil and gas wells (CALGEM, 2020), collected between 1939–71 (table 1) are also generally comparable in both resistivity value and resistivity structure in many locations (fig. 4). In figure 4, these borehole resistivity logs are plotted against the AEM sections using the same color scale. Borehole resistivity is shown with a 10 m moving window average filter to reduce the vertical resolution of the borehole log to be more comparable to the resolution of the AEM. The typical similarities in structure and value suggest that the subsurface resistivity has not shifted substantially over time and further support that the comparison between 2016 resistivity and relatively old and mixed-age TDS observations may be reasonable for the Poso Creek area.

Table 1. Year borehole geophysical logs were collected in the vicinity of the Poso Creek airborne electromagnetic survey.

Well number	Year resistivity log collected
02930717	1965
02930721	1947
02930726	1955
02930728	1961
02930764	1963
02930774	1964
02930780	1939
02930786	1964
02949410	1971

Figures 7 and 8 show a series of comparisons between AEM-derived bulk resistivity and the historical TDS water-sample records. Figures 7*A* shows resistivity maps sampled at the approximated fall 2016 water table elevation and figure 7*B* shows resistivity maps sampled at a constant 50 m offset below the fall 2016 water table elevation (shown as contour lines) as a representation of resistivity trends in the upper part of the saturated zone. For wells with multiple records prior to 2006, the median TDS value is shown. For wells with samples taken between 2006–20, the sample taken closest in time to 2016 is shown as the most relevant for comparison to the AEM results. Available well construction information (Metzger and others, 2018) indicated that wells tend to have top perforations near the water table with relatively long screened intervals (median screen length 160 m). It is assumed that most other undocumented wells are similarly constructed and valid for comparison but acknowledged that some of the TDS samples shown (fig. 7, square symbols) may not be representative of conditions within the AEM DOI. Within the survey area, TDS is commonly less than 1,500 mg/L, but historical records suggest that in some places, TDS can exceed 2,000 mg/L, and there is a general tendency for TDS to increase towards the west and south (fig. 7). Although the resistivity models also show a general decrease in resistivity to the southwest, particularly near the water table (fig. 7*A*), this broader trend may be inherited from the dipping units that pass below the water table elevation and related, at least in part, to lithologic texture (fig. 4*D* and 4*F*). Similar resistivity values (8–10 Ω•m) occur in the northeastern portion of the saturated zone where TDS measurements, although sparse, have historically been less than 500 mg/L (fig. 7). Throughout the survey area, resistivity shows a slight tendency to increase with depth below the water table (fig. 7*A* and 7*B*), but the long perforation depth intervals associated with the available sample record do not allow us to explore the general relations between TDS and resistivity with depth. The mean resistivity of the full modeled depth of the saturated zone above the upper DOI (fig. 7*C*) shows similar overall spatial trends to those seen in the more discrete resistivity elevation slices (fig. 7*A* and 7*B*). Comparisons between this mean saturated resistivity with median TDS from wells with known overlapping perforation depth interval elevations further indicate a limited measurable dependence between AEM-derived bulk resistivity and TDS (fig. 8). These observations suggest that in the Poso Creek region, changes in clay content and lithologic texture have a stronger influence on resistivity than groundwater salinity given the range of TDS concentrations in the area. Some observed variations in resistivity likely are the result of relative changes in groundwater salinity, but quantitative mapping of salinity variations between 100 to 2,000 mg/L from the resistivity structure cannot be reasonably accomplished without directly addressing other spatially varying factors, such as changes in clay content and lithologic texture.

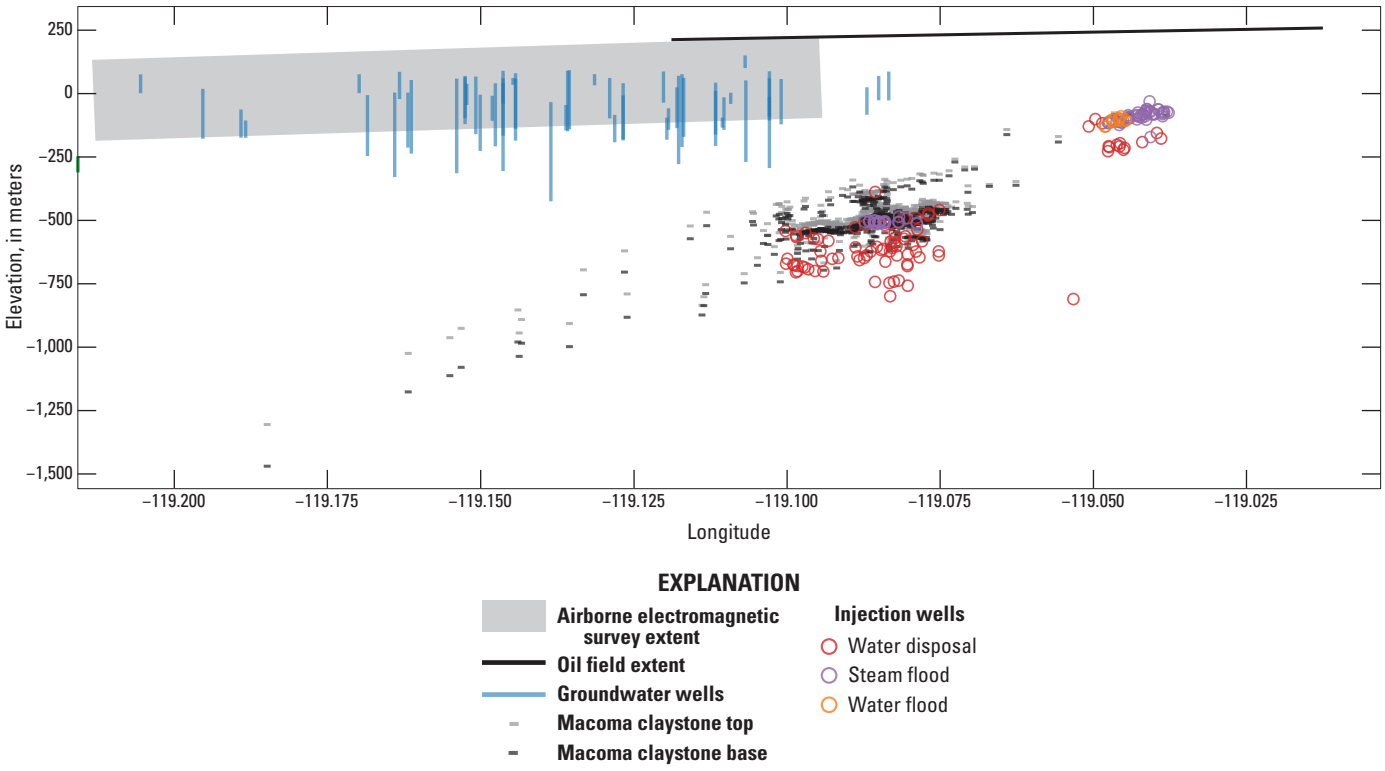

Figure 5. Spatial relation between fluid injection within the Poso Creek oil field administrative boundary, groundwater wells, and airborne electromagnetic survey area. Injection occurs below the Macoma claystone and below the mean lower depth of investigation of the airborne electromagnetic survey. Data compiled from Davis and others (2018a), Metzger and others (2018) and Stephens and others (2018).

Discussion

Based on the above observations, the resistivity structure of the Poso Creek region shows the strongest sensitivity to lithologic texture and clay content, with saturation and salinity having more muted and less spatially consistent observable impacts on resistivity. Based on the relationships to the mapped surficial geology and the general correlation to lithology from driller's logs (figs. 1, 3, 4, and 6), the high-resistivity layer (>18 Ω•m) that occurs near the land surface across most of the survey area is likely indicative of an unsaturated, coarse-grained alluvial layer that thickens and fans out to the west. This resistive layer extends farther south-southwest from the active channel of Poso Creek (fig. 3). Within this high-resistivity layer, relatively thin moderate resistivity layers (8–18 Ω•m) occur in places (fig. 4). These layers are most prominent in the flatter terrain of the western half of the survey and are generally discontinuous. Although little lithologic information from driller's logs is available in these layers, it is possible that they are fine-grained or clay-bearing deposits within the coarser-grained alluvium. Another possibility is that the reduced resistivity is the result of increased saturation in discontinuous perched aquifers. Perched aquifers in the upper zones of the Kern River Formation have been noted by Coburn and Gillespie (2002). Transitions across the approximated fall 2016 water table in deeper parts of the survey area can exhibit similar contrasts in resistivity to those seen in these features. Both suggested explanations indicate heterogeneities in the shallow parts of the aquifer that may affect the downward movement of water through the unsaturated zone.

At greater depth, resistivity generally transitions to a more conductive unit that, based on the dip and increasing thickness to the west, is most likely indicative of finer grained and higher clay-content alluvium of the Kern River Formation (Bartow, 1984). Internal layering in resistivity at depth is likely the result of a combination of changes in lithologic texture and clay content, while some changes could be the result of increasing saturation across the 2016 water table and local variability in groundwater salinity (fig. 4). Additional interpretation of the AEM-derived results, such as the development of high-resolution clay fraction or lithologic texture models in support of groundwater model development, could be undertaken with these AEM results, particularly with additional detailed lithologic descriptions (for example, Gunnink and Siemon, 2015; Knight and others, 2018).

Interruptions in the resistivity layering are commonly correlated with previously mapped faults (fig. 4). The northwest trending Poso Creek Fault is mapped near an interruption in the vertical resistivity layering seen in cross sections (fig. 4*A*–*C*), showing a lateral break (down to the southwest) in

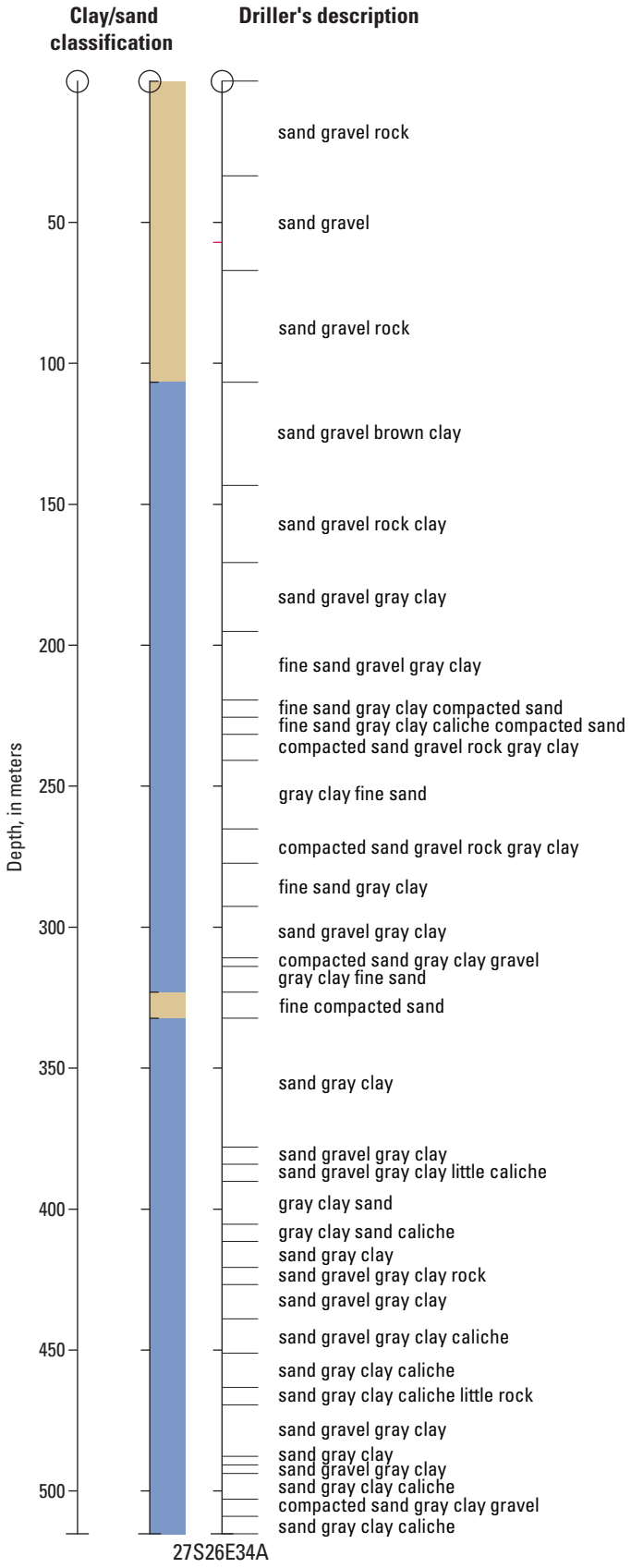

the deeper conductive fine-grained or clay-bearing layer suggesting some vertical offset. Within the survey area, the trace of the Poso Creek Fault is buried and approximately mapped at different locations on various maps (for example, Bartow, 1991); the interruption in resistivity layering can be used to establish a more precise location of a buried fault trace, which would be about 300 m to the northeast when compared to the approximate mapping of Bartow (1984). On the northeast side of the fault, resistivity tends to be slightly lower within the lower layers below 150 m elevation (figs. 3 and 4). Additional mapped faults also show general lateral interruptions in the resistivity layering, and similar resistivity interruptions in other locations may be indicative of buried, unmapped faults.

In the southern part of the survey area, the conductivity in the upper portion of the lower resistivity dipping layer (100–120 m in elevation) is somewhat elevated (5–6 Ω•m) in comparison to other parts of the immediate area (fig. 4*E* and 4*F*). Mapped historical produced water disposal ponds are located near and upgradient of this area (fig. 1), and the elevated conductivity could be indicative of perched water or elevated salt concentrations in the vadose zone; however, borehole geophysical logs from nearby oil and gas wells suggest this relatively conductive layer is likely to be associated with a lithologic layer with elevated clay content. Two borehole resistivity logs collected in 1939 and 1964 also show this conductive layer (well number 0293780 and 0293786; fig. 4*F*), indicating that this layer has been present and similar in resistivity for decades. About 5 km east of the survey area, more recent borehole geophysical logs collected in 2014 show layers with similar resistivity values and depths correlated to elevated gamma response consistent with high clay content (well number 03053410; CALGEM, 2020). Another relatively conductive isolated feature is found near and below the approximated water table elevation in the westernmost 500 m of the northernmost flight line (fig. 7). This feature approaches 4–5 Ω•m in value, lower in resistivity than typically seen in other parts of the survey area. This location could have elevated salinity that is unsampled by wells or be representative of clay-rich deposit, but it could also be the result of AEM data impacted by unrecognized infrastructure.

Overall, the absence of larger strongly conductive regions indicates that saline fluids exceeding 10,000 mg/L are unlikely to occur in the upper 300–400 m of sediments within the AEM survey area. Although no historical observations approach this salinity threshold in the immediate area that can be used to assess the bulk resistivity values associated with higher groundwater salinity levels in this geologic

Figure 6. Driller's log 27S26E34A plotted with binary clay content classifications. Blue indicates clay bearing layer, and tan indicates a layer without clay, the same color scheme used in driller's logs in fig. 4. This driller's log is plotted on line L501501 in figure 4*D*.

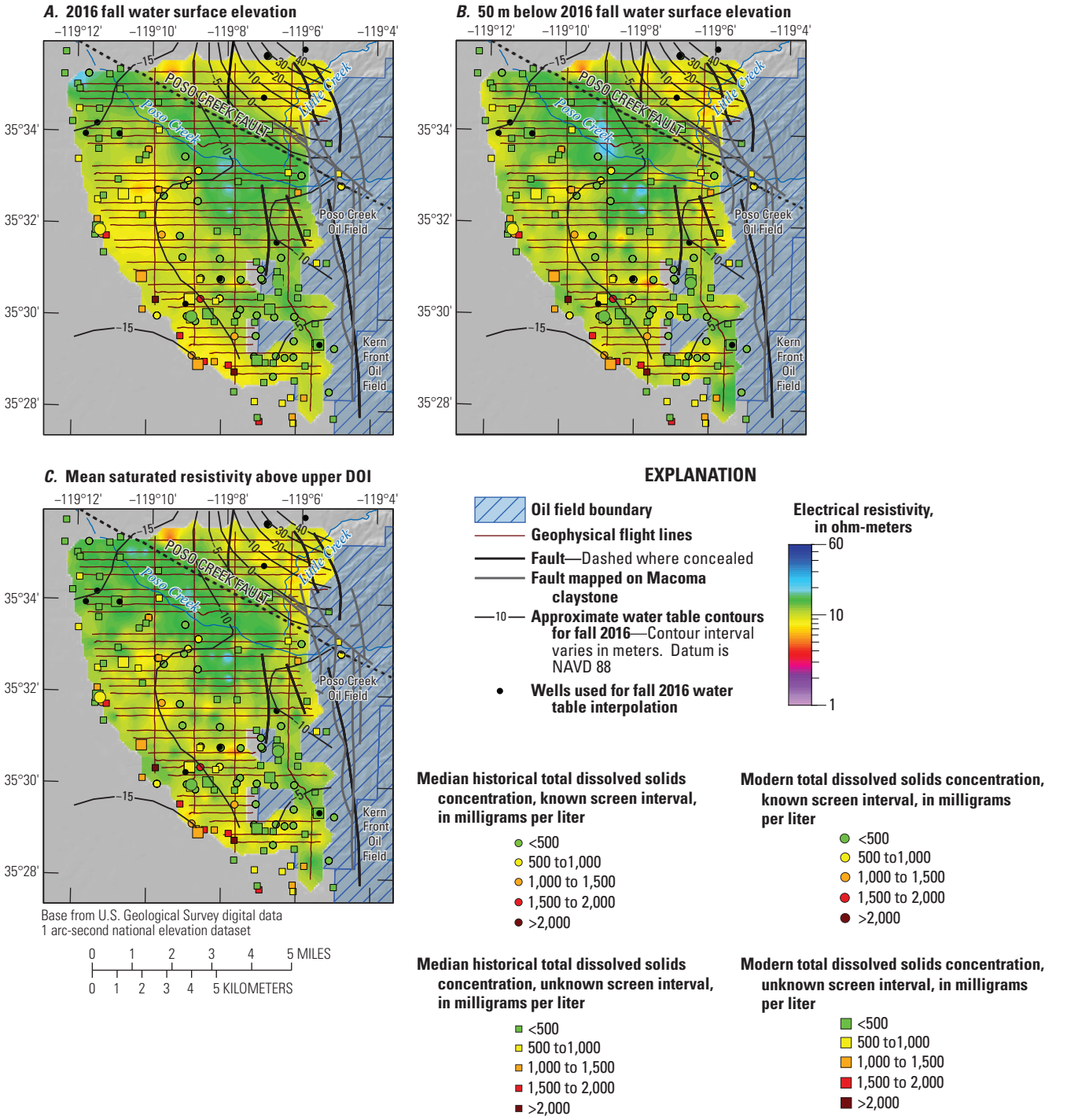

Figure 7. Airborne electromagnetic-derived resistivity. *A*, Resistivity taken at the approximated fall 2016 water table elevation (grey contours) *B*, resistivity taken 50 m below the water table elevation, and *C*, mean resistivity of the saturated zone above the upper DOI limit compared to historical total dissolved solids concentrations. Total dissolved solids data (Metzger and others, 2018 and California State Water Resources Control Board, 2020) are shown for recent (large symbols, 2006–20) and historical median (small symbols, 1930–2005) measurements. Total dissolved solids samples for wells with reported well construction where the screen interval overlaps with the saturated portion of the airborne electromagnetic depth of investigation (circles) and where construction is not known (squares).

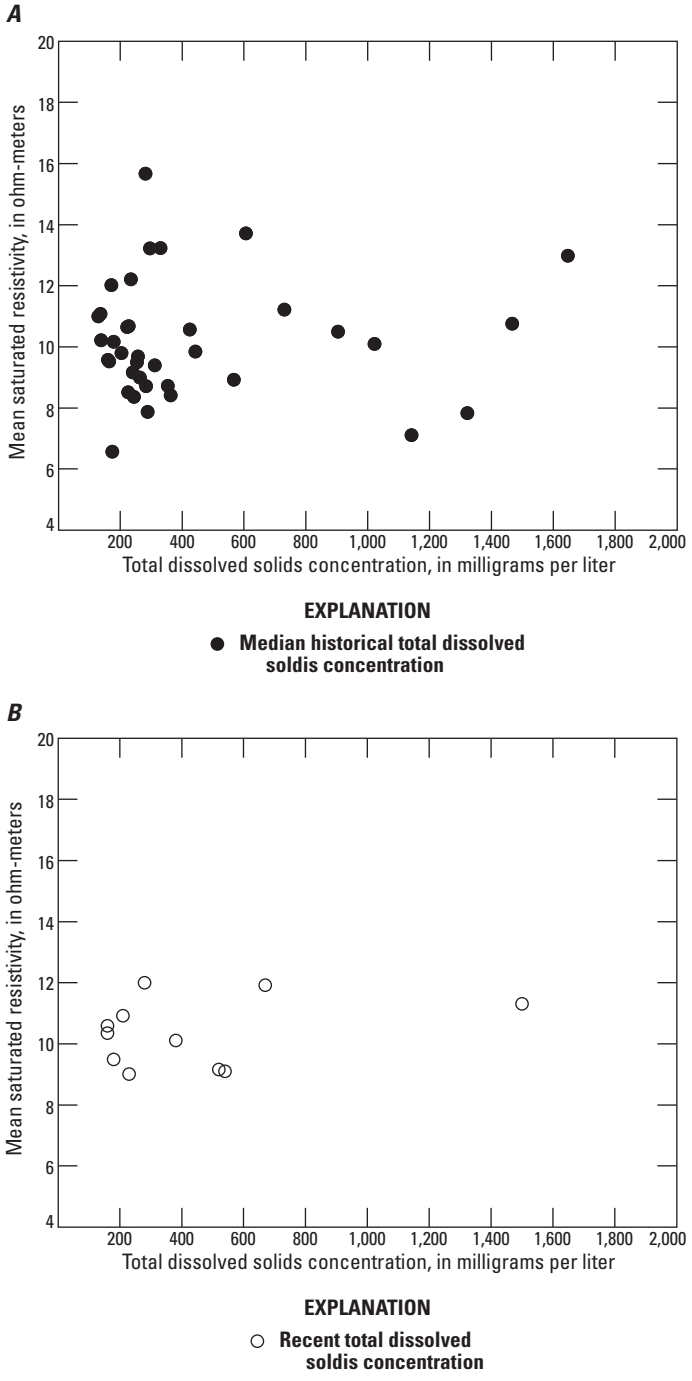

Figure 8. Correlation between mean bulk resistivity of the saturated zone above the upper depth of investigation limit and *A*, median historical total dissolved solids concentrations for wells with screens that overlap the depth of investigation interval and *B*, recent total dissolved solids concentrations between 2006–20 where well construction is unknown.

setting, comparisons from other studies can lend some context. High salinity groundwater more than 10,000 mg/L typically drives resistivity below the values commonly associated with fine-grained lithology or clay-rich sediments in other parts of the region. On the west side of the San Joaquin Valley, AEM-derived bulk resistivity was typically found to be less than 2 Ω•m for areas where groundwater exceeded 10,000 mg/L, whereas resistivity values less than 4 Ω•m were rarely observed where TDS concentrations were less than 3,000 mg/L regardless of lithologic texture or clay content (Ball and others, 2020). Resistivity values do not fall below the 2 Ω•m threshold within the Poso Creek survey area, and no substantial areas fall below the 4 Ω•m threshold. The substantial differences in geologic setting between the western and eastern margins of the San Joaquin Valley may limit the applicability of the salinity-resistivity relations developed for the west. Borehole geophysical log analyses by Stephens and others (2021) for the Poso Creek oil field found a threshold bulk resistivity of 2 Ω•m in clean (water saturated and clay free) sands associated with TDS > 10,000 mg/L in the Kern River Formation and Etchegoin Formations. Though we cannot independently evaluate clay content throughout the AEM survey, the lack of relatively low bulk resistivity locally associated with this salinity threshold further supports that groundwater salinity above the AEM DOI is unlikely to exceed 10,000 mg/L in the Poso Creek area.

Summary

An airborne electromagnetic (AEM) survey was conducted in fall 2016 of the area adjacent to the Poso Creek oil field along the eastern margin of the San Joaquin Valley of California. Inverted resistivity models developed from the AEM data reveal a layered, west-dipping resistivity structure that corresponds most closely to the geologic trends of the area. The models indicate a relatively high-resistivity wedge-shaped layer extending from the surface, that transitions to lower resistivity layers likely indicative of finer-grained, higher clay content materials at depth. Resistivity contrasts become more muted below the expected position of the water table, but lithologic controls on resistivity remain apparent. Groundwater salinity in the region is relatively low in the historical record, with total dissolved solids concentrations typically below 1,000 milligrams per liter (mg/L) and commonly below 500 mg/L. With this expected salinity range, variations in aquifer lithology have a stronger apparent influence on AEM-derived resistivity than variations in salinity, and mapping salinity variations within this narrow range is difficult without directly addressing aquifer lithology. However, the absence of strongly conductive regions in the AEM results suggests that areas of elevated salinity, particularly above the 10,000 mg/L threshold, are unlikely to occur in the upper 300 to 400 meters (m) of the survey area.

The USGS California Oil Gas and Groundwater program has several broad objectives including locating aquifers containing fresh and brackish groundwater near oil and gas fields and improving our understanding of the hydrologic connectivity between oil and gas activities and groundwater resources. The Poso Creek AEM results show little evidence for saline groundwater within the study area, and resistivity values are consistent with sediments containing relatively fresh groundwater. Correlations between AEM-derived resistivity and historical salinity data, driller's descriptions, and water table measurements demonstrate the strongest sensitivity to lithologic texture, with likely secondary influences from saturation and salinity variations. The resistivity structure therefore provides geologic context that may assist in the interpretation of groundwater quality sampling results by providing high-resolution information about lithologic variability and by defining faults and structural trends that may influence hydrogeologic connectivity between wells and the Poso Creek oil field upgradient of the AEM survey area.

References Cited

Archie, G.E., 1942, The electrical resistivity log as an aid in determining some reservoir characteristics: Transactions of the AIME, v. 146, no. 1, p. 54–62. [Also available at https://doi.org/10.2118/942054-G.]

Auken, E., Christiansen, A.V., Kirkegaard, C., Fiandaca, G., Schamper, C., Behroozmand, A.A., Binley, A., Nielsen, E., Efferso, F., Christensen, N.B., Sorenson, K., Foged, N., and Vignoli, G., 2015, An overview of a highly versatile forward and stable inverse algorithm for airborne, ground-based and borehole electromagnetic and electric data: Exploration Geophysics, v. 46, no. 3, p. 223–235. [Also available at https://doi.org/10.1071/EG13097.]

Aarhus Geosoftware, 2019, Aarhus Workbench, version 6.0.1: Aarhus Geosoftware software release, accessed March 14, 2022, at https://www.aarhusgeosoftware.dk/.

Ball, L. B., 2020, Airborne electromagnetic and magnetic survey data, San Joaquin Valley near Lost Hills, California, October 2016: U.S. Geological Survey data release, accessed March 14, 2022, at https://doi.org/10.5066/F7G44PKR.

Ball, L.B., Davis, T.A., Minsley, B.J., Gillespie, J.M., and Landon, M.K., 2020, Probabilistic categorical groundwater salinity mapping from airborne electromagnetic data adjacent to California's Lost Hills and Belridge oil fields: Water Resources Research, v. 56, no. 6, 20 p. [Also available at https://doi.org/10.1029/2019WR026273.]

Bartow, J.A., 1984, Geologic map and cross sections of the southeastern margin of the San Joaquin Valley, California: U.S. Geological Survey Miscellaneous Investigations Map I–1496, 1 sheet, scale 1:125,000.

Bartow, J.A., 1991, The Cenozoic evolution of the San Joaquin Valley, California: U.S. Geological Survey Professional Paper 1501, 40 p., 2 pls. [Also available at https://doi.org/10.3133/pp1501.]

Bartow, J.A., and Pittman, G.M., 1983, The Kern River Formation, southeastern San Joaquin Valley, California: U.S. Geological Survey Bulletin 1529–D, 17 p., accessed March 14, 2022, at https://pubs.er.usgs.gov/publication/b1529D.

Beahm, C.L., 2015, Depositional environment of the basal Etchegoin Formation within the Poso Creek oil field, Kern County, California: California State University, Bakersfield thesis, accessed March 14, 2022, at https://scholarworks.calstate.edu/concern/theses/hq37vr58h.

California Department of Water Resources [CDWR], 2020, Well completion reports: California Department of Water Resources website, accessed March 14, 2022, at https://water.ca.gov/Programs/Groundwater-Management/Wells/Well-Completion-Reports.

California Geologic Energy Management Division [CALGEM], 2020, Well records search: California Department of Conservation website, accessed March 14, 2022, at https://filerequest.conservation.ca.gov/WellRecord.

California Oil, Gas, and Groundwater Program, 2020, California Oil, Gas, and Groundwater (COGG) program: California Water Science Center website, accessed March 14, 2022, at https://webapps.usgs.gov/cogg/.

California Senate, 2013, Oil and gas—Well Stimulation: California Senate Bill no. 4, chap. 313, 21 p., accessed March 14, 2022, at https://leginfo.legislature.ca.gov/faces/billNavClient.xhtml?bill_id=201320140SB4.

California State Water Resources Control Board, 1988, State water resources control board resolution no. 88–63 adoption of policy entitled "sources of drinking water": California State Water Resources Control Board resolution, 2 p., accessed February 24, 2022, at https://www.waterboards.ca.gov/board_decisions/adopted_orders/resolutions/1988/rs1988_0063.pdf.

California State Water Resources Control Board, 2015, Model criteria for groundwater monitoring in areas of oil and gas well stimulation: California State Water Resources Control Board, 31 p., accessed March 14, 2022, at https://www.waterboards.ca.gov/water_issues/programs/groundwater/sb4/docs/model_criteria_final_070715.pdf.

California State Water Resources Control Board, 2020, Groundwater ambient monitoring and assessment groundwater information system: California State Water Resources Control Board website, accessed March 14, 2022 at https://gamagroundwater.waterboards.ca.gov/gama/gamamap/public/.

Cawelo Groundwater Sustainability Agency, 2020, Cawelo groundwater sustainability agency, groundwater sustainability plan: Todd Groundwater, Alameda California, accessed March 14, 2022, at https://www.cawelowd.org/wp-content/uploads/2020/03/cawelo_mngareaplan-gsp_complete_jan20_2020.pdf.

Central Valley Water Board, 2018, Produced wastewater ponds in the Central Valley: Central Valley Water Board website, accessed March 14, 2022, at https://www.waterboards.ca.gov/centralvalley/water_issues/oil_fields/information/disposal_ponds/.

Christiansen, A.V., and Auken, E., 2012, A global measure for depth of investigation: Geophysics, v. 77, no. 4, p. 171–177. [Also available at https://doi.org/10.1190/geo2011-0393.1.]

Christiansen, A.V., Foged, N., and Auken, E., 2014, A concept for calculating accumulated clay thickness from borehole lithological logs and resistivity models for nitrate vulnerability assessment: Journal of Applied Geophysics, v. 108, p. 69–77. [Also available at https://doi.org/10.1016/j.jappgeo.2014.06.010.]

Christiansen, A.V., Madsen, L.M., and Auken, E., 2019, Sensitivity functions of airborne EM systems over layered models: American Geophysical Union-Society of Economic Geologists Airborne Geophysics Workshop, Davie, Florida, accessed January 1, 2020, at https://agu.confex.com/agu/19workshop1/webprogram/Paper478800.html.

Coburn, M.G., and Gillespie, J.M., 2002, A hydrogeologic study to optimize steam flood performance in a giant oilfield—Kern River field, California: AAPG Bulletin, v. 86, no. 8, p. 1489–1505. [Also available at https://doi.org/10.1306/61EEDCD8-173E-11D7-8645000102C1865D.]

Croft, M.G., 1972, Subsurface geology of the Late Tertiary and Quaternary water-bearing deposits of the southern part of the San Joaquin Valley, California: U.S. Geological Survey Water-Supply Paper 1999–H, 29 p., 6 pls. [Also available at https://doi.org/10.3133/wsp1999H.]

Davis, T.A., Bennett, G.L., Metzger, L.F., Kjos, A.R., Peterson, M.F., Johnson, J., Johnson, T.D., Brilmyer, C.A., and Dillon, D.B., 2018a, Data analyzed for the preliminary prioritization of California oil and gas fields for regional groundwater monitoring: U.S. Geological Survey data release, accessed March 14, 2022, at https://doi.org/10.5066/F7FJ2DV3.

Davis, T.A., Landon, M.K., and Bennett, G.L., 2018b, Prioritization of oil and gas fields for regional groundwater monitoring based on a preliminary assessment of petroleum resource development and proximity to California's groundwater resources: U.S. Geological Survey Scientific Investigations Report 2018–5065, 115 p. [Also available at https://doi.org/10.3133/sir20185065.]

Dieter, C.A., Maupin, M.A., Caldwell, R.R., Harris, M.A., Ivahnenko, T.I., Lovelace, J.K., Barber, N.L., and Linsey, K.S., 2018, Estimated use of water in the United States in 2015: U.S. Geological Survey Circular 1441, 65 p. [Also available at https://doi.org/10.3133/cir1441.]

Faunt, C.C., ed., 2009, v. 1766. Groundwater availability of the Central Valley Aquifer, California, U.S. Geological Survey Professional Paper, 227 p. [Also available at https://doi.org/10.3133/pp1766.]

Gillespie, J. M., Davis, T.A., Ball, L.B., Herrera, P.J., Wolpe, Z., Medrano, V., Bobbitt, M. and Stephens, M.J., 2019, Geological, geochemical, and geophysical data from the Lost Hills and Belridge oil fields: U.S. Geological Survey data release, accessed March 14, 2022, at https://doi.org/10.5066/p90qh6ci.

Gillespie, J.M., Kong, D., and Anderson, S.D., 2017, Groundwater salinity in the southern San Joaquin Valley: AAPG Bulletin, v. 101, no. 8, p. 1239–1261. [Also available at https://doi.org/10.1306/09021616043.]

Gunnink, J.L., and Siemon, B., 2015, Applying airborne electromagnetics in 3D stochastic geohydrological modelling for determining groundwater protection: Near Surface Geophysics, v. 13, no. 1, p. 45–60. [Also available at https://doi.org/10.3997/1873-0604.2014044.]

Jennings, C.W., Strand, R.G., Rogers, T.H., Boylan, R.T., Moar, R.R., and Switzer, R.A., 1977, Geologic map of California: California Division of Mines and Geology, 1 sheet, scale 1:750,000.

Keller, G.V., and Frischknecht, F.C., 1966, Electrical methods in geophysical prospecting: Oxford, Permagon Press, 526 p.

Kern County Department of Agriculture, 2016, Kern County 2016 annual permitted crop boundaries: Kern County Department of Agriculture website, accessed March 14, 2022, at http://www.kernag.com/gis/gis-data.asp.

Knight, R., Smith, R., Asch, T., Abraham, J., Cannia, J., Viezzoli, A., and Fogg, G., 2018, Mapping aquifer systems with airborne electromagnetics in the Central Valley of California: Ground Water, v. 56, no. 6, p. 893–908. [Also available at https://doi.org/10.1111/gwat.12656.]

Kodl, E.J., Eacmen, J.C., and Coburn, M.G., 1990, A geologic update of the emplacement mechanism within the Kern River Formation at the Kern River field—Structure: California, Stratigraphy and Hydrocarbon Occurrences of the San Joaquin Basin.

McMahon, P.B., Kulongoski, J.T., Vengosh, A., Cozzarelli, I.M., Landon, M.K., Kharaka, Y.K., Gillespie, J.M., and Davis, T.A., 2018, Regional patterns in the geochemistry of oil-field water, southern San Joaquin Valley, California, USA: Applied Geochemistry, v. 98, p. 127–140. [Also available at https://doi.org/10.1016/j.apgeochem.2018.09.015.]

Metzger, L.F., Davis, T.A., Peterson, M.F., Brilmyer, C.A., and Johnson, J.C., 2018, Water and petroleum well data used for preliminary regional groundwater salinity mapping near selected oil fields in central and southern California: U.S. Geological Survey data release, accessed March 14, 2022, at https://doi.org/10.5066/F7RN373C.

Metzger, L.F., and Landon, M.K., 2018, Preliminary groundwater salinity mapping near selected oil fields using historical water-sample data, Central and Southern California: U.S. Geological Survey Scientific Investigations Report 2018–5082, 54 p., accessed March 14, 2022, at https://pubs.er.usgs.gov/publication/sir20185082.

Negrini, R., Baron, D., Gillespie, J., Horton, R., Draucker, A., Durham, N., Huff, J., Philley, P., Register, C., Parker, J., and Haslebacher, T., 2009, A Middle Pleistocene lacustrine delta in the Kern River depositional system—Structural control, regional stratigraphic context, and impact on groundwater quality: Contributions to the Geology of the San Joaquin Basin, California, Pacific Section American Association of Petroleum Geologists Publication MP48, p. 95–111.

Page, R.W., 1986, Geology of the fresh ground-water basin of the Central Valley, California with texture maps and sections: U.S. Geological Survey Professional Paper 1401–C, p. 1–54, 5 pls. [Also available at https://doi.org/10.3133/pp1401C.]

Sorensen, K., and Auken, E., 2004, SkyTEM—A new high-resolution helicopter transient electromagnetic system: Exploration Geophysics, v. 35, no. 3, p. 194–202. [Also available at https://doi.org/10.1071/EG04194.]

Stephens, M.J., Haugen, E.A., Shimabukuro, D.H., Gillespie, J.M., Sowers, T.A., Ducart, A., and Medrano, V., 2018, Geochemical, geological, and geophysical data for wells in the Poso Creek oil and gas field, Kern County, California: U.S. Geological Survey data release, accessed March 14, 2022, at https://doi.org/10.5066/P9RR9UYN.

Stephens, M.J., Shimabukuro, D.H., Chang, W., Gillespie, J.M., and Levinson, Z., 2021, Stratigraphic and structural controls on groundwater salinity variations in the Poso Creek Oil Field, Kern County, California, USA: Hydrogeology Journal, v. 29, no. 8, p. 2803–2820. [Also available at https://doi.org/10.1007/s10040-021-02381-5.]

Turesson, A., 2006, Water content and porosity estimated from ground-penetrating radar and resistivity: Journal of Applied Geophysics, v. 58, no. 2, p. 99–111. [Also available at https://doi.org/10.1016/j.jappgeo.2005.04.004.]

U.S. Census Bureau, 2018, 2018 National and State population estimates: U.S. Census Bureau website accessed July 29, 2019, at https://www.census.gov/newsroom/press-kits/2018/pop-estimates-national-state.html.

U.S. Department of Agriculture Economic Research Service, 2010, Agricultural productivity in the United States: U.S. Department of Agriculture Economic Research Service data set, accessed July 29, 2019 at https://www.ers.usda.gov/data-products/agricultural-productivity-in-the-us.

U.S. Energy Information Administration, 2017, Crude oil production: Energy Information Administration website, accessed July 29, 2019 at https://www.eia.gov/dnav/pet/pet_crd_crpdn_adc_mbbl_a.htm.

U.S. Drought Monitor, 2021, Kern County, California percent area in U.S. drought monitor categories: U.S. Drought Monitor website accessed March 14, 2022, at https://droughtmonitor.unl.edu/DmData/TimeSeries.aspx.

Viezzoli, A., Christiansen, A.V., Auken, E., and Sørensen, K., 2008, Quasi-3D modeling of airborne TEM data by spatially constrained inversion: Geophysics, v. 73, no. 3, p. 105–113. [Also available at https://doi.org/10.1190/1.2895521.]

Weddle, J., 1959, Premier and Enas areas of Poso Creek oil field—California oil fields summary of operations, forty-fifth annual report of the State Oil and Gas Supervisor: California Division of Oil and Gas, v. 45, no. 2, p. 41–50.

Welge, E.A., 1973, Poso Creek oil field, McVan area—California summary of operations, fifty-ninth annual report of the State Oil and Gas Supervisor: California Division of Oil and Gas, v. 59, no. 1, p. 59–68.

Zamudio, K.D., and Ball, L.B., 2022, Airborne electromagnetic and magnetic survey data, southeastern San Joaquin Valley near Cawelo, California, 2016: U.S. Geological Survey data release, https://www.sciencebase.gov/catalog/item/5d642e32e4b01d82ce987143.

Appendix 1. Modeled Resistivity Profiles for Airborne Electromagnetic Flight Lines

This section shows modeled resistivity profiles for each airborne electromagnetic (AEM) flight line in figures 1.1*A*–*C*–1.35*A*–*C*. The bolded line in the shaded relief map in the upper corner of each figure depicts the flight line shown in cross section. The approximated fall 2016 water table elevation is shown for each AEM flight line. Lithologic logs are classified by presence of clay. Borehole resistivity logs are shown using the same color scale as airborne electromagnetic models. Profiles are plotted alongside a geologic map showing the surficial geology (bottom map, modified from Bartow, 1984) that has been centered on the flight path (solid line) with resistivity logs shown as triangles and lithologic logs shown as squares.

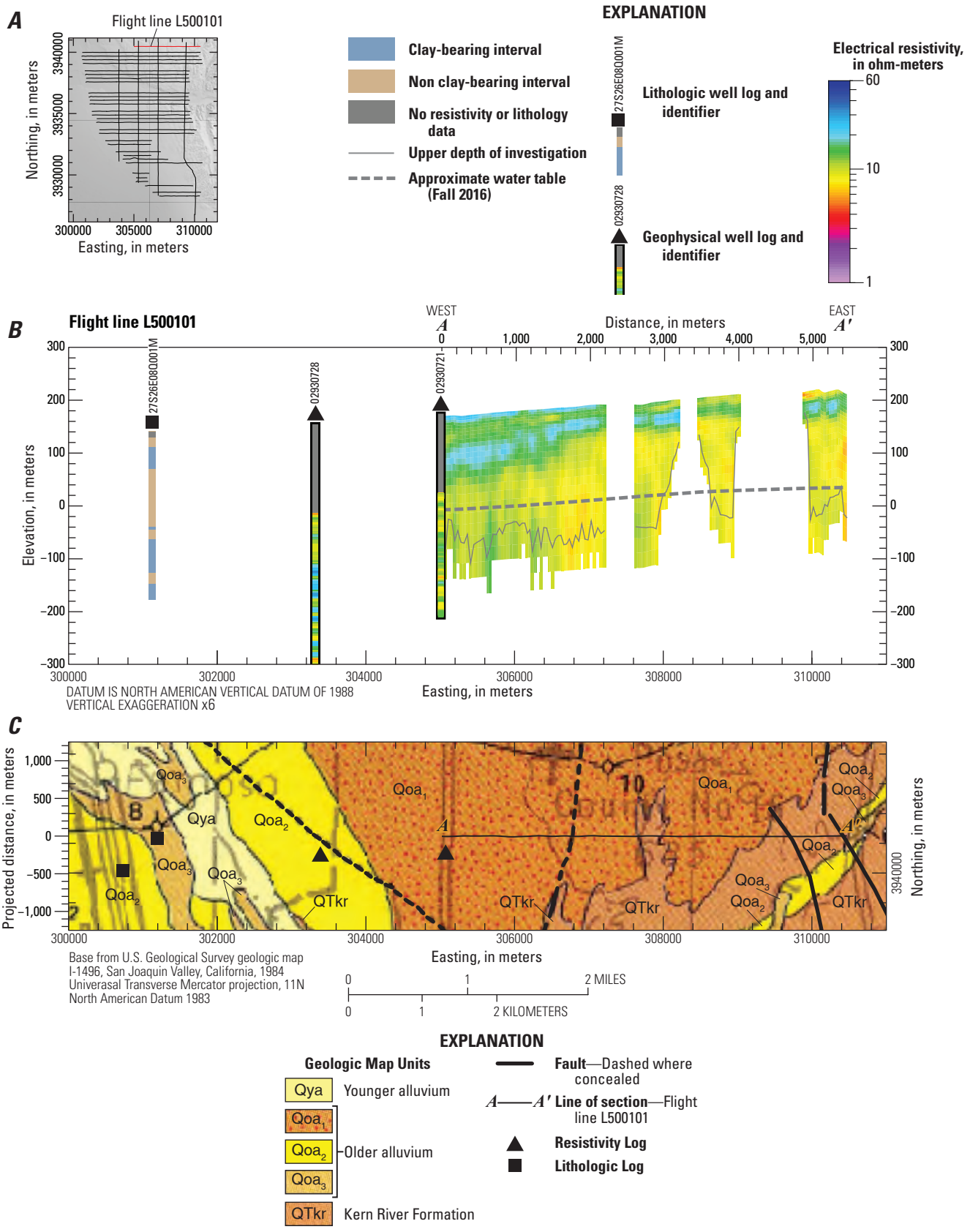

Figure 1.1. *A–C,* modeled resistivity profiles for airborne electromagnetic flight line L500101.

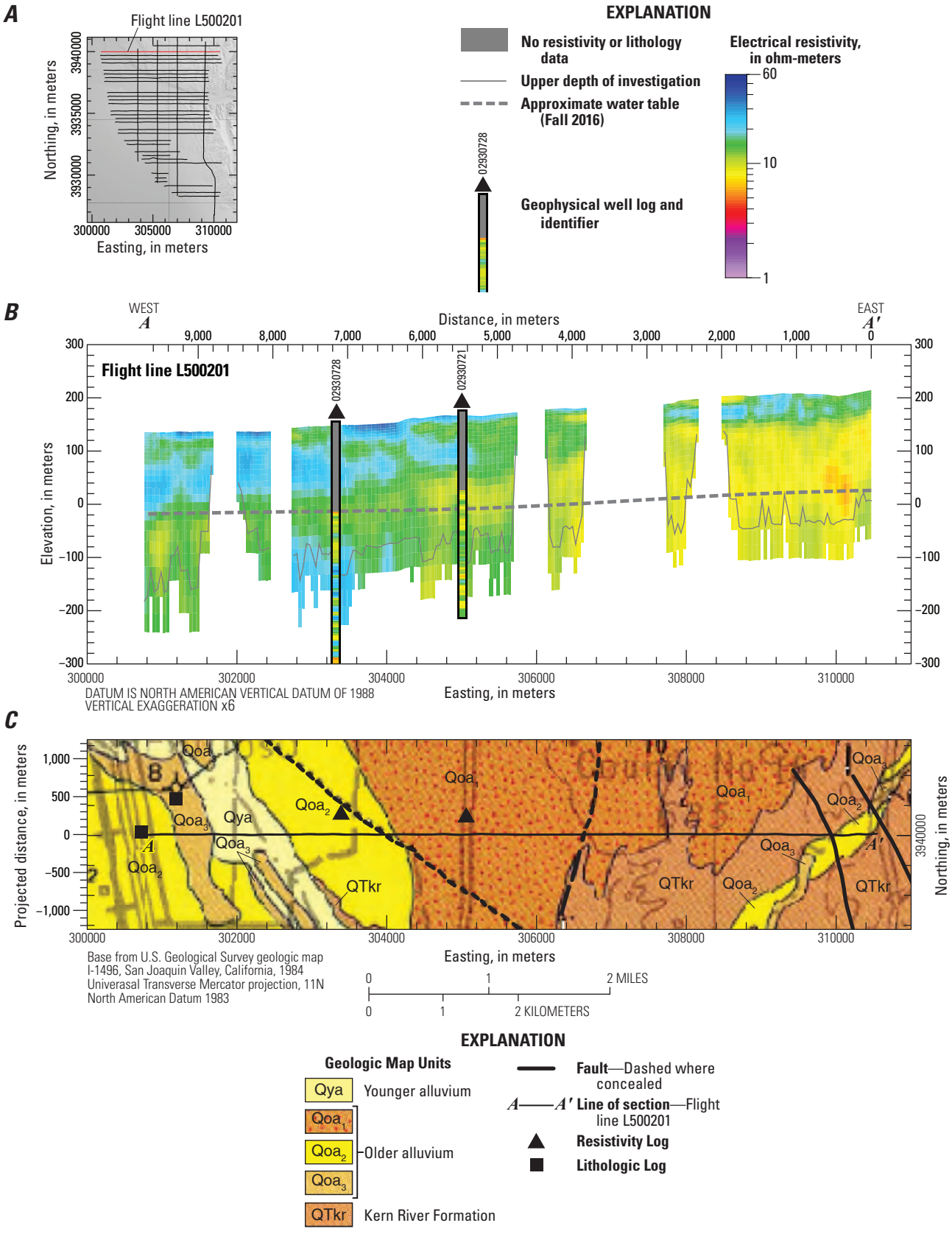

Figure 1.2. *A–C,* modeled resistivity profiles for airborne electromagnetic flight line L500201.

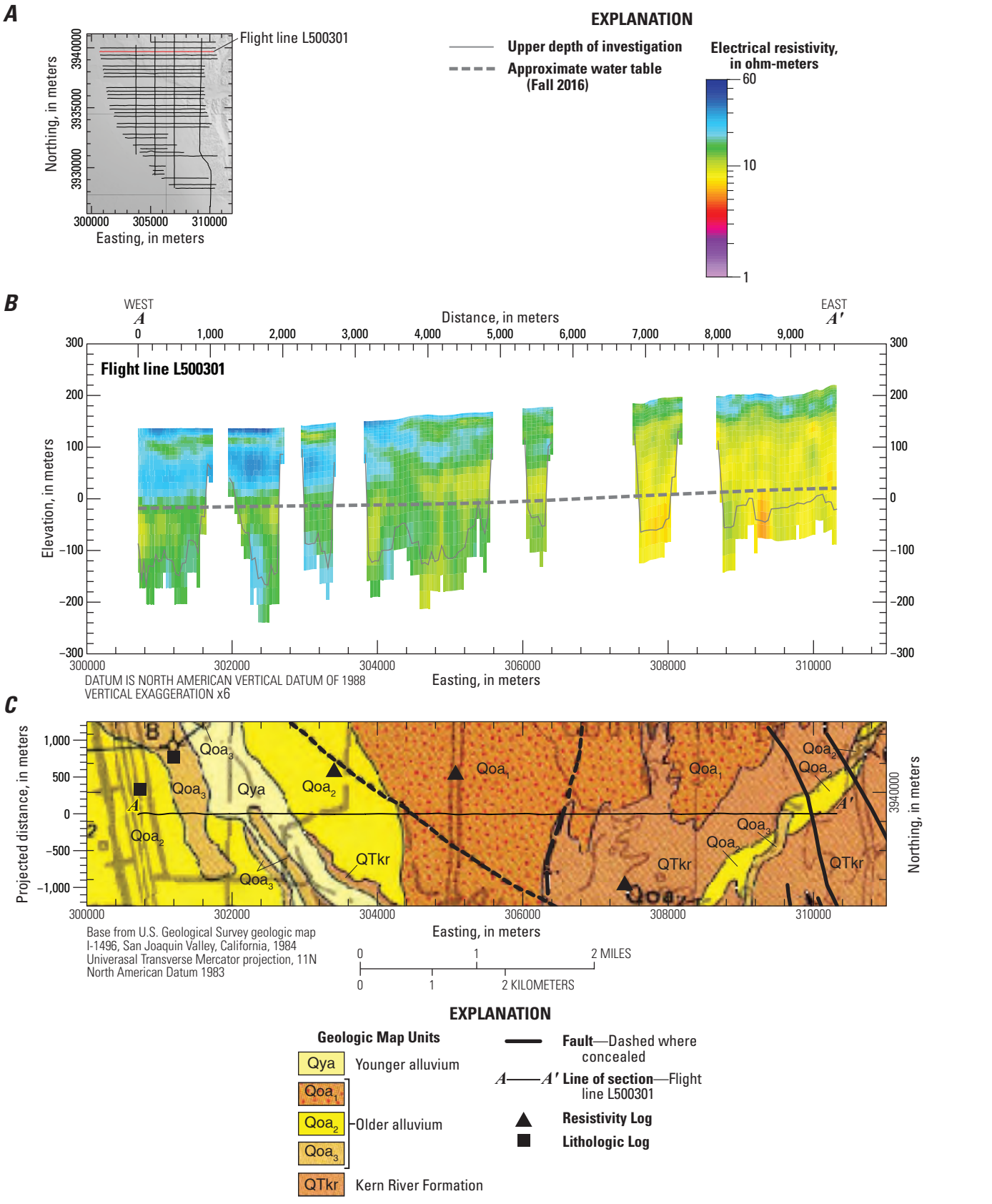

Figure 1.3. *A–C,* modeled resistivity profiles for airborne electromagnetic flight line L500301.

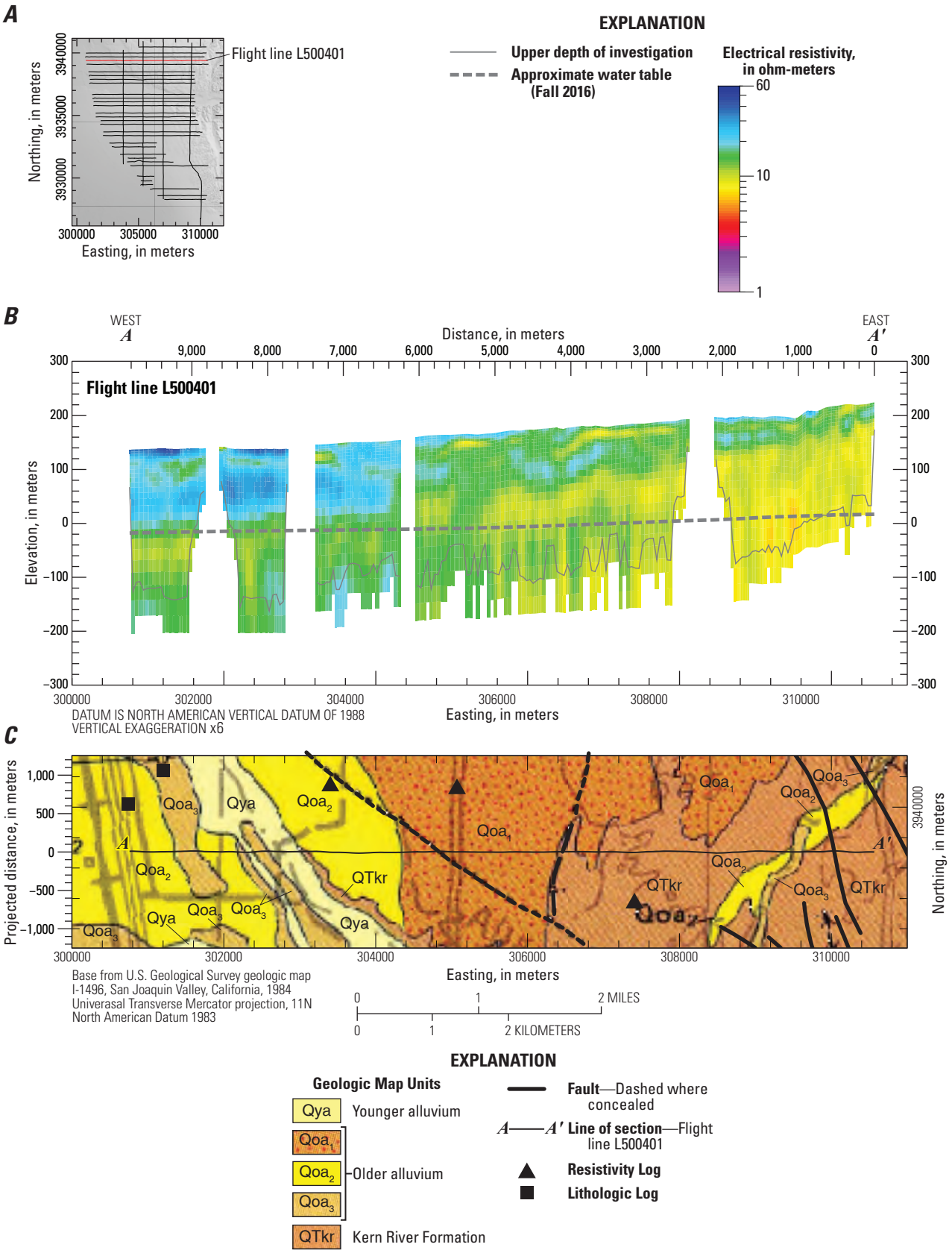

Figure 1.4. *A–C,* modeled resistivity profiles for airborne electromagnetic flight line L500401.

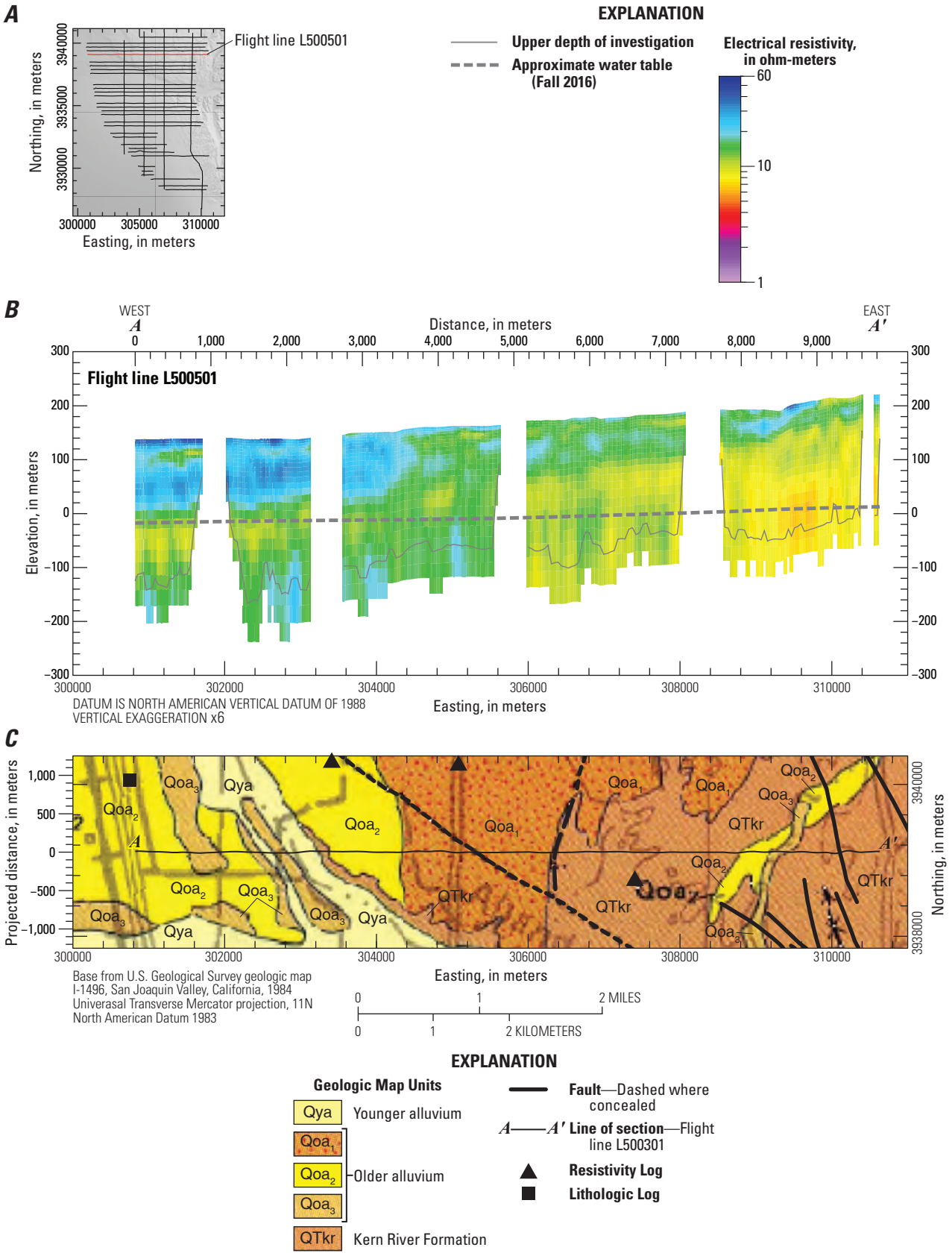

Figure 1.5. *A–C,* modeled resistivity profiles for airborne electromagnetic flight line L500501.

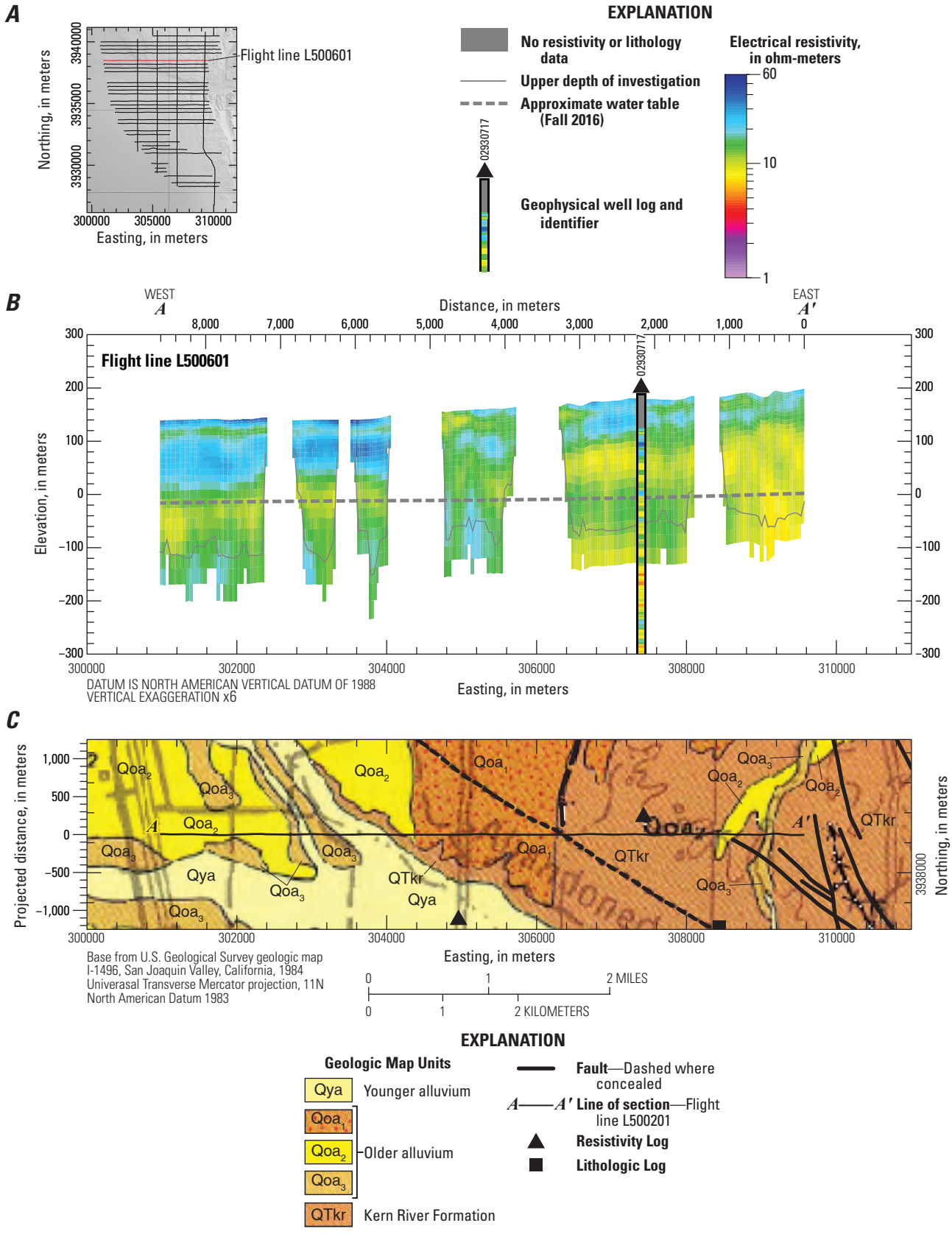

Figure 1.6. *A–C,* modeled resistivity profiles for airborne electromagnetic flight line L500601.

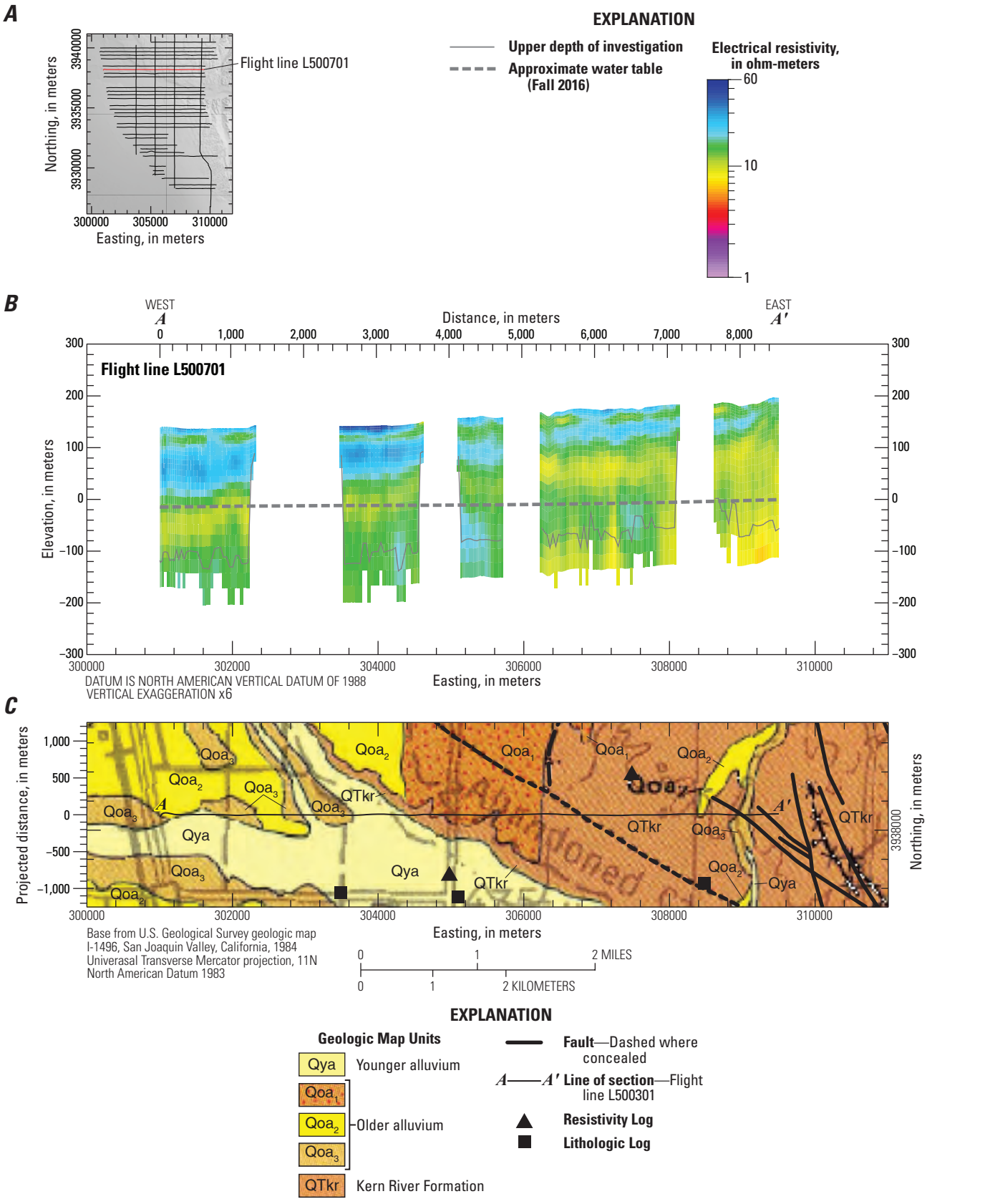

Figure 1.7. *A–C,* modeled resistivity profiles for airborne electromagnetic flight line L500701.

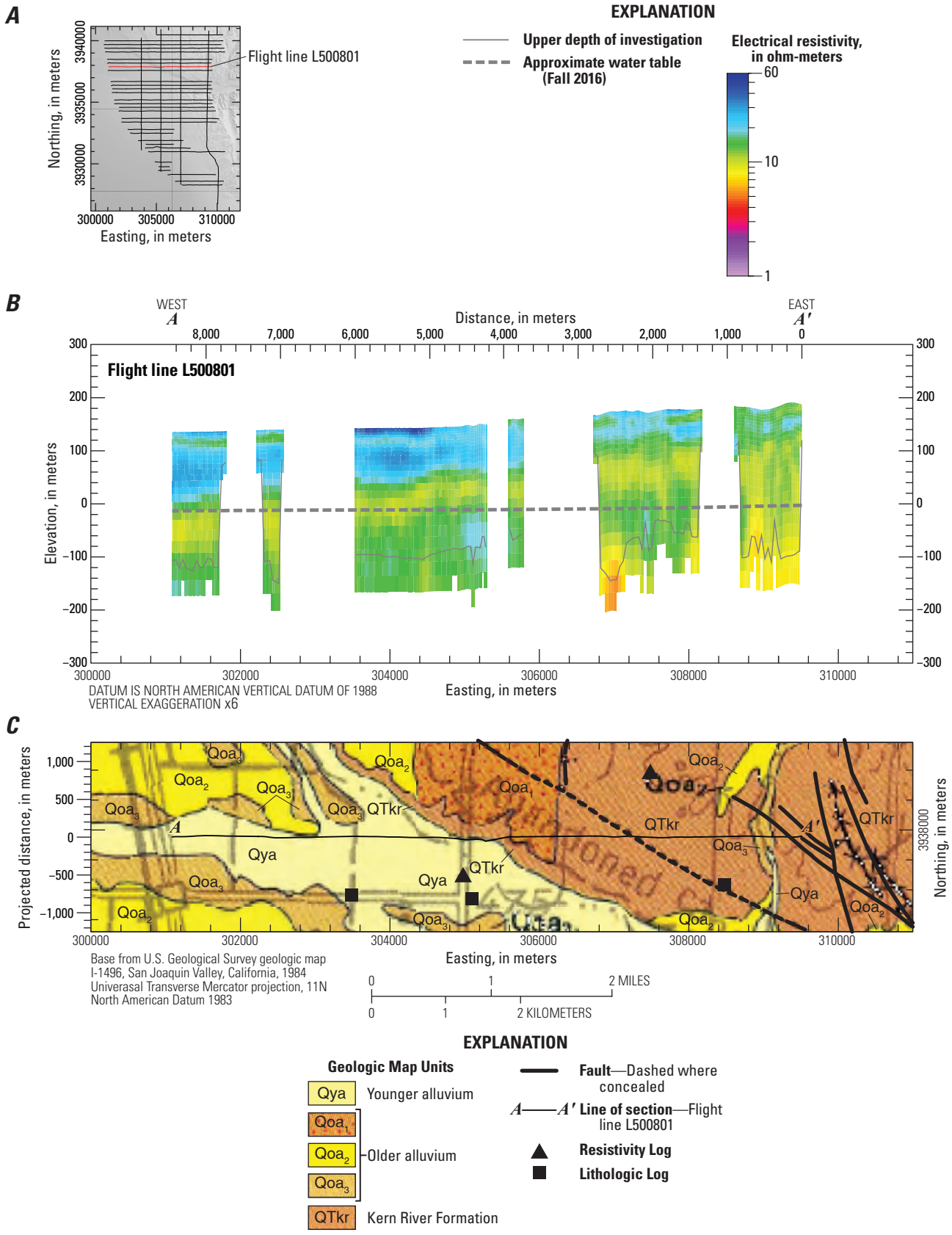

Figure 1.8. *A–C,* modeled resistivity profiles for airborne electromagnetic flight line L500801.

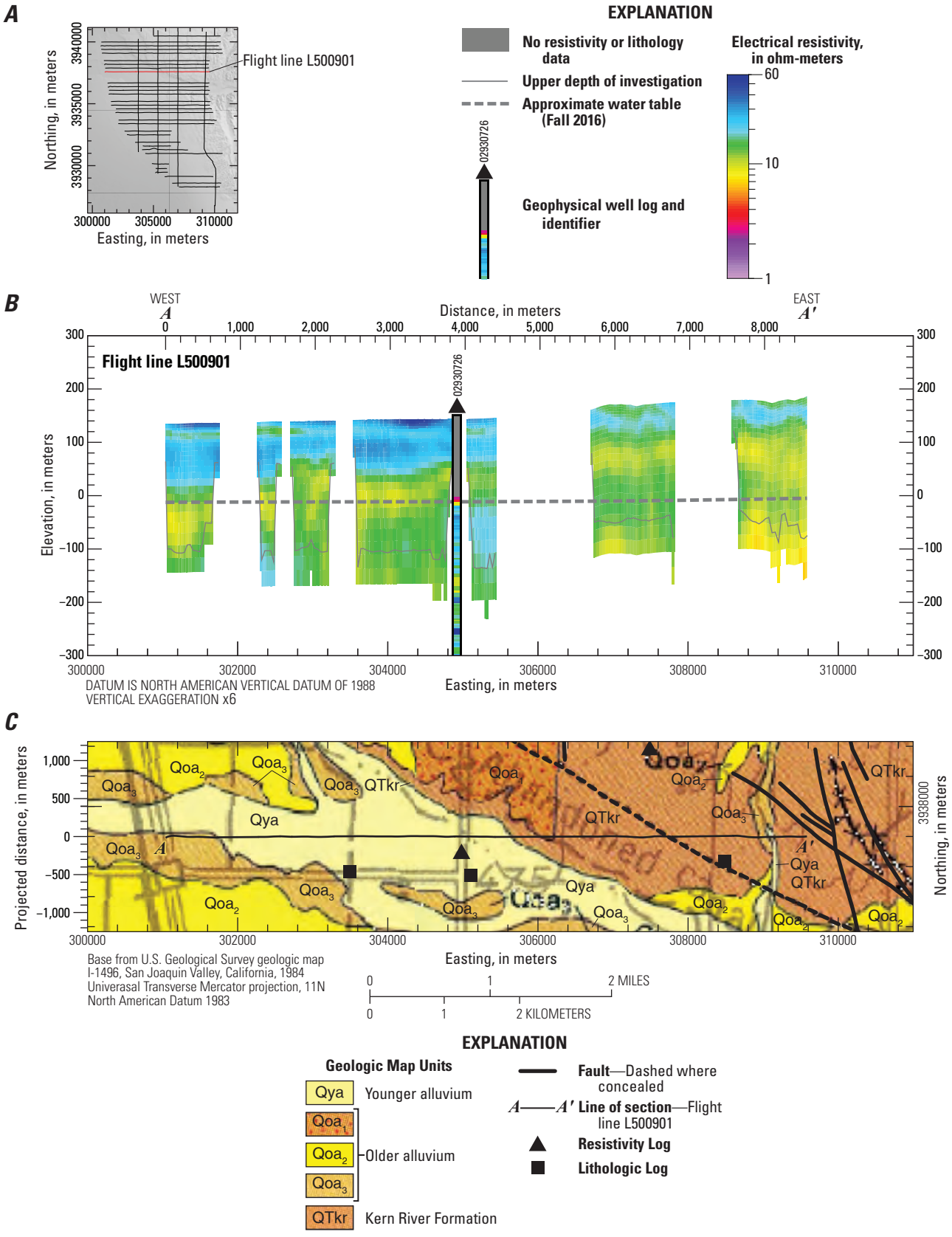

Figure 1.9. *A–C,* modeled resistivity profiles for airborne electromagnetic flight line L500901.

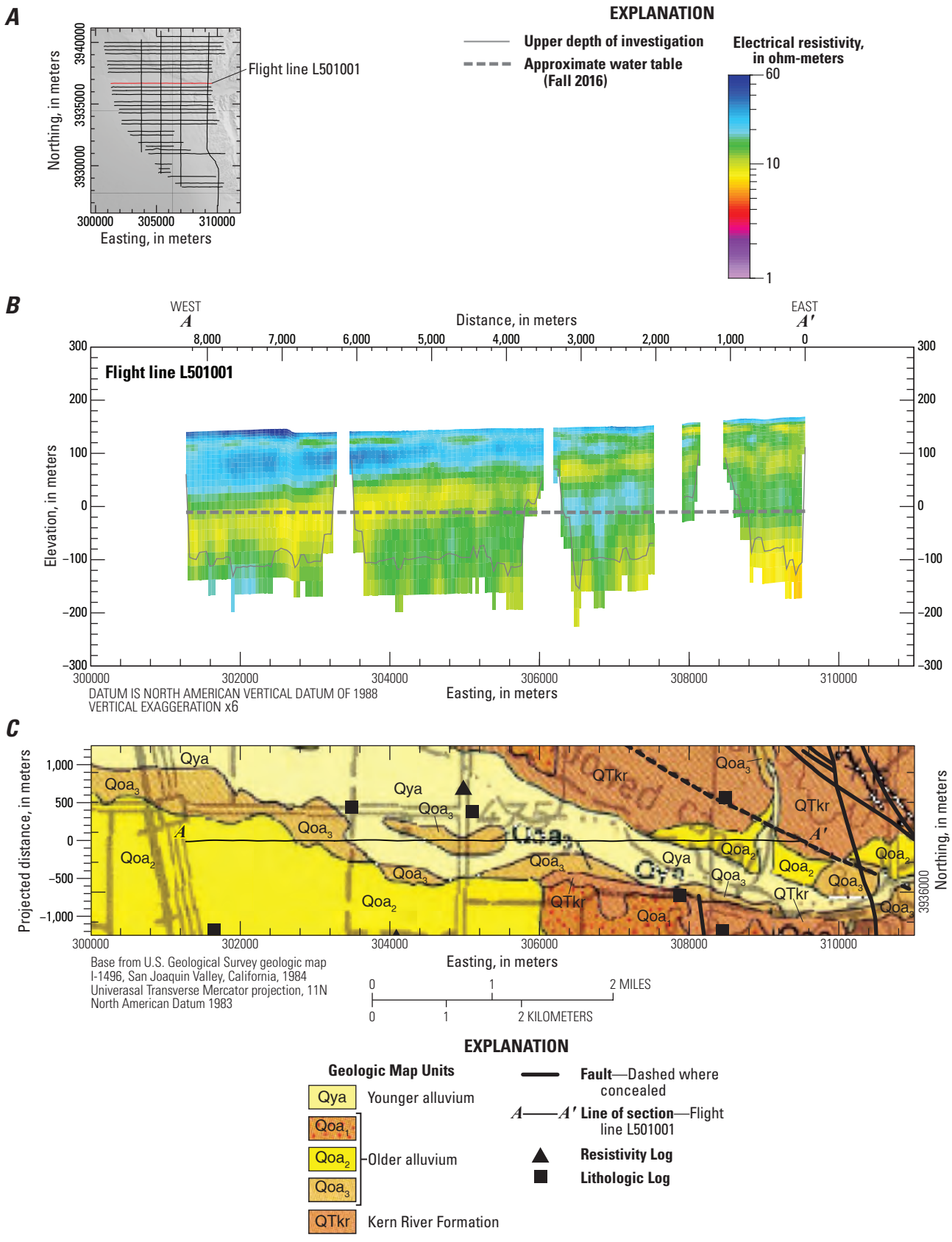

Figure 1.10. *A–C,* modeled resistivity profiles for airborne electromagnetic flight line L5001001.

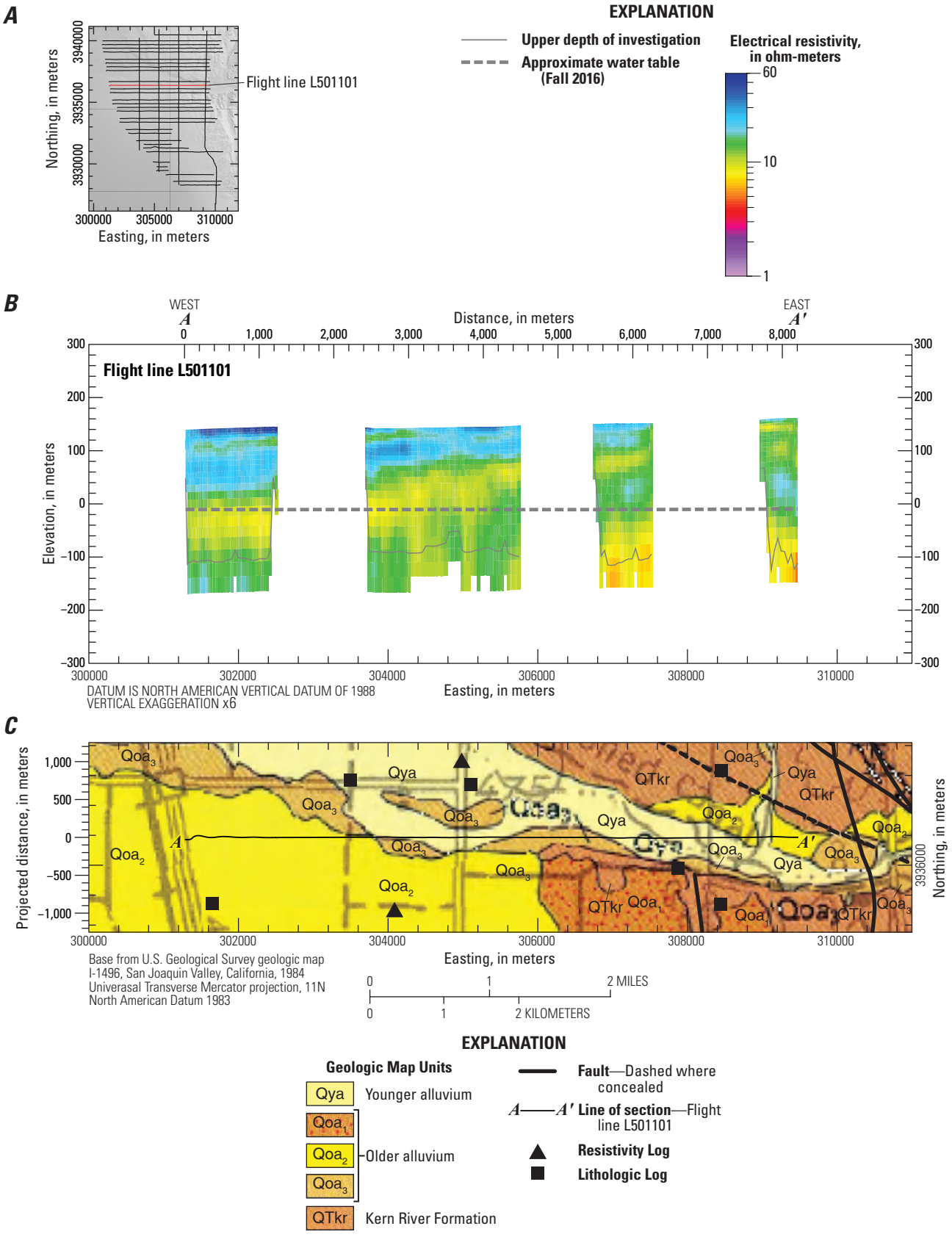

Figure 1.11. *A–C,* modeled resistivity profiles for airborne electromagnetic flight line L5001101.

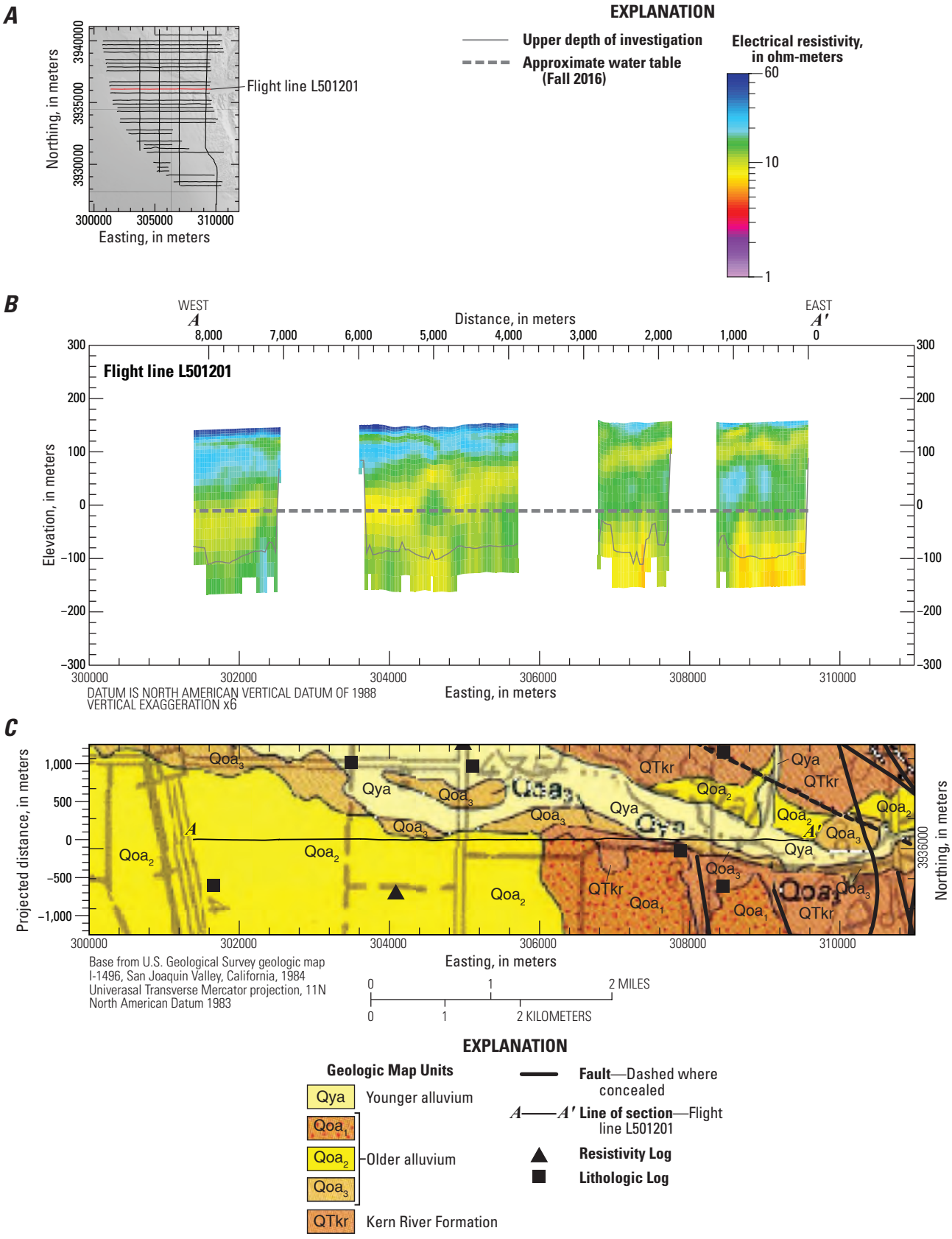

Figure 1.12. *A–C,* modeled resistivity profiles for airborne electromagnetic flight line L5001201.

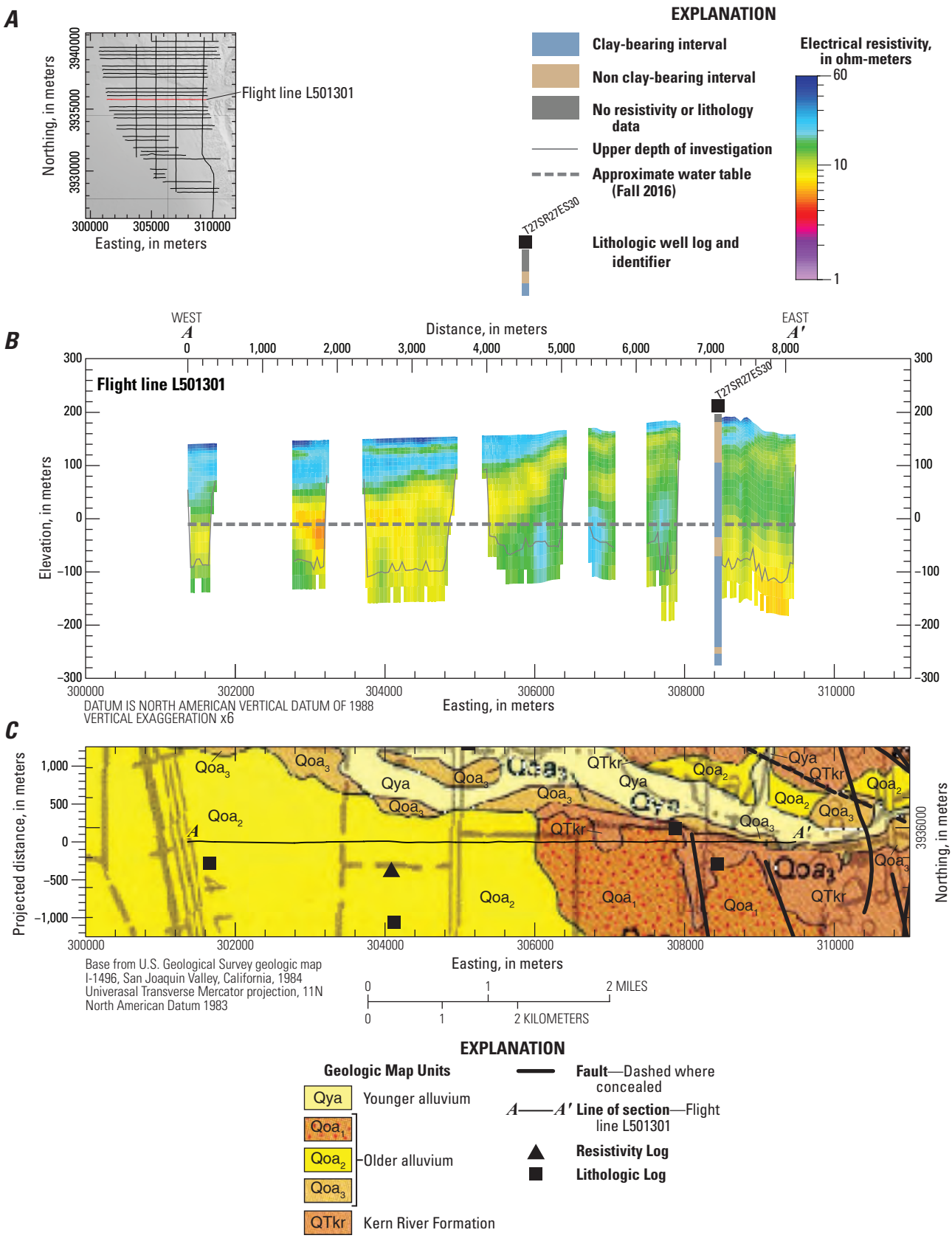

Figure 1.13. *A–C,* modeled resistivity profiles for airborne electromagnetic flight line L5001301.

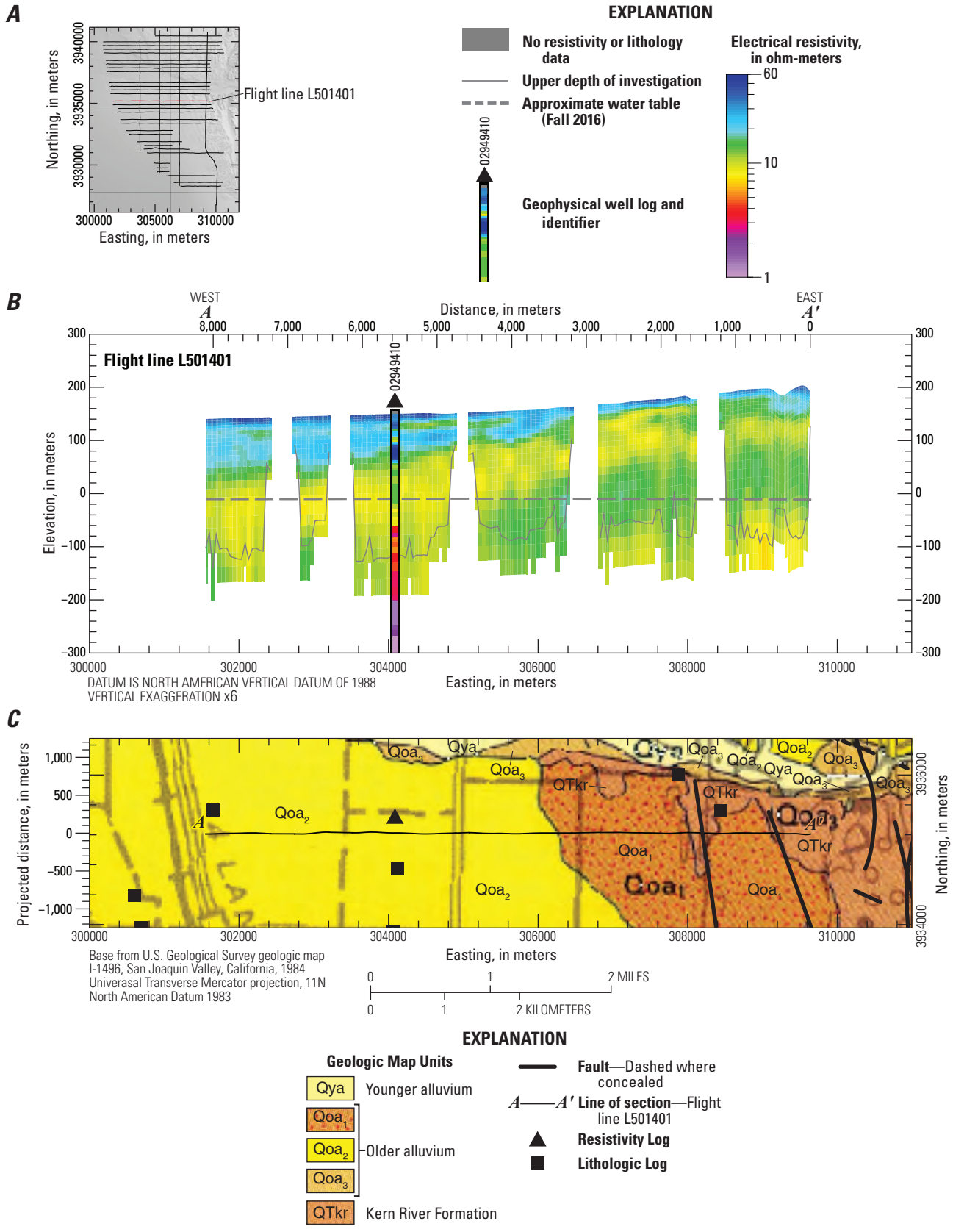

Figure 1.14. *A–C,* modeled resistivity profiles for airborne electromagnetic flight line L5001401.

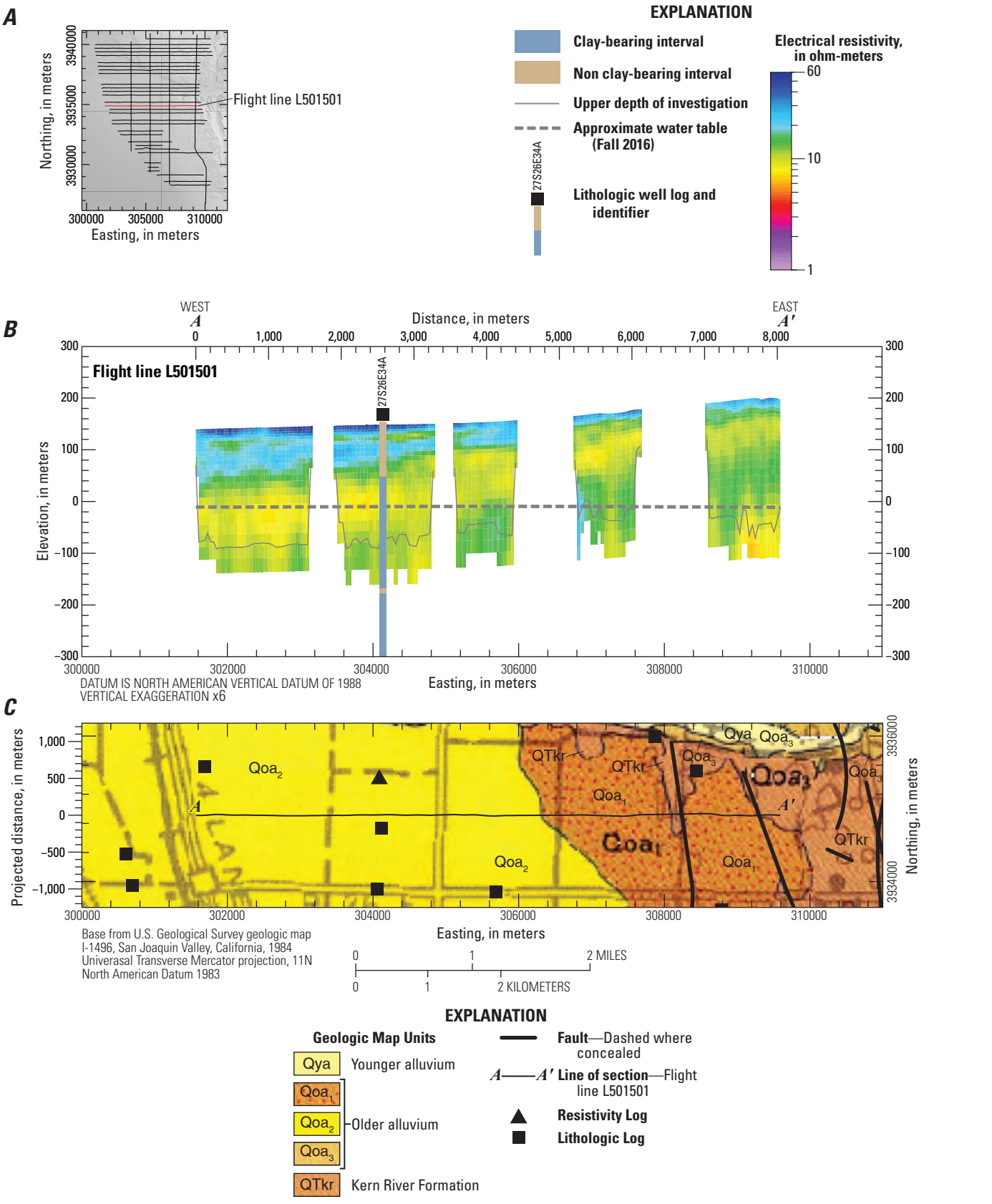

Figure 1.15. *A–C,* modeled resistivity profiles for airborne electromagnetic flight line L5001501.

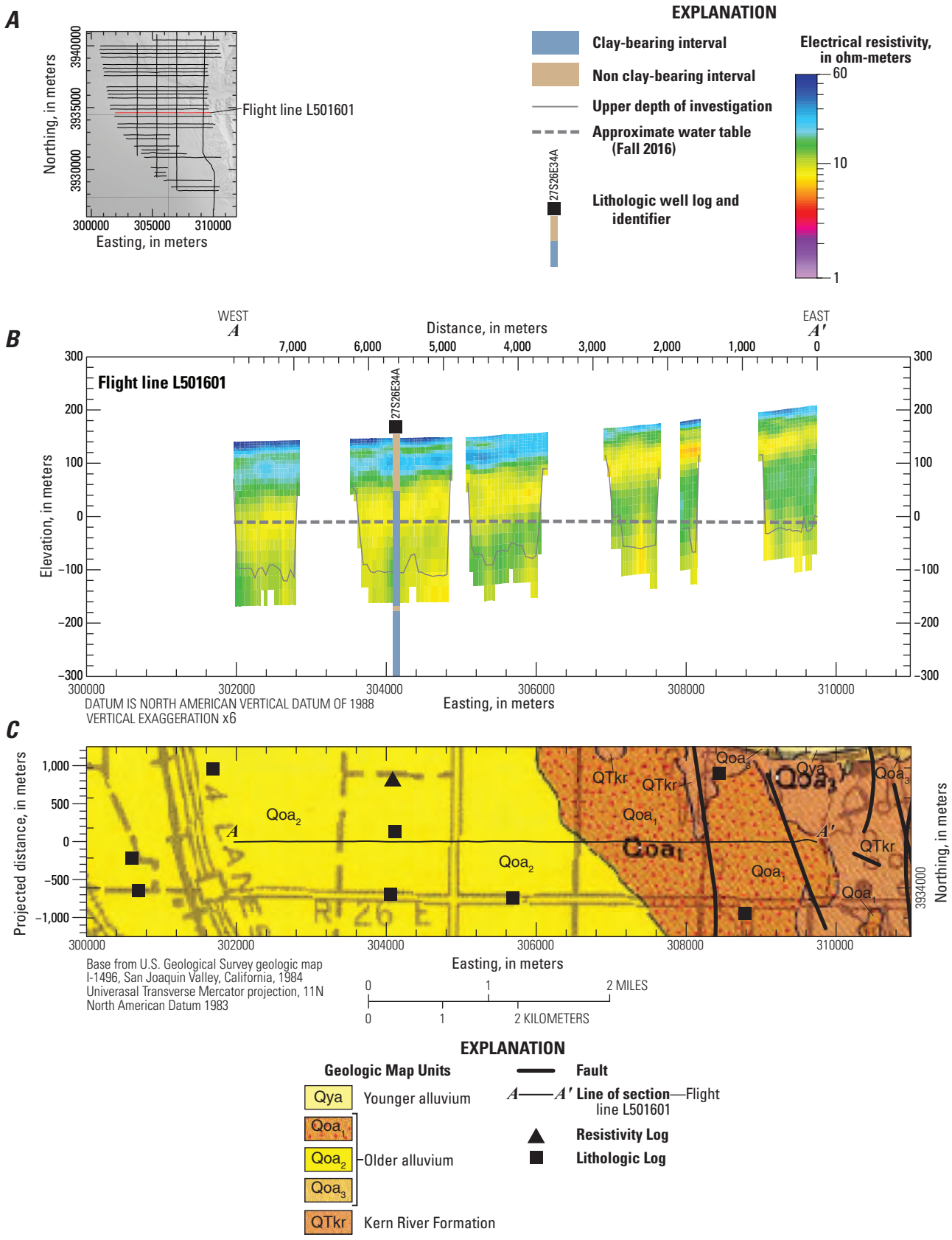

Figure 1.16. *A–C,* modeled resistivity profiles for airborne electromagnetic flight line L5001601.

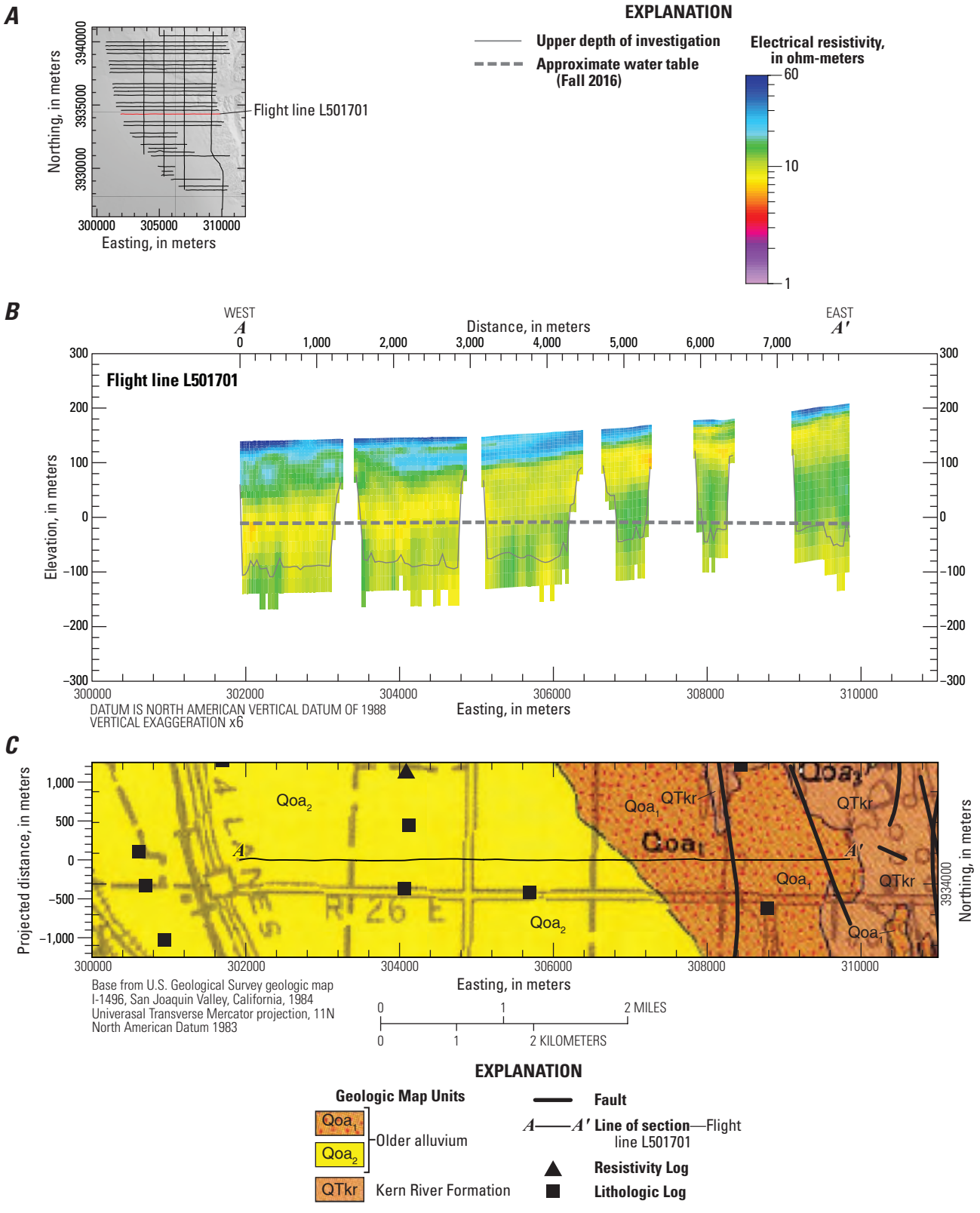

Figure 1.17. *A–C,* modeled resistivity profiles for airborne electromagnetic flight line L5001701.

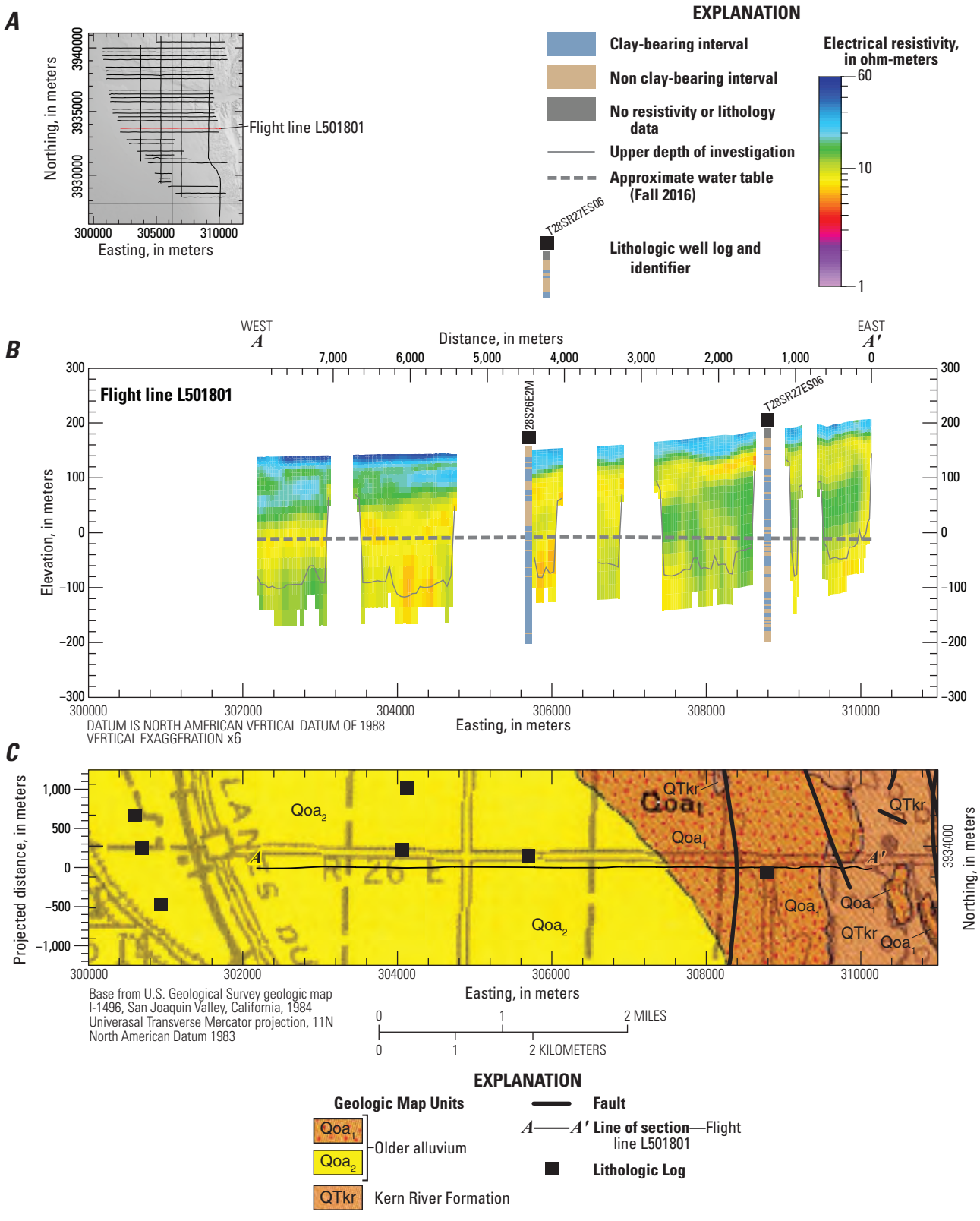

Figure 1.18. *A–C,* modeled resistivity profiles for airborne electromagnetic flight line L5001801.

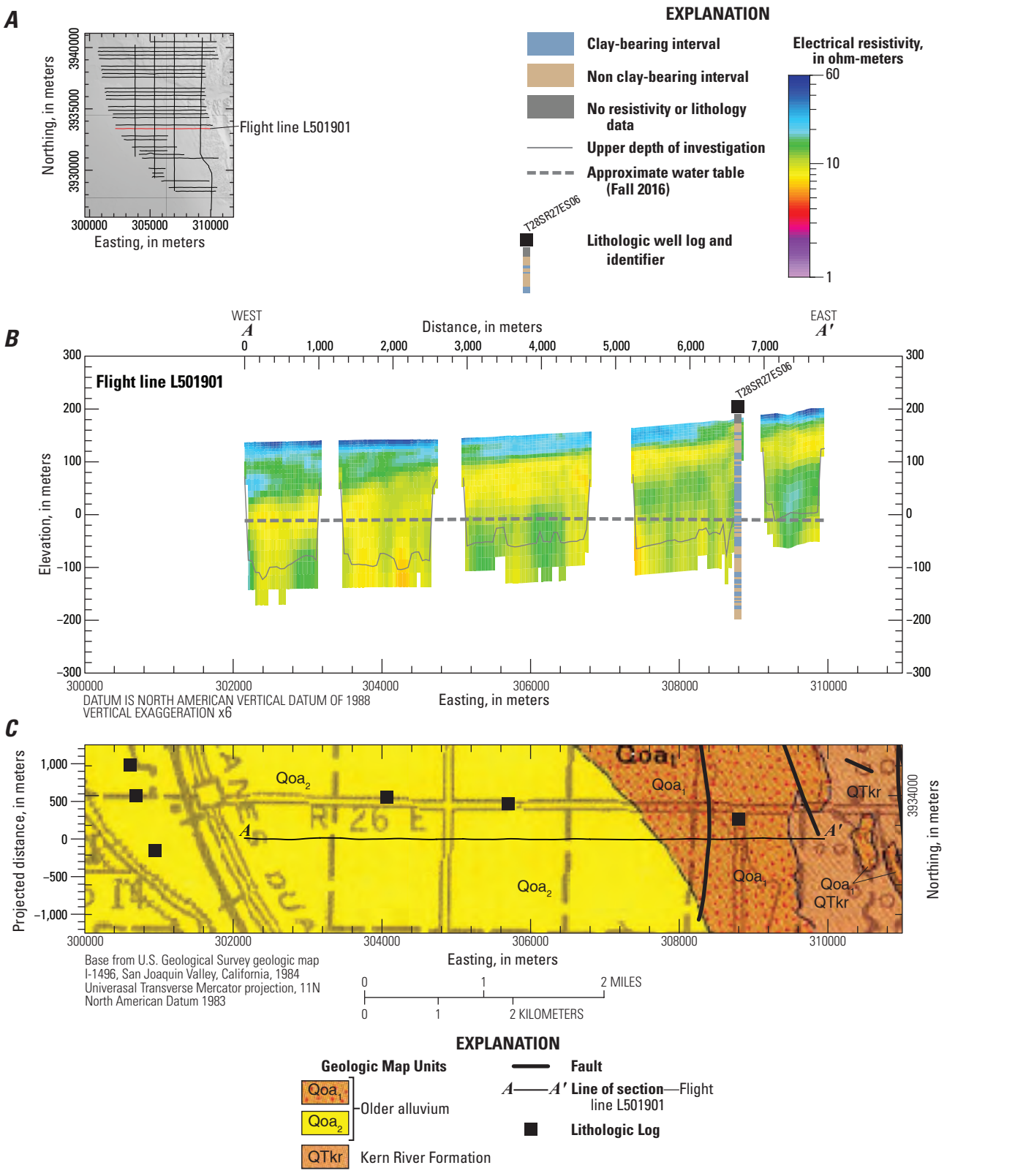

Figure 1.19. *A–C,* modeled resistivity profiles for airborne electromagnetic flight line L5001901.

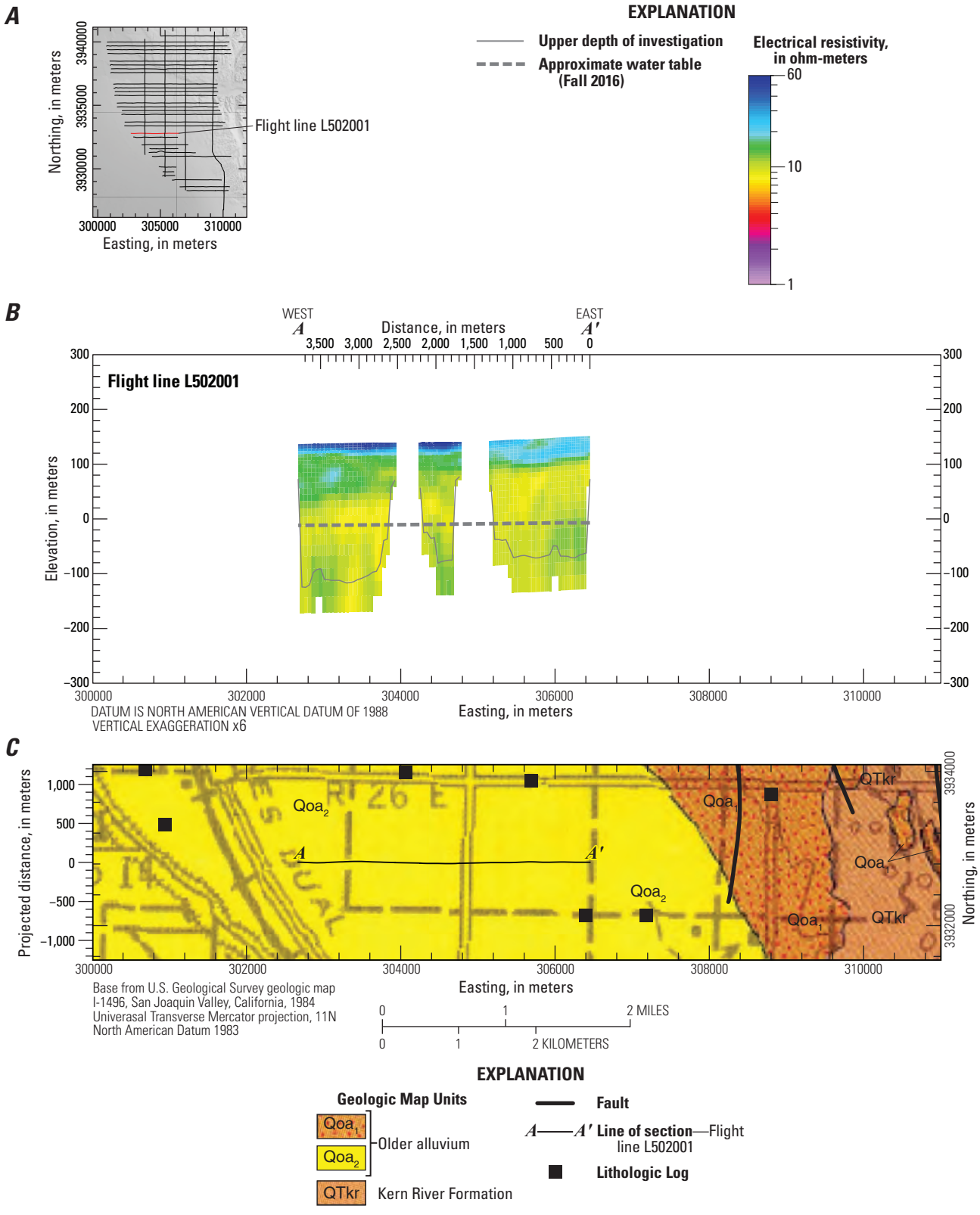

Figure 1.20. *A–C,* modeled resistivity profiles for airborne electromagnetic flight line L5002001.

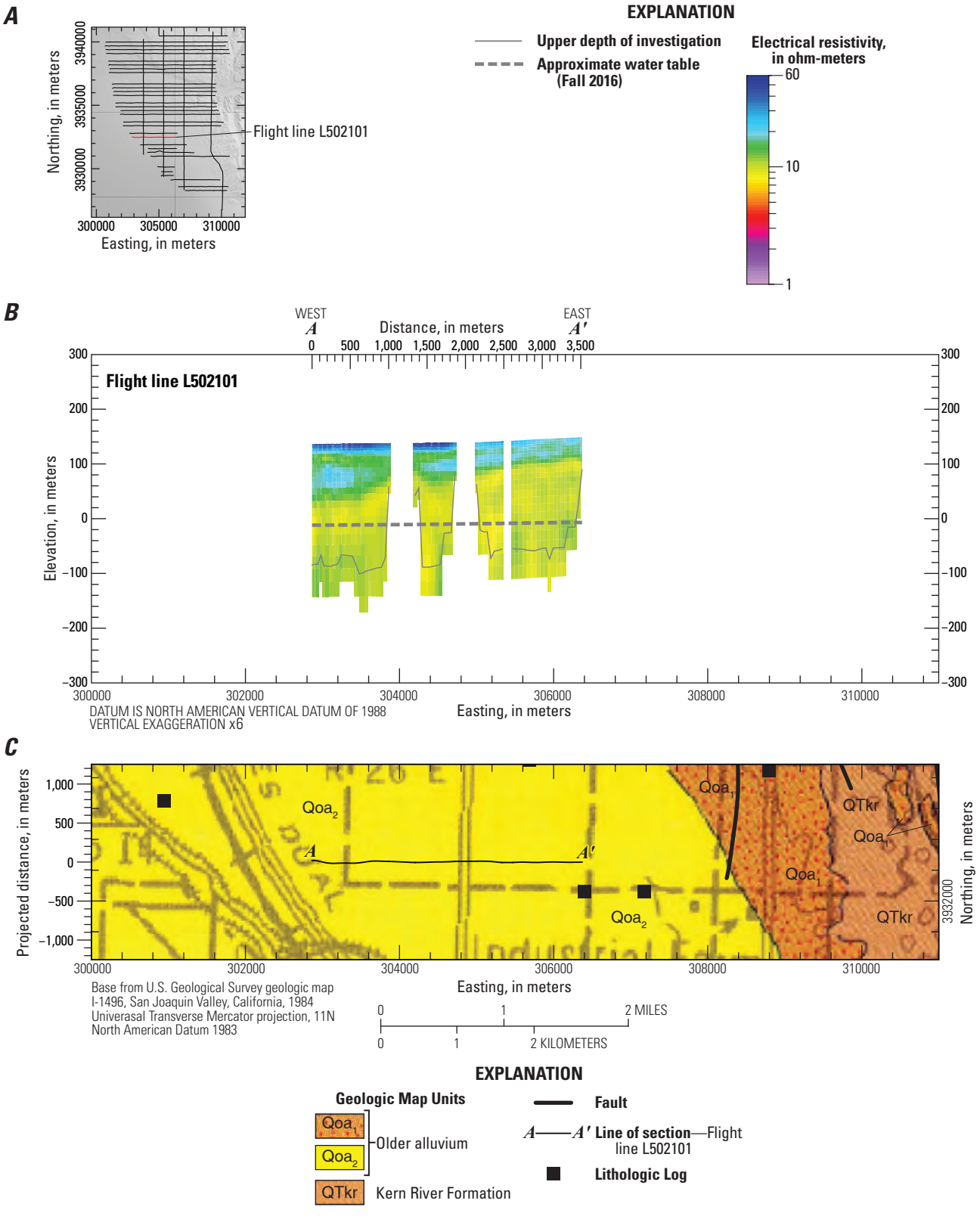

Figure 1.21. *A–C,* modeled resistivity profiles for airborne electromagnetic flight line L5002101.

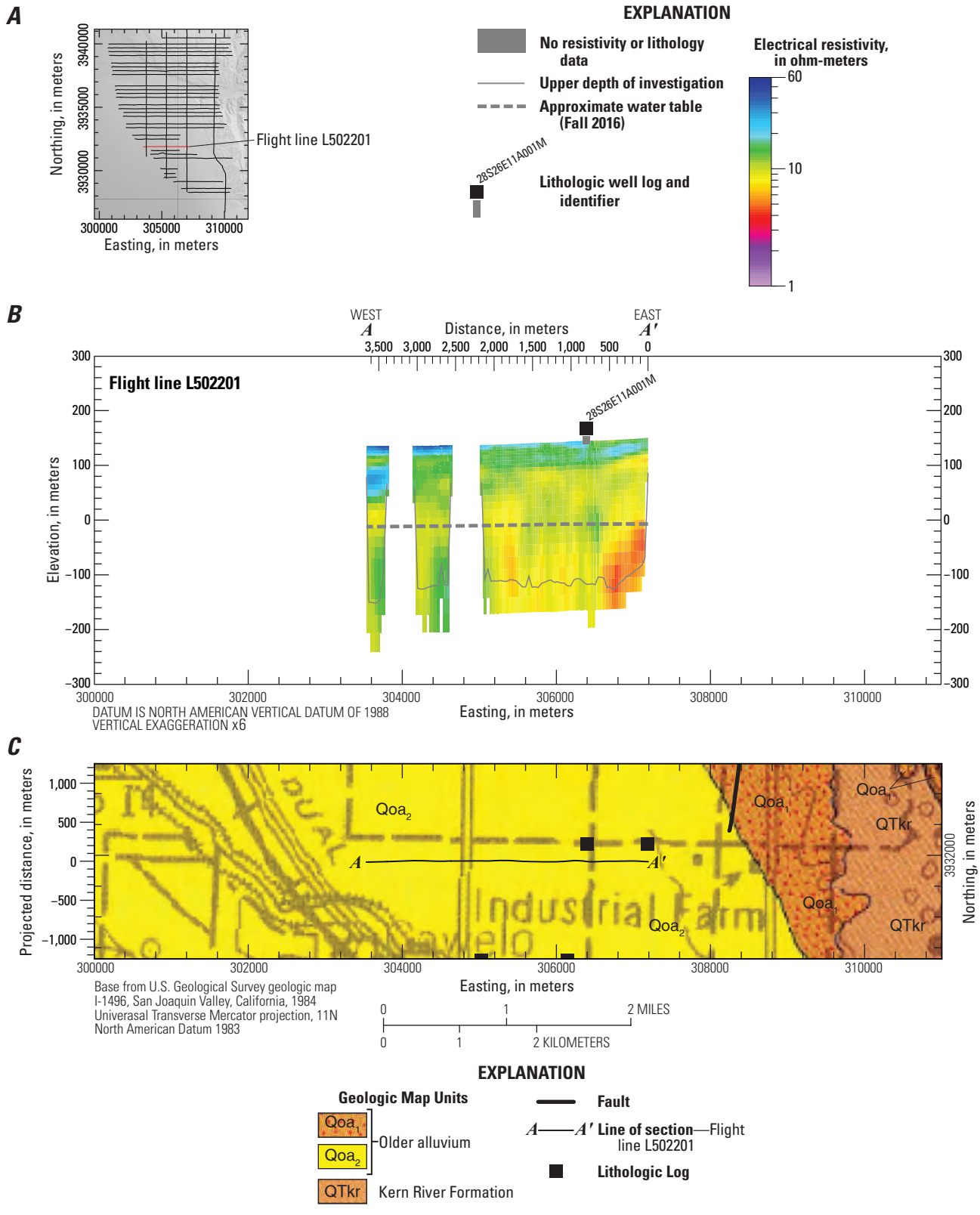

Figure 1.22. *A–C,* modeled resistivity profiles for airborne electromagnetic flight line L5002201.

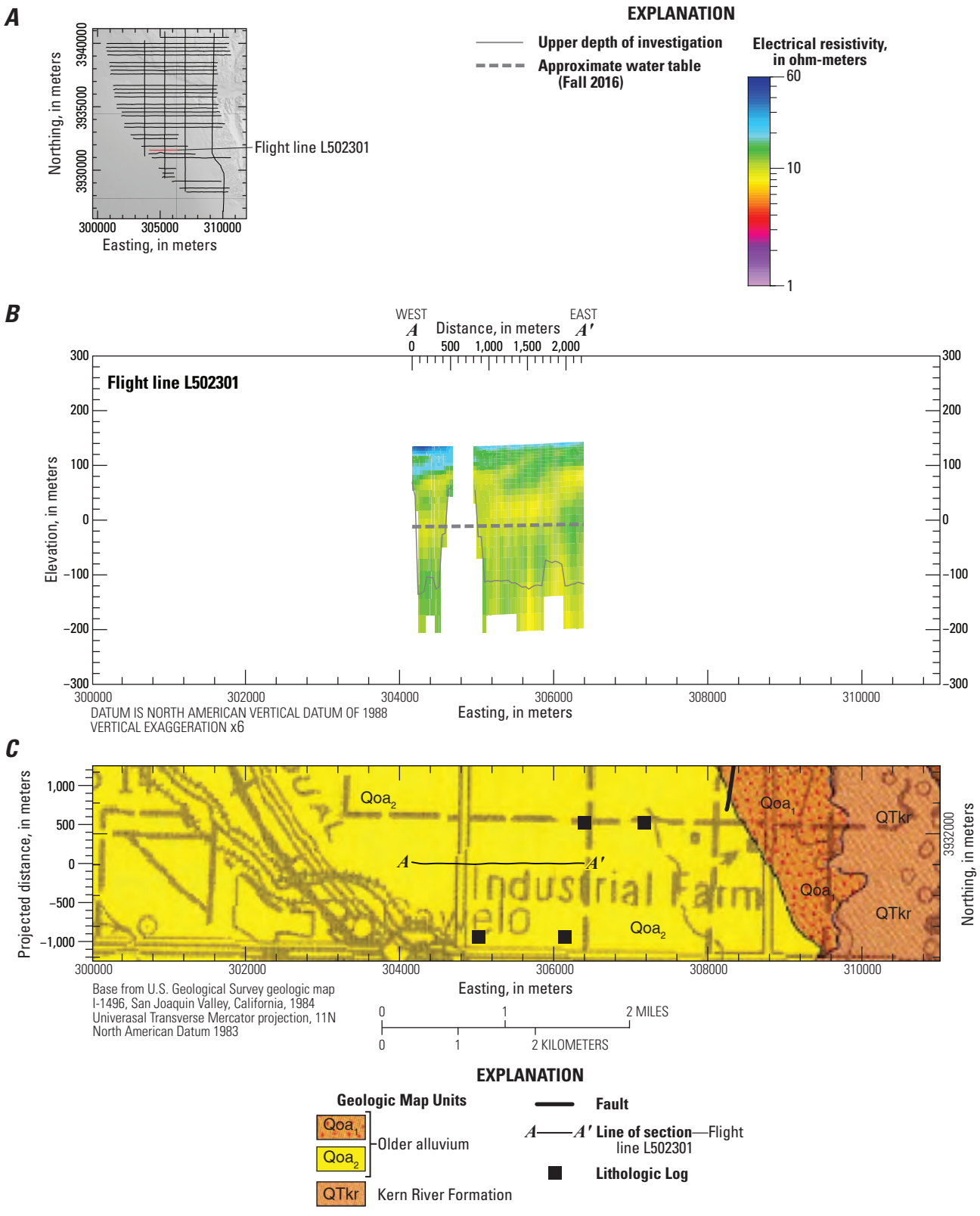

Figure 1.23. *A–C,* modeled resistivity profiles for airborne electromagnetic flight line L5002301.

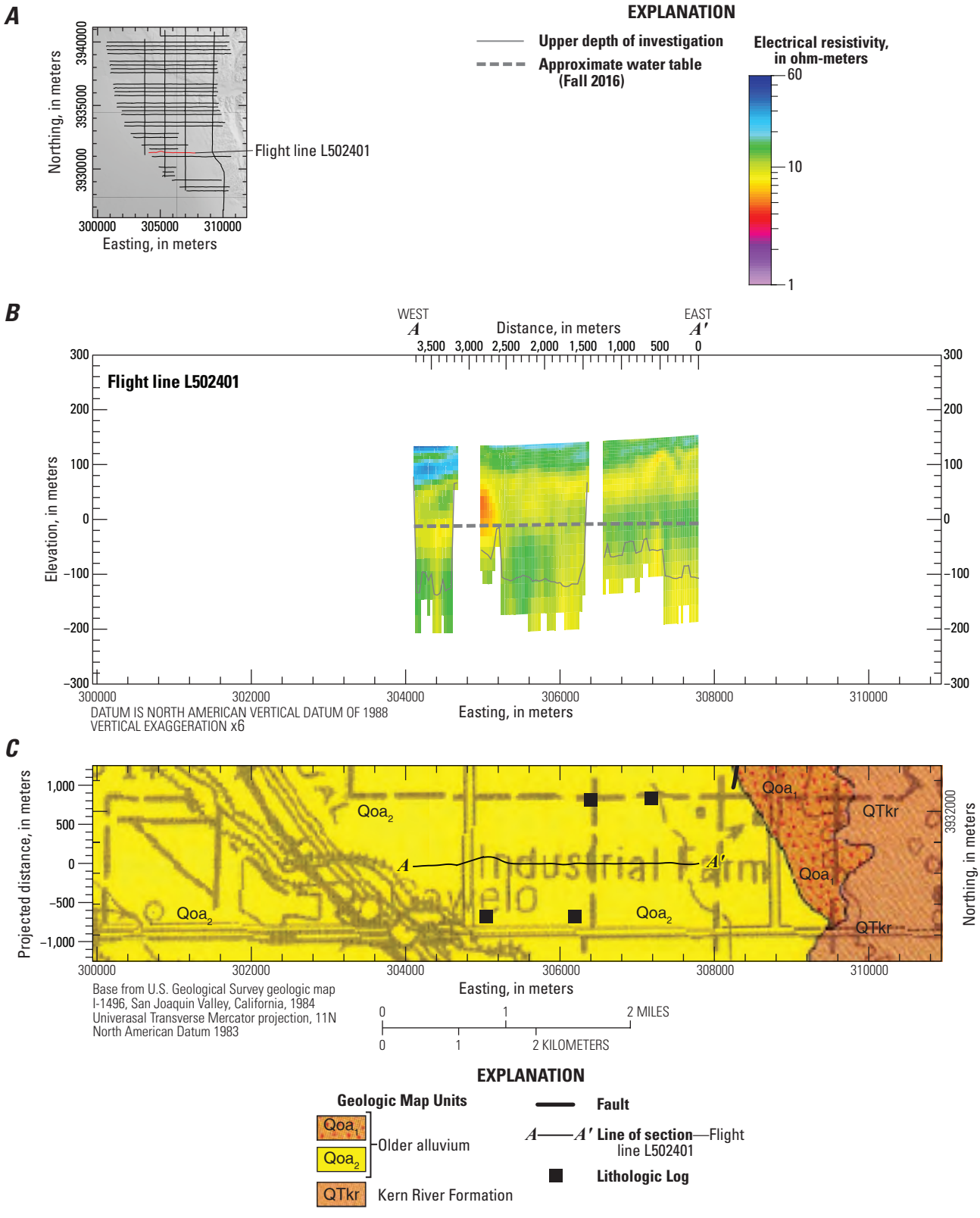

Figure 1.24. *A–C,* modeled resistivity profiles for airborne electromagnetic flight line L5002401.

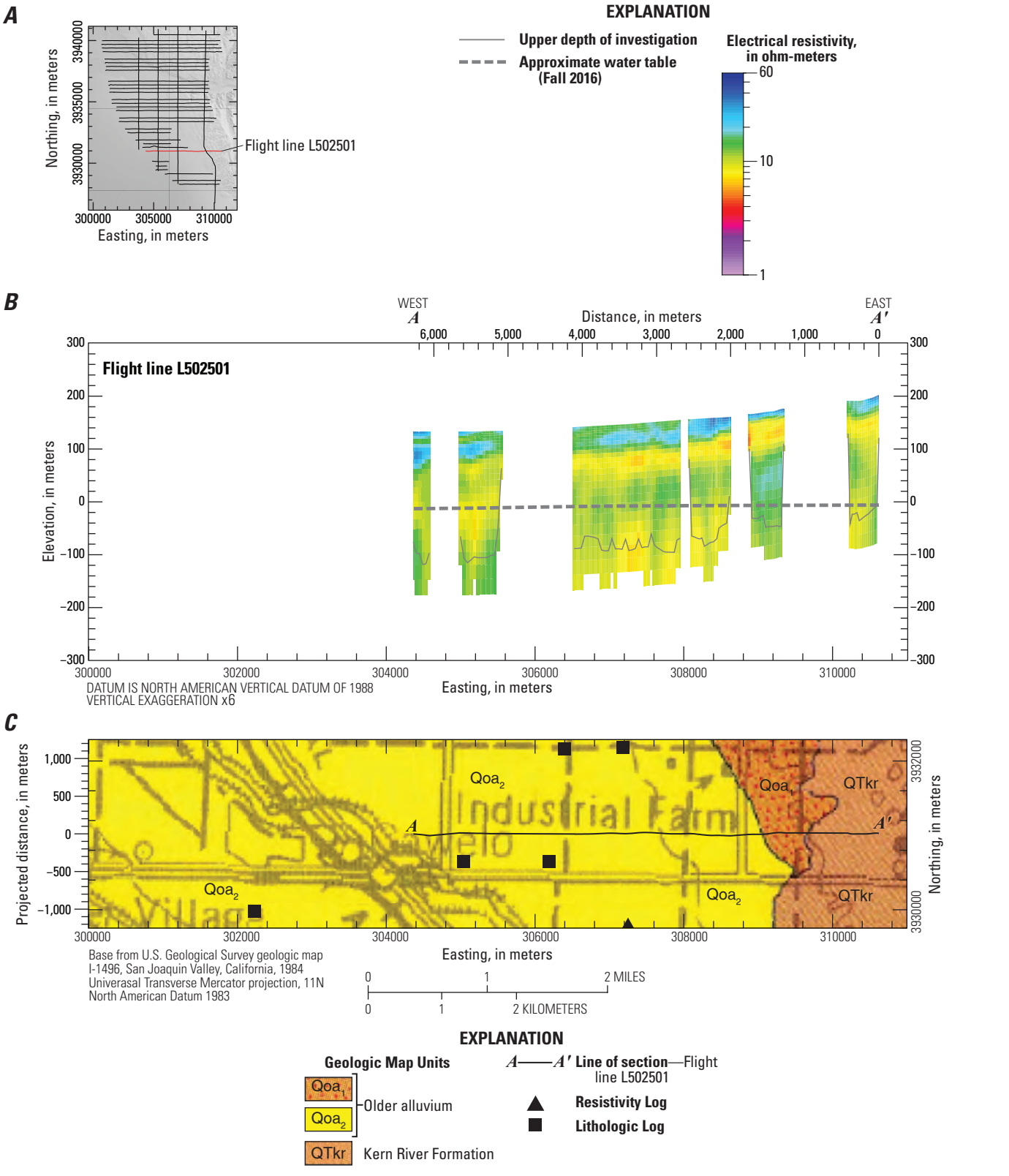

Figure 1.25. *A–C,* modeled resistivity profiles for airborne electromagnetic flight line L5002501.

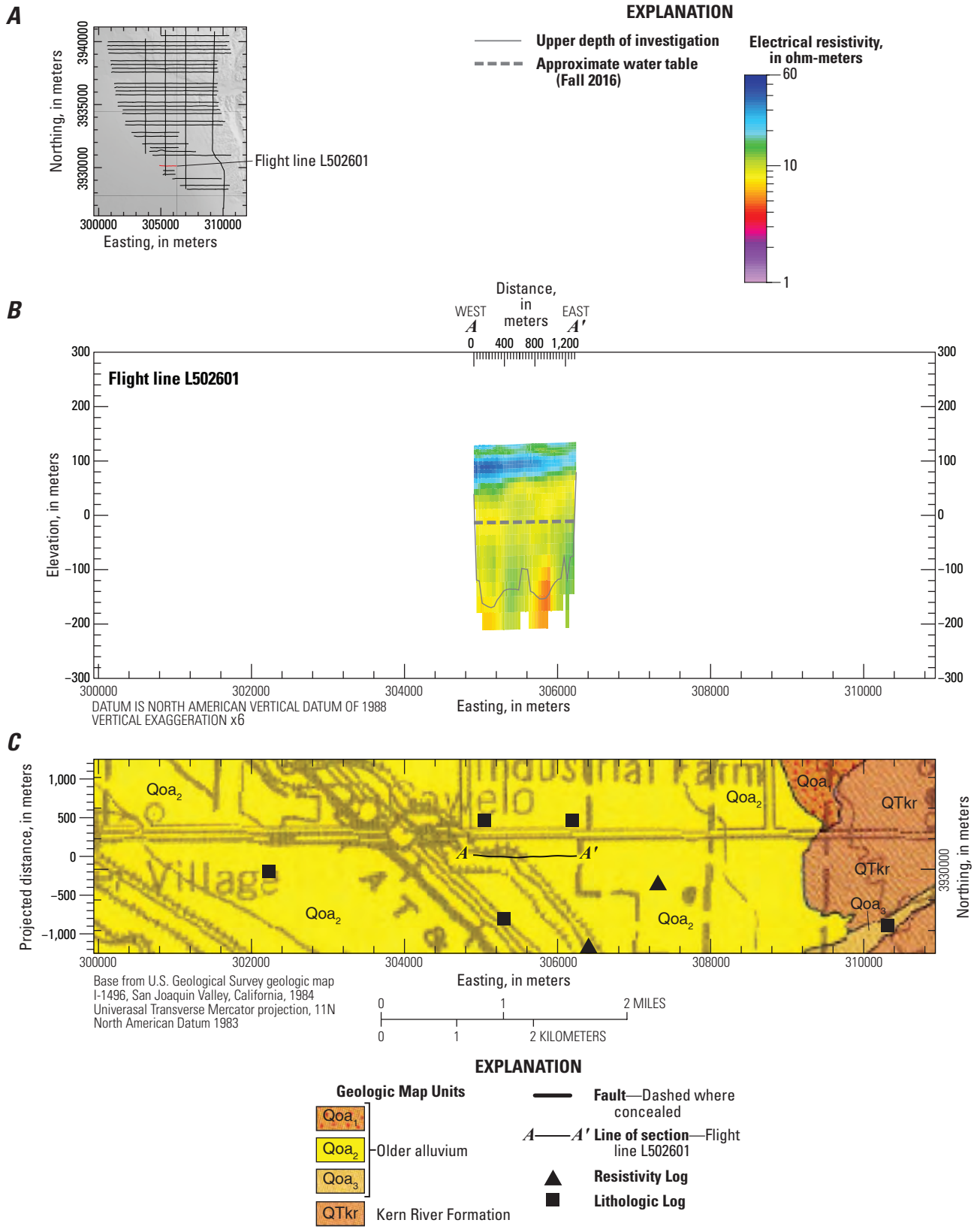

Figure 1.26. *A–C,* modeled resistivity profiles for airborne electromagnetic flight line L5002601.

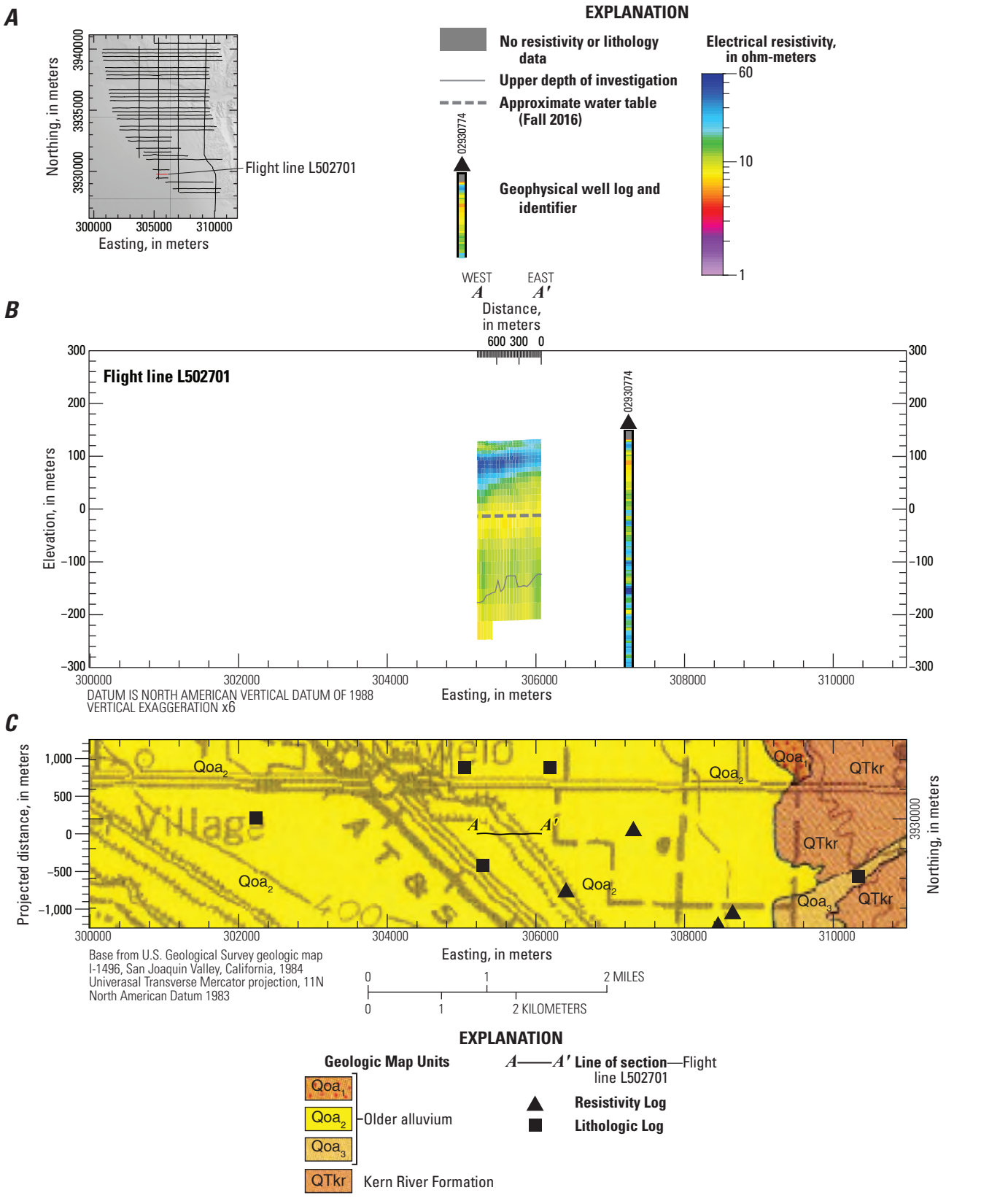

Figure 1.27. *A–C,* modeled resistivity profiles for airborne electromagnetic flight line L5002701.

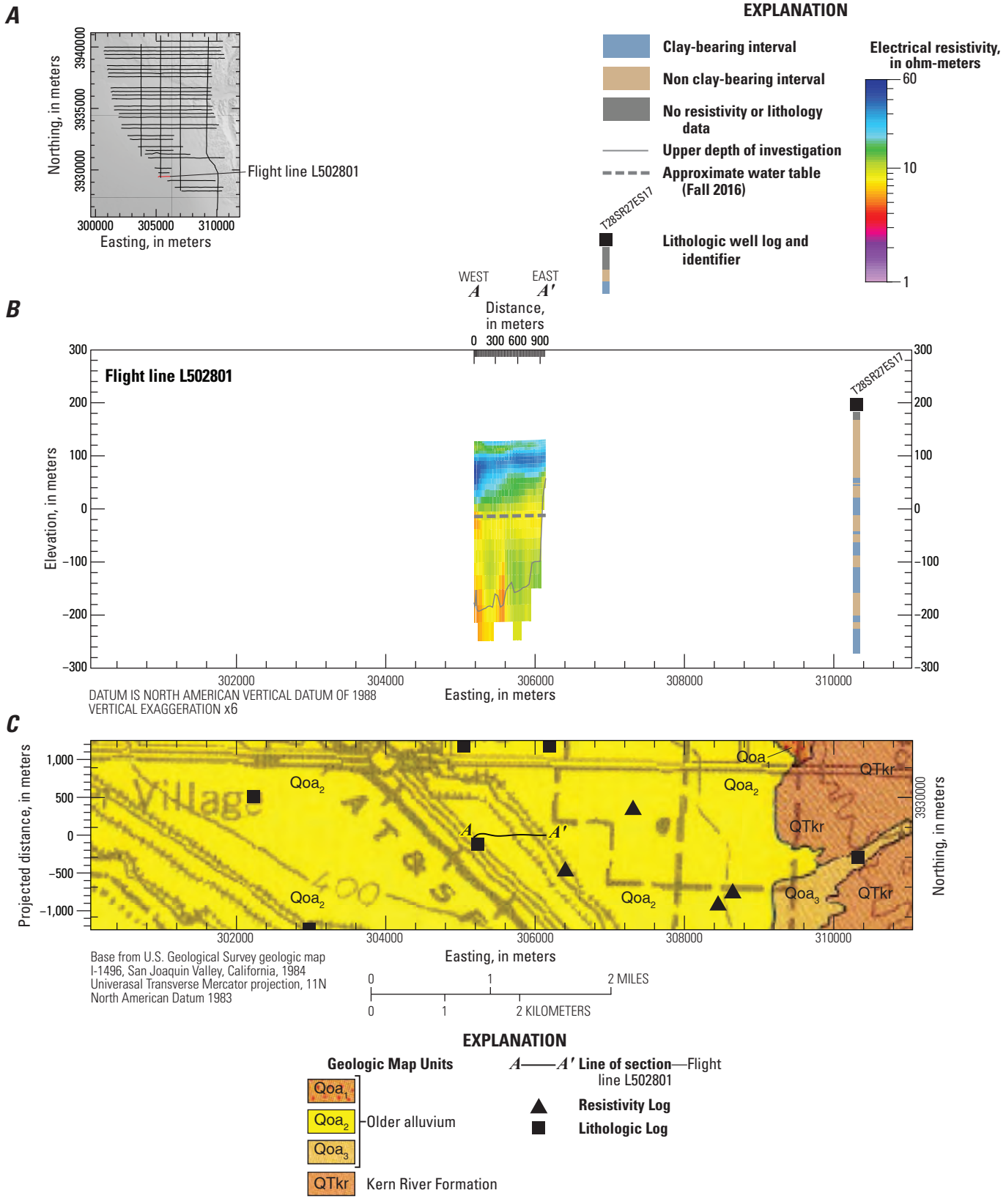

Figure 1.28. *A–C,* modeled resistivity profiles for airborne electromagnetic flight line L5002801.

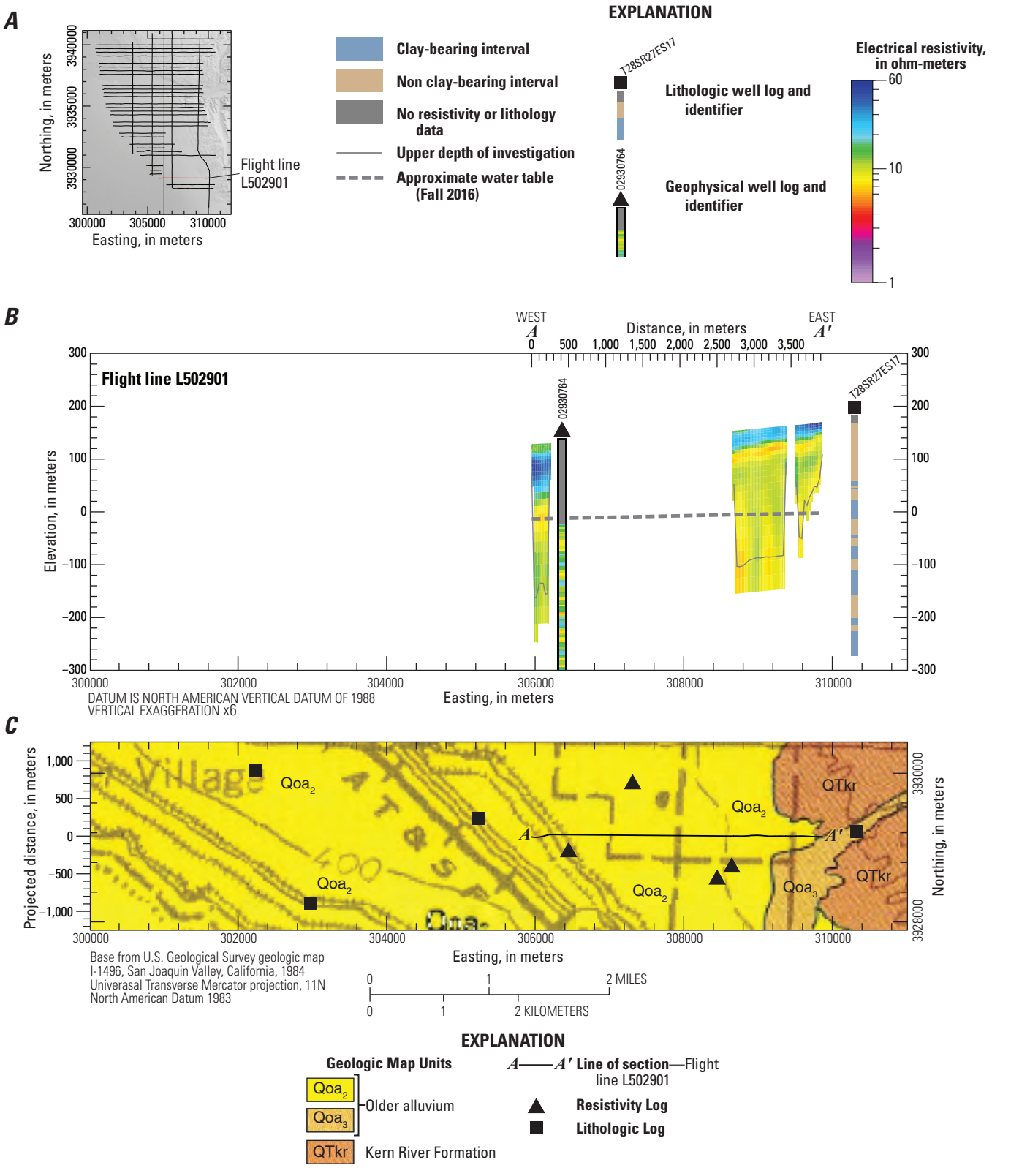

Figure 1.29. *A–C,* modeled resistivity profiles for airborne electromagnetic flight line L5002901.

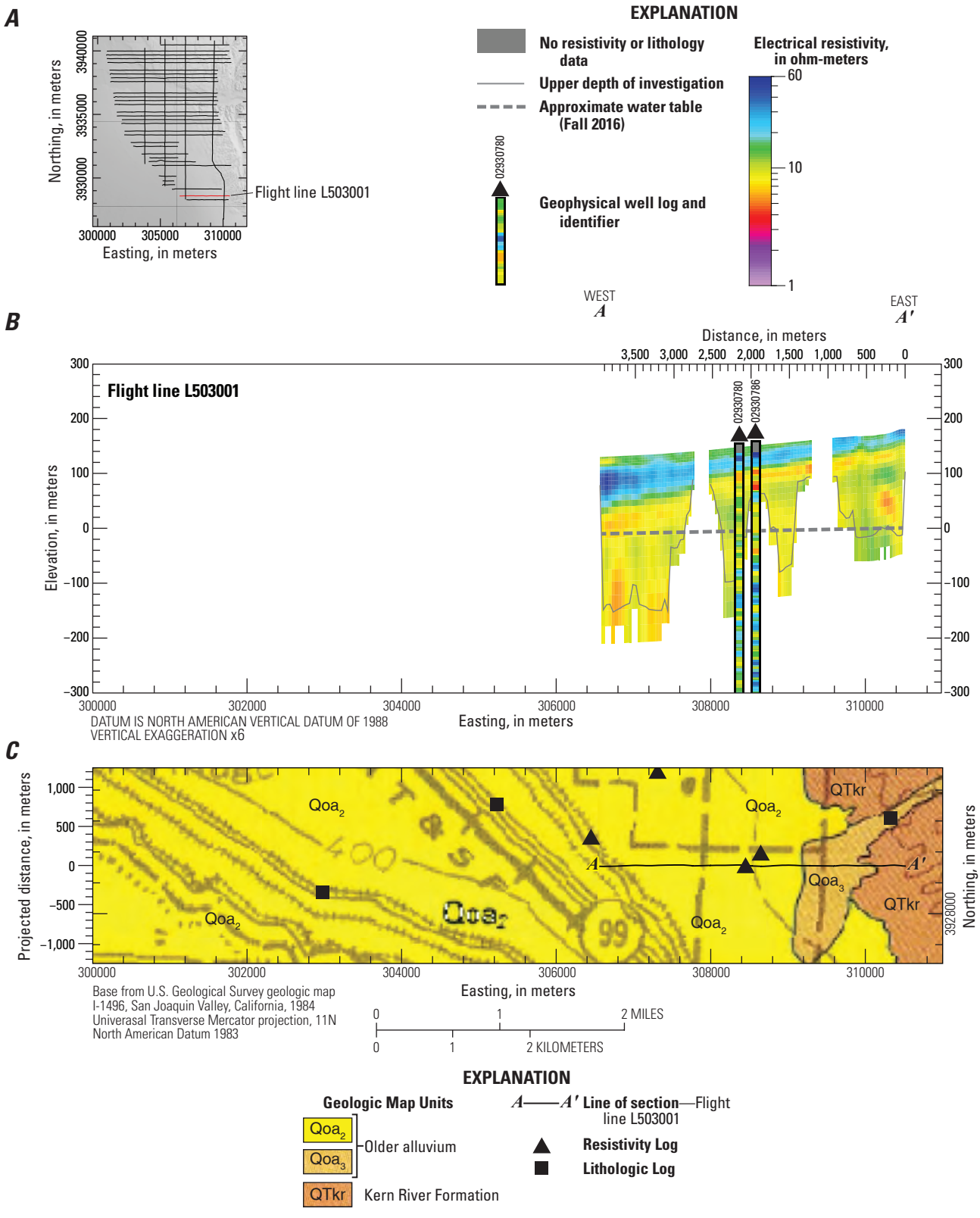

Figure 1.30. *A–C,* modeled resistivity profiles for airborne electromagnetic flight line L503001.

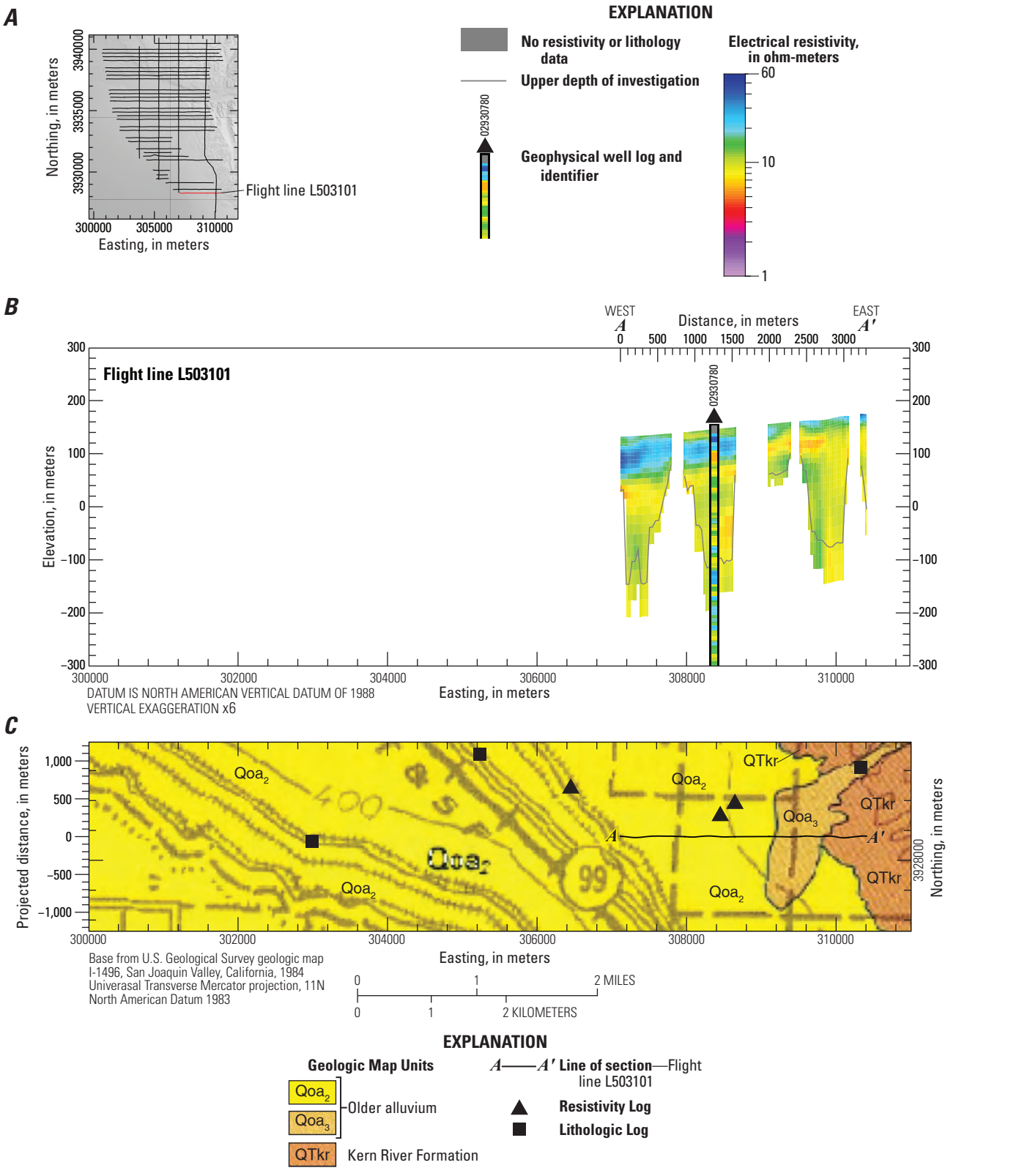

Figure 1.31. *A–C,* modeled resistivity profiles for airborne electromagnetic flight line L503101.

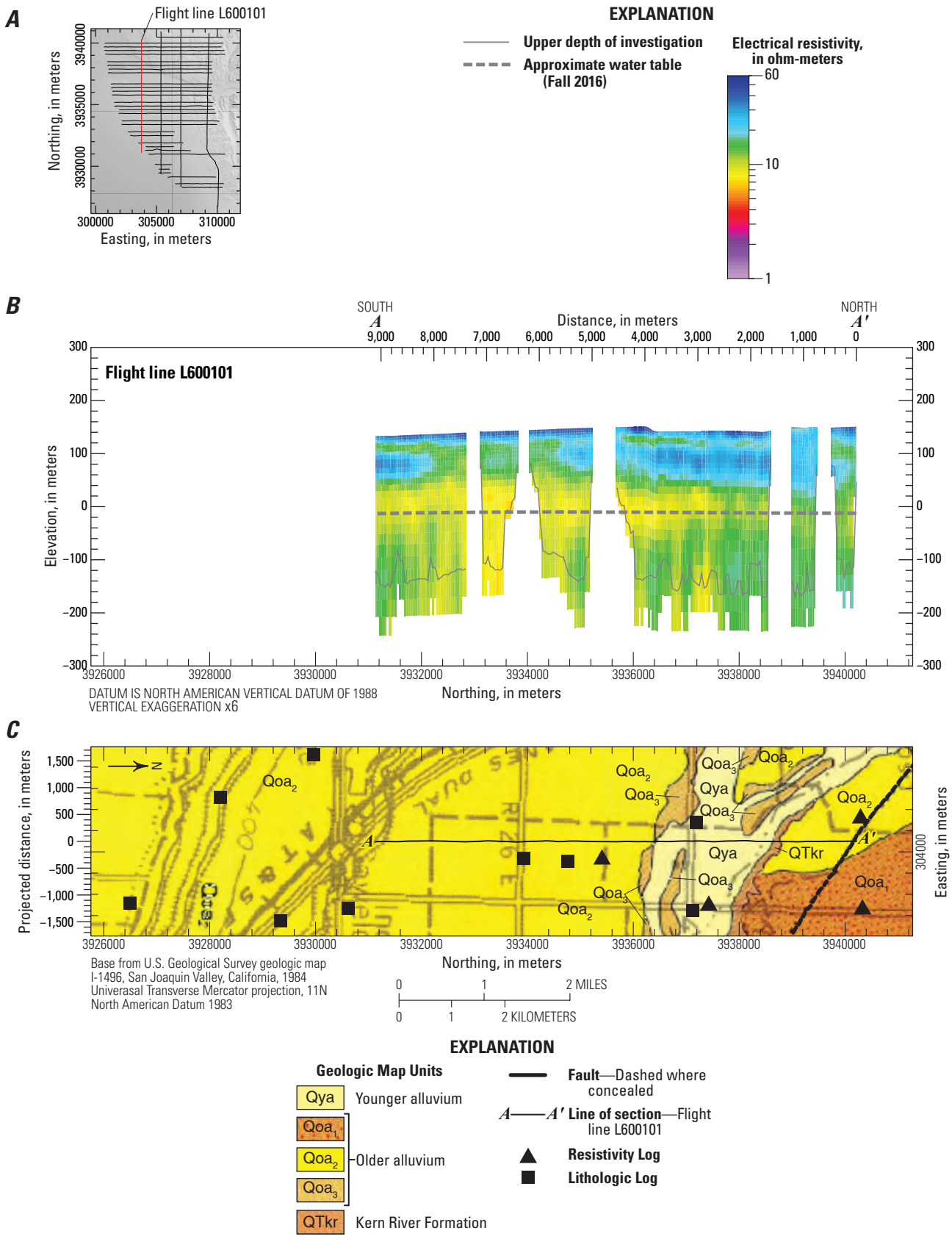

Figure 1.32. *A–C,* modeled resistivity profiles for airborne electromagnetic flight line L600101.

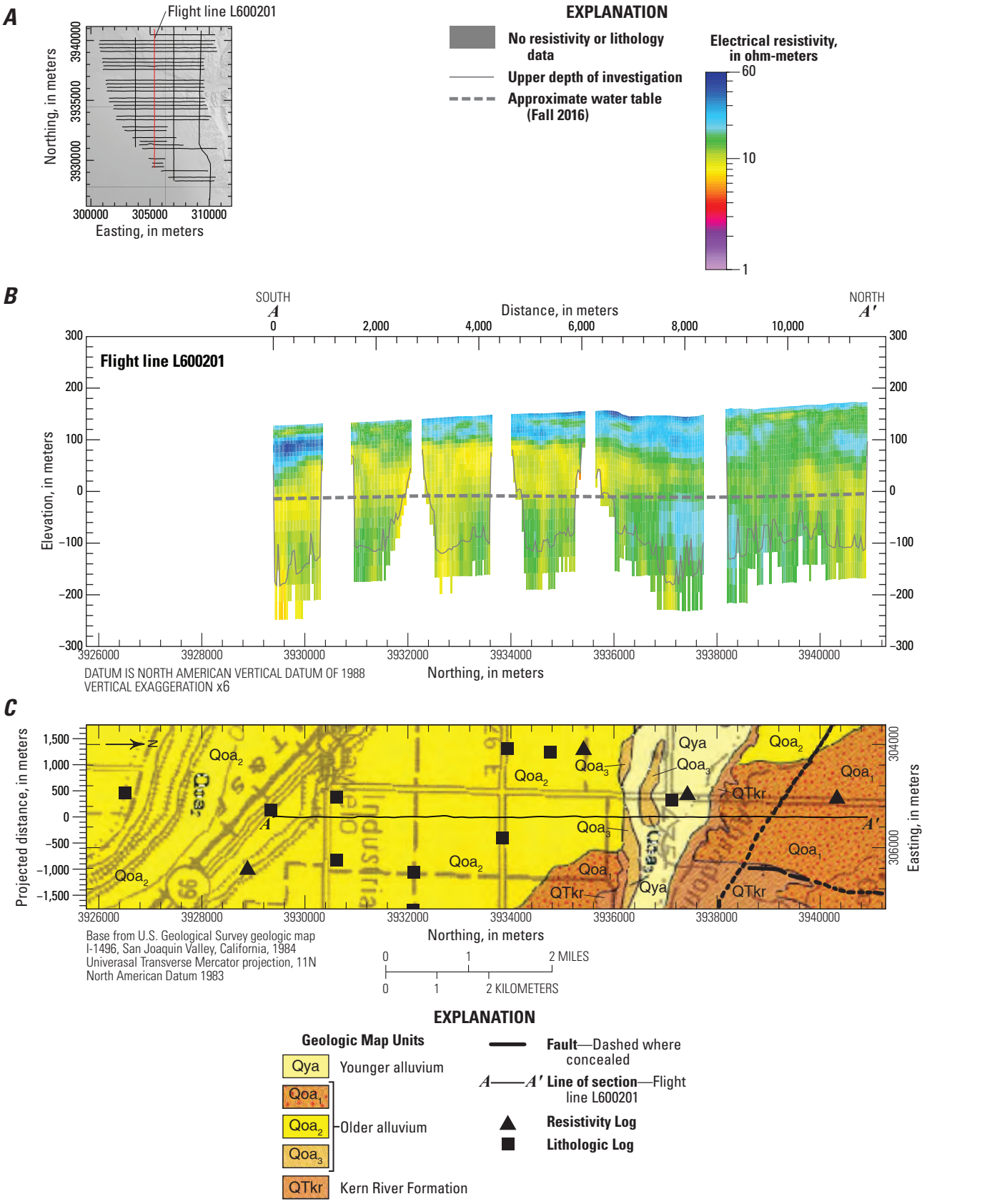

Figure 1.33. *A–C,* modeled resistivity profiles for airborne electromagnetic flight line L600201.

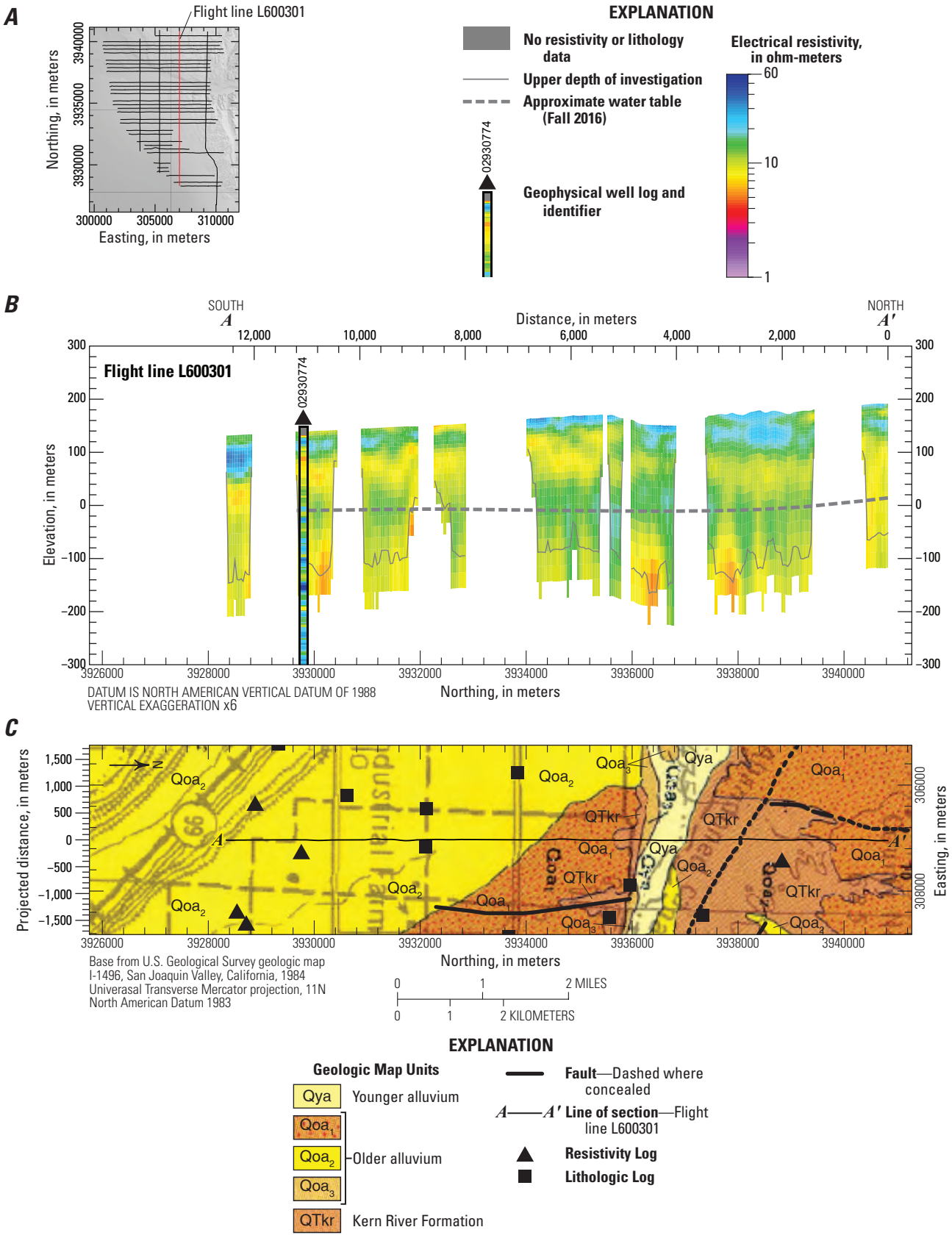

Figure 1.34. *A–C,* modeled resistivity profiles for airborne electromagnetic flight line L600301.

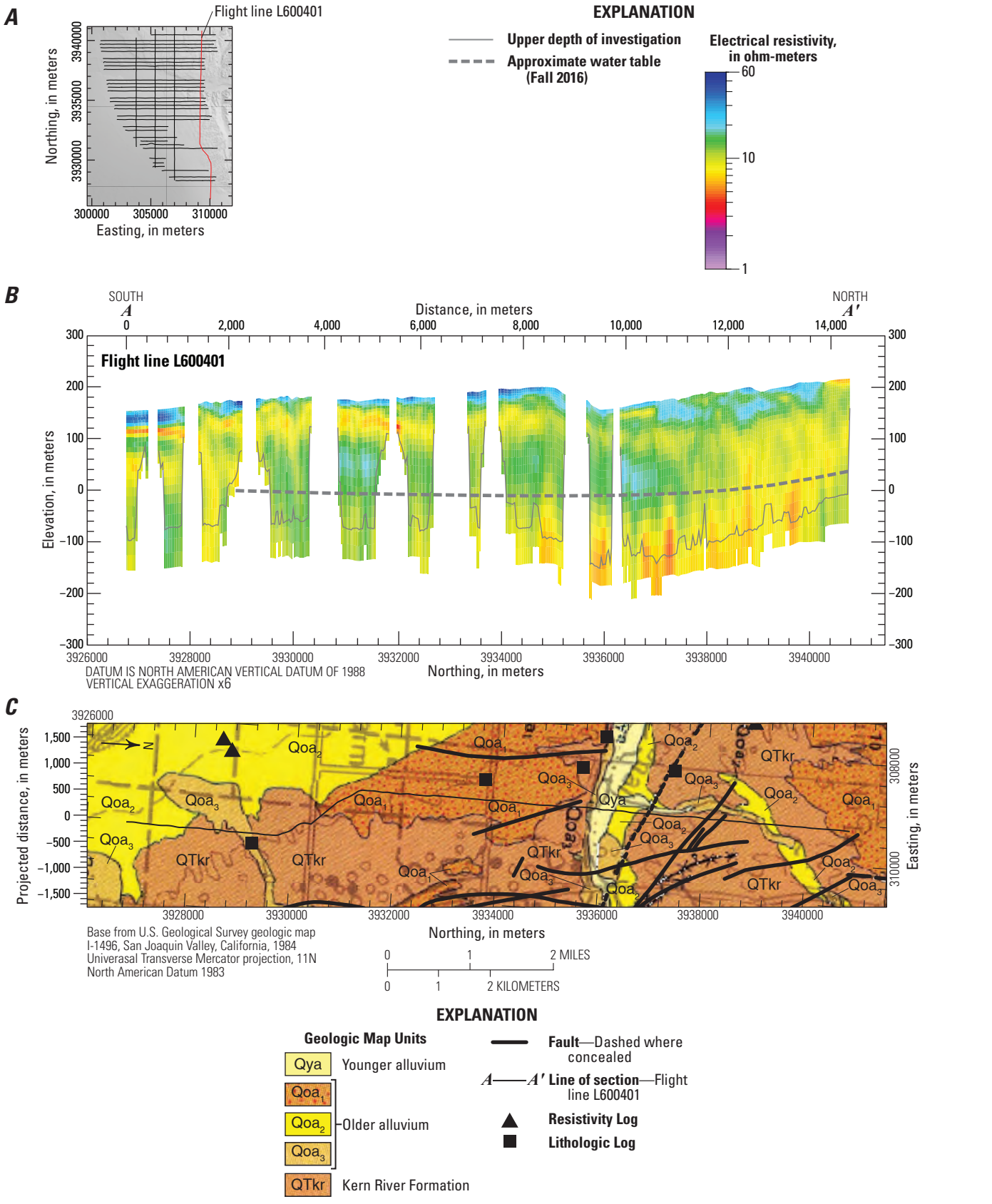

Figure 1.35. *A–C,* modeled resistivity profiles for airborne electromagnetic flight line L600401.

Publishing support provided by the Science Publishing Network,
Denver Publishing Service Center

For more information concerning the research in this report, contact the
Center Director, USGS Geology, Geophysics, and Geochemistry Science Center
Box 25046, Mail Stop 973
Denver, CO 80225
(303) 236-1800
Or visit Geology, Geophysics, and Geochemistry Science Center website at
https://www.usgs.gov/centers/gggsc

ISSN 2771-9448 (online)
https://doi.org/10.3133/dr1155